Master's Thesis

Non-Linear reduced MHD Simulations of Edge-Localized Modes in Realistic ASDEX Upgrade Geometry

Isabel Krebs

September 28, 2012

Submitted to:

Fakultät für Physik
Ludwig-Maximilians-Universität München

Supervisor:

Prof. Dr. Hartmut Zohm
Max-Planck-Institut für Plasmaphysik, Garching

Contents

Chapter 1.

Introduction

In 1920, Sir Arthur Stanley Eddington proposed for the first time, that energy in stars could be supplied by nuclear fusion ([Eddington1920]). A few years later, R. d'E. Atkinson and F. G. Houtermans specified how this could work based on the quantum mechanical tunnel effect found shortly before by G. A. Gamow ([Gamow1928], [Atkinson1929]). In the context of this progress in astrophysics, the idea came up to gain energy on earth following this example. Since the 1950s, much research has been performed in order to find out how controlled nuclear fusion could be used as an energy source. Nowadays, this idea has gained importance, considering on the one hand the ambition to reduce carbon dioxide emissions and on the other hand the difficulties associated with existing carbon-neutral energy sources like for instance nuclear fission power plants.

What makes energy extraction by nuclear fusion possible is, that the fusion of two light[1] atomic nuclei yields a new nucleus whose mass is smaller than the sum of the masses of the initial nuclei. As Albert Einstein has stated, mass and energy are equivalent. The difference between the initial and the final total mass is released as energy. To enable two colliding nuclei to fuse, their relative energy has to be sufficiently large to overcome their mutual Coulomb repulsion, which is facilitated by the possibility of tunneling.

A nuclear fusion reaction, which is particularly suitable as energy source on earth, is the fusion of the hydrogen isotopes deuterium and tritium, as the probability of this reaction at relatively small relative energies is particularly large and the energy gain is high. The released energy of 17.6 MeV is distributed in the form of kinetic energy to the reaction products, namely a helium core and a neutron.

To be able to harness nuclear fusion as energy source, the conditions to allow enough fusion reactions have to be provided using an economically reasonable amount of input power, and the produced power needs to be controllable. The necessary condition is, that a sufficiently large number of particles with enough energy is confined over a sufficiently long period of time to obtain the desired amount of fusion reactions.

Different concepts have been developed with the objective of meeting these requirements. One of the most promising concepts is thermonuclear fusion using magnetic confinement. The idea of thermonuclear fusion is to provide the necessary energy for fusion reactions in the form of thermal energy. The required temperature to allow particles in the high-energy tail of the Maxwell distribution to have a sufficient energy to fuse, is about 100 million °C. At such temperatures, the

[1] For atoms whose mass number exceeds about 60, the binding energy per nucleon decreases with increasing mass number, such that the fusion of two heavy nuclei would not be an energetically favorable process. In contrast, energy can be gained by fission of such a nucleus into two lighter nuclei of comparable masses.

atoms are ionized by collisions and thus constitute a plasma. The high temperatures preclude a confinement by material walls, but the non-zero charge of the plasma particles allows to confine them by means of a magnetic field which forces them to a gyro-motion around the magnetic field lines and reduces the transport perpendicular to the field lines.
For the success of a nuclear fusion device with magnetic confinement, it is crucial to find a magnetic field configuration ensuring a sufficiently stable equilibrium state with good confinement of particles and energy. An important theoretical tool used for this purpose is the framework of magnetohydrodynamics (MHD), describing a plasma as an electrically conducting fluid. The main challenge is to restrain plasma instabilities, which lead to losses of particles and energy or even to a complete destruction of the confinement.
A promising configuration, developed in the 1950s in the Soviet Union, is the tokamak[2], an axisymmetric toroidal system with a strong magnetic field component in toroidal direction produced by external coils and a weaker poloidal component mainly produced by a toroidal plasma current. In the last five decades the concept of the tokamak has been pursued by scientists in many different countries, yielding a spectrum of different machines. In the course of the 1970s, it turned out, that to increase energy confinement times, devices of increased size were needed. Thereupon, large machines have been built like for instance the German ASDEX in 1980, the US-American TFTR in 1982 and DIII-D in 1986, and the Japanese JT-60 in 1985. The largest one was JET, built in the United Kingdom in 1983, having a minor radius of about 1 m and a major radius of 3 m. An even larger device and the next step towards a nuclear fusion reactor will be ITER, which is currently being built in France by an international cooperation. ITER is supposed to demonstrate that significantly more power can be generated from fusion processes than is required for operation.
An important step forward in the quest for better energy and particle confinement was the discovery of the H-regime, also called H-mode, in 1982 at ASDEX. This regime, which under certain conditions appears abruptly at high auxiliary heating power, provides a significantly improved confinement due to a reduced particle and energy transport at the edge of the plasma. Subsequently, it has become a standard operational regime for ASDEX and its successor ASDEX Upgrade built in 1991, as well as for other tokamaks. In 1991, an H-mode deuterium-tritium[3] plasma discharge in JET succeeded to produce about 60 % of the input power by nuclear fusion. The discovery of the H-regime was accompanied by the occurrence of a new type of instability, the so-called edge-localized mode (ELM), which turned out to be either a curse or a blessing depending on its specific properties. Edge-localized modes are relaxation-oscillations at the plasma edge, ejecting particles and energy from the plasma. They are driven by the high density and temperature gradients at the edge of H-mode plasmas. Their favorable effect is to reduce the amount of impurities[4] contained in the plasma, which reduces the energy losses due to radiation. Additionally, they help to avoid an excess of density, which would lead to an abandonment of the H-regime. But if edge-localized modes become too violent, the reduction of the energy and

[2]The name "tokamak" is a Russian composite word for "toroidal chamber with magnetic coils".

[3]Note, that the standard tokamak experiments are done with hydrogen or helium, and only a few experimental campaigns have used deuterium-tritium plasmas.

[4]Impurities are atoms with high mass numbers coming from the plasma vessel and other plasma facing components, which enter the plasma, are ionized and then confined by the magnetic field.

particle content of the plasma degrades the performance of the device and the high heat fluxes can damage the vessel wall and components inside the vessel.
Hence, the size of edge-localized modes, the associated energy and particle losses and heat flux onto plasma facing components decide if the H-regime can be a suitable operational regime for ITER, and future nuclear fusion reactors. The prediction of the onset of edge-localized modes and their exact properties is thus crucial. As a self-consistent theoretical description of this instability has not yet been found, numerical simulations are an important tool to advance the comprehension of edge-localized modes, to analyze possibilities to control them and to extrapolate their properties to larger machine sizes. In the case of edge-localized modes, non-linear simulations are particularly important, as the linear analysis only yields information about stability boundaries, but as it is not only interesting how to avoid edge-localized modes, but also what their detailed properties are and how these can be controlled, the non-linear evolution has to be analyzed as well.
In the thesis at hand, non-linear simulations of edge-localized modes in realistic ASDEX Upgrade geometry are presented and analyzed. The simulations have been carried out using the finite element code JOREK ([Huysmans2007]), which solves the non-linear reduced MHD[5] equations in full tokamak geometry including the vacuum region between plasma and vessel wall.
Emphasis is put onto the time evolution of the instability, characterized by the exponential growth of the perturbation and its subsequent saturation. The perturbation has been decomposed into Fourier components with toroidal and poloidal periodicity. The different toroidal modes grow at different rates as some are more unstable than others. The non-linear interaction between these Fourier modes allows them to exchange energy, which influences their growth rates. This interplay of the different modes of different dominance yields a complex time evolution of the mode structure, which changes fundamentally when the saturation of the mode growth sets in.
Questions discussed in this thesis are for instance: How unstable are the different toroidal modes linearly? How does non-linear mode interaction work and how does it determine the evolution of the mode structure? What mechanisms cause the saturation and how do they influence the mode structure and the spatial structure of the toroidal perturbations? And how does an ideally conducting wall around the plasma influence the results? For the analysis, simulations have been carried out including single and multiple different toroidal modes in order to separate the dynamics of the non-linear mode interaction. This is possible, because in toroidal direction, JOREK is discretized using a Fourier representation.
Part I of the thesis introduces the theoretical background of the work. In Chapter 2 the derivation of the ideal MHD equations is outlined and the reduced MHD model is introduced. Chapters 3 and 4 present aspects of MHD equilibrium and stability theory, introducing the concept of tokamaks and discussing instabilities in these configurations. An introduction into the physics of the H-regime and edge-localized modes is presented in Chapter 5. Finally, the main numerical features of JOREK and how to simulate ELMs with JOREK are described in Chapter 6 .
In Part II, the results of the simulations are presented and discussed. Chapter 8 treats the linear mode growth, analyzing growth rates of single toroidal modes of different mode numbers and

[5]Reduced MHD is a simplified MHD model particularly suitable for the description of tokamak plasmas.

how they are influenced by an ideally conducting wall. The phenomenon of non-linear mode interaction is examined in Chapter 9, where a simple model of mode interaction is developed and used to reproduce to some extent and interpret the results obtained in the JOREK simulations. In Chapter 10, possible mechanisms responsible for the saturation of the mode growth are discussed. A summary of the results is presented in Chapter 11.

Much effort has been put into numerical simulations of edge-localized modes in the last years, some publications will be exemplarily referred to in the following. Linear stability analysis of edge-localized modes has i.a. been done using the linear codes GATO ([Bernard1981], [Saarelma2003]), ELITE ([Wilson2002], [Snyder2004]) and ILSA ([Konz2007], [Osmanlic2012]). Non-linear simulations have been carried out using for instance the codes NIMROD ([Glasser1999], [Pankin2007]), M3D ([Park1999], [Sugiyama2010]), BOUT++ ([Dudson2011]) and also JOREK ([Huysmans2007]). JOREK has been used to qualitatetively examine ELM filaments, ELM sizes, the evolution of radial profiles and heat fluxes onto plasma facing components in JET- and MAST[6]-like magnetic field geometry, to analyze the influence of pellet[7] injection onto ELMs in a plasma of circular shape and to study poloidal equilibrium flows in ELM simulations in References [Huysmans2009], [Pamela2010], [Pamela2010a] and [Pamela2011]. JOREK simulations of ELMs based on ASDEX Upgrade discharges have also been carried out. The spatial structure of the perturbation, filaments and heat and particle fluxes are analyzed for the first time in Reference [Hoelzl2011]. In Reference [Hoelzl2012], additional emphasis has been put on including a large number of toroidal Fourier harmonics, leading to a poloidal and toroidal localization of the perturbations agreeing with the experimental observations.
Finally, some references are given considering the topics mentioned in the introduction. An introduction into nuclear fusion and its use for energy production is for instance presented in Reference [Dux2002]. An overview about nuclear fusion, tokamaks and their history can be found in Reference [Wesson2004]. More detailed information about the early history of nuclear fusion research is presented in Reference [Teller1981]. MHD equilibria and stability are discussed for instance in Reference [Freidberg1987]. For an introduction into the physics of the H-mode and edge-localized modes refer to References [Biskamp1993] and [Wesson2004], an overview about the topic can be found in References [Zohm1996], [Suttrop2000] and [Pamela2010]. The possible damage of plasma facing components due to edge-localized modes in ITER has been analyzed in References [Loarte2003] and [Klimov2011]. The role of existing renewable energies in the challenge of covering the future demand for electricity is critically examined in Reference [Wagner2012].

[6] MAST is a British tokamak which has been built in 2000.

[7] Pellets are little cubes of frozen hydrogen or deuterium and tritium, injected into the plasma in order to supply the plasma with fuel.

Part I.

Theoretical background

Chapter 2.

MHD equations

2.1. Derivation of the MHD equations

To describe the time evolution of a plasma as a system of N particles, it is necessary to determine their trajectories in the $6N$-dimensional phase-space. As plasma particles are charged, their equations of motion are coupled because of electromagnetic interaction. Hence solving the resulting system of equations is in general not feasible.
Therefore it is necessary to simplify the problem by using appropriate approximating descriptions. The present work uses the framework of *magnetohydrodynamics* (MHD) which describes the plasma by a few moments of the distribution function, i.e., by macroscopic quantities in 3D position space.
The derivation of this framework is now outlined, starting from the exact distribution function $\hat{f}_\alpha(\vec{x},\vec{v},t)d^3xd^3v$ which describes the number of (indistinguishable) particles of species α in phase space element d^3xd^3v at time t. Phase space conservation and the assumption of particle conservation lead to a 6-dimensional continuity equation for $\hat{f}_\alpha$. Considering particle trajectories, $\dot{\vec{x}}$ can be replaced by $\vec{v}$ and $\dot{\vec{v}}$ by $\vec{F}/m$, where $\vec{F}$ is a force, in this case the Lorentz force $\vec{F}_L$. The continuity equation then reads

$$\frac{d\hat{f}_\alpha}{dt} = \frac{\partial \hat{f}_\alpha}{\partial t} + \vec{v}\cdot\vec{\nabla}\hat{f}_\alpha + \frac{q_\alpha}{m_\alpha}\left(\vec{\hat{E}} + \vec{v}\times\vec{\hat{B}}\right)\cdot\vec{\nabla}_v\hat{f}_\alpha = 0\,, \tag{2.1}$$

where q_α denotes the electric charge, m_α the mass of the particles and $\vec{\nabla}_v$ the gradient with respect to velocity. In general the force $\vec{F}$ can also include the gravitational force $\vec{F}_G = m_\alpha\vec{g}$. The present work treats plasmas in nuclear fusion devices where the gravitational force is negligible.
A more manageable, smooth distribution function f_α is obtained by ensemble averaging $\hat{f}_\alpha$. The same can be done with the electric and the magnetic fields, which yields the smooth, macroscopic fields $\vec{E}$ and $\vec{B}$ respectively. Ensemble averaging the continuity Equation (2.1) gives the *kinetic equation*

$$\frac{\partial f_\alpha}{\partial t} + \vec{v}\cdot\vec{\nabla}f_\alpha + \frac{q_\alpha}{m_\alpha}\left(\vec{E} + \vec{v}\times\vec{B}\right)\vec{\nabla}_v f_\alpha = \left(\frac{\partial f_\alpha}{\partial t}\right)_{\text{coll}}\,, \tag{2.2}$$

where the correlation between particle trajectories and electromagnetic fields, which manifests itself in particle collisions, are expressed by the collision term $(\partial_t f_\alpha)_{\text{coll}}$. This term contains the

dynamics and quantities on the microscopic scale, thus the interaction among individual particles.
In case of an ideal plasma, where the kinetic energy of the particles dominates over the interaction among the particles, those interactions only play a role within distances smaller than the so-called *Debye-length* λ_D. The Debye-length determines the scale on which the Coulomb potential of a charged test particle in a plasma is shielded by a displacement of plasma particles around the test particle.
The left-hand side of Equation (2.2) contains only macroscopic quantities. In case of an ideal plasma, they are averaged over the ensemble of particles within a sphere with radius λ_D, thus describing the physics on scales beyond the Debye-length. The macroscopic electromagnetic fields are obtained from the Maxwell equations with a charge density ρ_{el} and an electric current density $\vec{j}$, defined by

$$\rho_{\mathrm{el}}(\vec{x}) = \sum_{\alpha} q_\alpha \int f_\alpha(\vec{x},\vec{v})\,\mathrm{d}^3v\,, \tag{2.3}$$

$$\vec{j}(\vec{x}) = \sum_{\alpha} q_\alpha \int \vec{v} f_\alpha(\vec{x},\vec{v})\,\mathrm{d}^3v\,. \tag{2.4}$$

Depending on the physical processes to be resolved, there are different choices for the collision term in the kinetic equation (2.2). Neglecting it completely yields the *Vlasov equation* and by choosing a collision term which describes localized two-body collisions one obtains the *Boltzmann equation*. The *Fokker-Planck equation* results from choosing a collision term which takes into account the shielding of the Coulomb potential and can be used to describe dissipative processes in plasmas.
By taking different order moments of the ensemble averaged distribution function and the kinetic equation, it is possible to pass on to the magnetohydrodynamic 3D-description of the system in position space. While the information contained in the kinetic equation is equivalent to the information contained in an infinite set of its moments, the truncated set of equations only gives an approximate description of the system. The k^{th} order moment of the distribution function is a tensor of rank k defined as

$$\int \underbrace{\vec{v}\vec{v}\vec{v}\ldots\vec{v}}_{k\text{-times}} f_\alpha(\vec{x},\vec{v})\,\mathrm{d}^3v\,, \tag{2.5}$$

where the integration is carried out over the whole velocity space. The particle density n_α of species α is given by the zero order moment

$$n_\alpha(\vec{x}) = \int f_\alpha(\vec{x},\vec{v})\,\mathrm{d}^3v \tag{2.6}$$

and their center of mass velocities $\vec{u}_\alpha$ are obtained by taking the first order moment

$$\vec{u}_\alpha(\vec{x}) = \frac{1}{n_\alpha(\vec{x})} \int \vec{v} f_\alpha(\vec{x},\vec{v})\,\mathrm{d}^3v\,. \tag{2.7}$$

This allows to define the thermal velocity

$$\vec{w}_\alpha = \vec{v} - \vec{u}_\alpha \,. \tag{2.8}$$

The frictional force is caused by momentum exchange in collisions of two different species α and β, thus by microscopic processes. Hence it is determined by the first order moment of the collision term. As the integration of the collision term over the center of mass velocity does not contribute because of momentum conservation, the frictional force becomes

$$\vec{R}_{\alpha\beta} = m_\alpha \int \vec{w}_\alpha \left(\frac{\partial f_\alpha}{\partial t}\right)_{\text{coll}} \mathrm{d}^3 w_\alpha = -\vec{R}_{\beta\alpha} \,. \tag{2.9}$$

The second order moments of the distribution function yield the temperature T_α of the ensemble of particles of species α and the corresponding pressure tensor $\overset{\leftrightarrow}{P}_\alpha$:

$$k_B T_\alpha = \frac{m_\alpha}{3 n_\alpha} \int \vec{w}_\alpha^2 f_\alpha(\vec{v}) \, \mathrm{d}^3 v \,, \tag{2.10}$$

$$\overset{\leftrightarrow}{P}_\alpha = m_\alpha \int \vec{w}_\alpha \vec{w}_\alpha f_\alpha(\vec{v}) \, \mathrm{d}^3 v \,, \tag{2.11}$$

where $\vec{w}_\alpha \vec{w}_\alpha$ is a tensor product. The isotropic pressure p_α is given by one third of the trace of the pressure tensor.
The energy exchange caused by collisions between particles of two different species α and β leads to a heat transfer $Q_{\alpha\beta}$. For its calculation it again suffices to integrate over the thermal part of the velocity because microscopic collisions conserve the total energy. Hence, one obtains

$$Q_{\alpha\beta} = \frac{m_\alpha}{2} \int \vec{w}_\alpha^2 \left(\frac{\partial f_\alpha}{\partial t}\right)_{\text{coll}} \mathrm{d}^3 w_\alpha \,. \tag{2.12}$$

The third order moment of the distribution function determines the heat flux

$$\vec{q}_\alpha = \frac{m_\alpha}{2} \int \vec{w}_\alpha \vec{w}_\alpha^2 f_\alpha(\vec{v}) \, \mathrm{d}^3 v \,. \tag{2.13}$$

Having defined these macroscopic quantities, it is now possible to develop the MHD equations. They are obtained by taking moments of the kinetic equation. The zero order moment results in a continuity equation for the particle density

$$\frac{\partial n_\alpha}{\partial t} + \vec{\nabla} \cdot (n_\alpha \vec{u}_\alpha) = 0 \,, \tag{2.14}$$

where the particle conservation in collisions has been used. The equation states that the change of the particle density at some point in space is, in the absence of sources or sinks, given by the divergence of the particle flux density. The first order moment gives

$$\frac{\partial}{\partial t} (m_\alpha n_\alpha \vec{u_\alpha}) + \vec{\nabla} \cdot \left(m_\alpha n_\alpha \vec{u_\alpha} \vec{u_\alpha} + \overset{\leftrightarrow}{P}_\alpha \right) - q_\alpha n_\alpha \left(\vec{E} + \vec{u}_\alpha \times \vec{B} \right) = \vec{R}_{\alpha\beta} \,. \tag{2.15}$$

This equation describes momentum conservation: A local change of momentum can be caused by a momentum flow, thus by a divergence of the momentum flux density $\left(m_\alpha n_\alpha \vec{u_\alpha}\vec{u_\alpha} + \overleftrightarrow{P}_\alpha\right)$ or by local sinks or sources of momentum, given by the Lorentz force and the frictional force. Using the continuity equation (2.14), Equation (2.15) can also be written as

$$m_\alpha n_\alpha \left(\frac{\partial \vec{u_\alpha}}{\partial t} + \left(\vec{u_\alpha}\cdot\vec{\nabla}\right)\vec{u_\alpha}\right) + \vec{\nabla}\overleftrightarrow{P}_\alpha - q_\alpha n_\alpha \left(\vec{E} + \vec{u}_\alpha \times \vec{B}\right) = \vec{R}_{\alpha\beta}\,, \tag{2.16}$$

which is a force balance equation: It states that the acceleration of a fluid element (the first term in brackets, called *convective derivative*, is nothing but the total derivative $\frac{d\vec{u_\alpha}}{dt}$ in a fixed frame of reference) equals the sum of all external forces applied to this element.
As every k^{th} order equation contains a $(k+1)^{\text{st}}$ order quantity, an additional equation is necessary to close the system of equations. Considering the first two equations (the continuity and force balance equations), the equation of state can be used to determine the pressure. A more detailed discussion of the derivation of the MHD equations via moments of the kinetic equation and about the one-fluid and ideal MHD equations, which are presented in the next two sections, can be found in References [Freidberg1987], [Fitzpatrick2011], [Goedbloed2004], [Zohm2010] and [Zohm2004].

2.2. One-fluid MHD

Hydrogen plasmas can with some limitations be described by one-fluid MHD. For this purpose, one-fluid variables are defined:

$$\rho = m_i n_i + m_e n_e \approx m_i n\,, \tag{2.17}$$

$$\vec{v} = \frac{1}{\rho}\left(m_i n_i \vec{u}_i + m_e n_e \vec{u}_e\right) \approx \vec{u}_i\,, \tag{2.18}$$

$$\vec{j} = en\left(\vec{u}_i - \vec{u}_e\right)\,, \tag{2.19}$$

$$p = p_i + p_e\,, \tag{2.20}$$

where ρ denotes the mass density and indices i an e indicate ion and electron quantities, respectively. Electron inertia is neglected $(m_i \gg m_e)$ and quasi-neutrality is assumed $(n_i = n_e = n)$.
In terms of these quantities, the continuity equations for ions and electrons add up to the one-fluid continuity equation

$$\frac{\partial \rho}{\partial t} + \vec{\nabla}\cdot\left(\rho\vec{v}\right) = 0 \tag{2.21}$$

and adding the momentum conservation equation (2.15) for ions and electrons yields the one-fluid momentum conservation equation

$$\frac{\partial}{\partial t}\left(\rho\vec{v}\right) + \vec{\nabla}\left(\rho\vec{v}\vec{v}\right) = -\vec{\nabla}p + \vec{j}\times\vec{B}\,. \tag{2.22}$$

The anisotropic part of the pressure tensor has been neglected which is possible in case of a collision dominated plasma, i.e., if the particles undergo enough collisions to have a nearly Maxwellian distribution function and if the system length scale is much larger than their mean free path[1].
Using the continuity equation (2.21), Equation (2.22) can be reformulated as one-fluid force balance equation

$$\rho\left(\frac{\partial\vec{v}}{\partial t}+\left(\vec{v}\cdot\vec{\nabla}\right)\vec{v}\right)\equiv\rho\frac{d\vec{v}}{dt}=-\vec{\nabla}p+\vec{j}\times\vec{B}\,. \tag{2.23}$$

From equation (2.23) it follows that in the stationary case a pressure gradient is balanced by an electric current which is orthogonal to the magnetic field lines.
Reformulating the electron force balance equation gives the *generalized Ohm's law*

$$\vec{E}+\vec{v}\times\vec{B}=\eta\,\vec{j}+\frac{1}{en}\left(\vec{j}\times\vec{B}-\vec{\nabla}p_e\right)-\frac{m_e}{e}\frac{d\vec{u}_e}{dt}\,, \tag{2.24}$$

where again only the isotropic part of the pressure has been taken into account and η denotes the electrical resistivity which is proportional to the frictional force $\vec{R}_{ei}$. The Equations (2.21)-(2.24), the adiabatic equation

$$\frac{d}{dt}\left(\frac{p}{\rho^\gamma}\right)=0\,, \tag{2.25}$$

with the adiabatic index γ, and the Maxwell equations

$$\vec{\nabla}\cdot\vec{E}=\frac{\rho_{\mathrm{el}}}{\varepsilon_0} \qquad \text{(Poisson's equation)}, \tag{2.26}$$

$$\vec{\nabla}\times\vec{E}=-\frac{\partial\vec{B}}{\partial t} \qquad \text{(Faraday's law)}, \tag{2.27}$$

$$\vec{\nabla}\cdot\vec{B}=0\,, \tag{2.28}$$

$$\vec{\nabla}\times\vec{B}=\mu_0\vec{j}+\varepsilon_0\mu_0\frac{\partial\vec{E}}{\partial t} \qquad \text{(Ampère's law)}, \tag{2.29}$$

where ε_0 is the vacuum permittivity and μ_0 the vacuum permeability, form the complete set of one-fluid MHD equations.

[1] Note, that in tokamaks, for instance, this condition is usually not fulfilled in the direction parallel to the magnetic field lines, as the mean free path in this direction is typically in the order of kilometers.

2.3. Ideal MHD

Some further approximations lead to the simpler *Ideal MHD equations*. The first step is the so-called *low-frequency and long-wavelength approximation* which neglects the information about high frequencies and short wavelengths. To obtain the low-frequency and long-wavelength version of the Maxwell equations, ε_0 is formally set to zero, which yields the neglect of the net charge $\varepsilon_0 \vec{\nabla} \vec{E}$ and the displacement current $\varepsilon_0 \mu_0 \frac{\partial \vec{E}}{\partial t}$. In addition, the electron inertia is neglected by formally letting $m_e \to 0$ which allows to neglect the last term of the generalized Ohm's law (2.24). In doing so, it is assumed that the electrons respond instantaneously compared to the considered time scales because of their small mass.
These approximations restrict the validity of the equations to the description of phenomena with frequencies much smaller than the electron plasma frequency $\omega_{pe} = \sqrt{4\pi n_e e^2/m_e}$ and the electron cyclotron frequency $\omega_{ce} = eB/m_e$ and with wavelengths which are much longer than the Debye-length λ_D and the electron gyro radius $r_{Le} = v_{\text{therm},e}/\omega_{ce}$. The approximation also only properly describes electromagnetic waves with phase velocities much smaller than the speed of light and is not applicable to relativistic thermal velocities.
In the generalized Ohm's law of the ideal MHD equations also the *Hall term* $(\vec{j} \times \vec{B})/(en)$ and the *electron diamagnetic drift term* $(\vec{\nabla} p_e)/(en)$ are omitted. Comparing the diamagnetic drift term to the $\vec{E} \times \vec{B}$ term yields

$$\frac{\left| \frac{\vec{\nabla} p_e}{ne} \right|}{\left| \vec{v} \times \vec{B} \right|} \sim \frac{r_{Li}}{a} \sim \frac{\omega}{\omega_{ci}}, \tag{2.30}$$

where $\vec{\nabla} p_e \sim p_e/a$, $p_e = nT_e$, $v \sim v_{\text{therm},i} \sim \sqrt{T_i/m_i}$ and $T_e \sim T_i$ has been used. Here, $\omega_{ci} = eB/m_i$ is the ion cyclotron frequency, $r_{Li} = v_{\text{therm},i}/\omega_{ci}$ is the ion gyro radius and ω and a are the characteristic frequency and length scale of the system. Assuming that

$$\frac{r_{Li}}{a} \ll 1, \tag{2.31}$$

which implies that

$$\frac{\omega}{\omega_{ci}} \ll 1, \tag{2.32}$$

the diamagnetic drift term can be neglected. As can be seen from the force balance equation (2.23), this term is comparable to the Hall term, such that both can be omitted.
The last approximation used in the ideal MHD equations is to neglect resistivity, so that the first term on the right hand side of equation (2.24) also vanishes. Finally, the ideal MHD equations

read

$$\frac{\partial \rho}{\partial t} + \vec{\nabla} \cdot (\rho \vec{v}) = 0 \qquad \text{(continuity equation)}, \tag{2.33}$$

$$\rho \left(\frac{\partial \vec{v}}{\partial t} + \left(\vec{v} \cdot \vec{\nabla} \right) \vec{v} \right) = -\vec{\nabla} p + \vec{j} \times \vec{B} \qquad \text{(force balance equation)}, \tag{2.34}$$

$$\vec{E} + \vec{v} \times \vec{B} = 0 \qquad \text{(generalized Ohm's law)}, \tag{2.35}$$

$$\vec{\nabla} \times \vec{E} = -\frac{\partial \vec{B}}{\partial t} \qquad \text{(Faraday's law)}, \tag{2.36}$$

$$\vec{\nabla} \cdot \vec{B} = 0, \tag{2.37}$$

$$\vec{\nabla} \times \vec{B} = \mu_0 \vec{j} \qquad \text{(Ampère's law)}, \tag{2.38}$$

$$\frac{d}{dt} \left(\frac{p}{\rho^\gamma} \right) = 0 \qquad \text{(adiabatic equation)}. \tag{2.39}$$

One important implication of the ideal MHD model is the conservation of magnetic flux which is defined by

$$\hat{\Psi} = \int \vec{B} \cdot \mathrm{d}\vec{A}. \tag{2.40}$$

It can be shown that the change of the magnetic flux, passing through an arbitrary moving surface A surrounded by the path l, is given by

$$\frac{d\hat{\Psi}}{dt} = \int \frac{\partial B}{\partial t} \cdot \mathrm{d}\vec{A} - \oint \vec{u}_S \times \vec{B} \cdot \mathrm{d}\vec{l}, \tag{2.41}$$

where $\vec{u}_S$ is the velocity of the surface. Using Faraday's law (2.36) and Stokes' theorem yields

$$\frac{d\hat{\Psi}}{dt} = -\int \left(\vec{E} + \vec{u}_S \times \vec{B} \right) \cdot \mathrm{d}\vec{l}. \tag{2.42}$$

If the surface is assumed to move at the same velocity as the plasma, the ideal generalized Ohm's law can be used to show that

$$\frac{d\hat{\Psi}}{dt} = 0. \tag{2.43}$$

If the surface is chosen to be the cross section of a long and arbitrary thin tube of plasma along the field lines (which is often called *flux tube*) this implies that the magnetic field lines have to move with the plasma. Thus in ideal MHD the topology of the magnetic field lines is preserved.

2.4. Diffusion and source terms in the MHD equations

The ideal MHD model does neither include diffusive mechanisms like current, momentum or heat diffusion, nor heat or particle sources. For the description of certain phenomena it can be

crucial to consider diffusive processes. For example current diffusion, caused by resistivity, is required for field line reconnection processes as these would be prohibited by the flux conservation of ideal MHD.
For magnetically confined plasmas in nuclear fusion devices, heat and particle sources or sinks can be important, because the plasma has to be heated and particles are injected into the plasma, lost and regained.
The so-called *resistive MHD equations* are obtained by including resistivity into the ideal generalized Ohm's law (2.35) which yields

$$\vec{E} + \vec{v} \times \vec{B} = \eta \vec{j}. \tag{2.44}$$

If one splits the particle flow into a convective flow and a diffusive term describing the effect of correlated fluctuations in velocity and density, which is done in the JOREK code, and adds a particle source term, the continuity equation (2.33) yields

$$\frac{\partial \rho}{\partial t} + \vec{\nabla} \cdot (\rho \vec{v}) = \vec{\nabla} \left(D \vec{\nabla} \rho \right) + S_\rho \,, \tag{2.45}$$

where D denotes the diffusivity and S_ρ a particle source or sink. Note that using the convective derivative, this equation can also be written as

$$\frac{d\rho}{dt} = -\rho \vec{\nabla} \cdot \vec{v} + \vec{\nabla} \cdot \left(D \vec{\nabla} \rho \right) + S_\rho \,. \tag{2.46}$$

To consider diffusion and sources in the momentum conservation equation, equation (2.22) is extended by a momentum diffusion term

$$\frac{\partial}{\partial t} (\rho \vec{v}) + \vec{\nabla} (\rho \vec{v} \vec{v}) = -\vec{\nabla} p + \vec{j} \times \vec{B} + \mu \vec{\nabla}^2 \vec{v}, \tag{2.47}$$

where μ is the viscosity. Again, it is rewritten underlining its interpretation as force balance equation

$$\begin{aligned} \frac{\partial}{\partial t} (\rho \vec{v}) + \vec{\nabla} (\rho \vec{v} \vec{v}) &= -\vec{\nabla} p + \vec{j} \times \vec{B} + \mu \vec{\nabla}^2 \vec{v} \\ \Leftrightarrow \rho \frac{\partial \vec{v}}{\partial t} + \vec{v} \left[\frac{\partial \rho}{\partial t} + \vec{\nabla} \cdot (\rho \vec{v}) \right] + \rho \left(\vec{v} \cdot \vec{\nabla} \right) \vec{v} &= -\vec{\nabla} p + \vec{j} \times \vec{B} + \mu \vec{\nabla}^2 \vec{v} \\ \Leftrightarrow \rho \left[\frac{\partial \vec{v}}{\partial t} + \left(\vec{v} \cdot \vec{\nabla} \right) \vec{v} \right] + \vec{v} \left[\vec{\nabla} \cdot \left(D \vec{\nabla} \rho \right) + S_\rho \right] &= -\vec{\nabla} p + \vec{j} \times \vec{B} + \mu \vec{\nabla}^2 \vec{v}, \end{aligned} \tag{2.48}$$

where equation (2.45) has been used. The terms originating from particle diffusion and particle sources will be neglected in the following, which is possible if particle sources and particle diffusion are not too strong. This yields

$$\rho \left(\frac{\partial \vec{v}}{\partial t} + \left(\vec{v} \cdot \vec{\nabla} \right) \vec{v} \right) = -\vec{\nabla} p + \vec{j} \times \vec{B} + \mu \vec{\nabla}^2 \vec{v}. \tag{2.49}$$

Finally, diffusion and source terms are introduced into the energy equation. Therefore, the adiabatic equation (2.39) is transformed into an equation describing the temperature evolution

$$\begin{aligned}
&\frac{d}{dt}\left(\frac{p}{\rho^{\gamma}}\right) = 0 \\
\Leftrightarrow\ &\frac{d}{dt}\left(\frac{T}{\rho^{\gamma-1}}\right) = 0 \\
&\Leftrightarrow \rho\frac{dT}{dt} = T(\gamma-1)\frac{d\rho}{dt} \\
&\Leftrightarrow \rho\frac{dT}{dt} = T(\gamma-1)\left[-\rho\vec{\nabla}\cdot\vec{v} + \vec{\nabla}\cdot\left(D\vec{\nabla}\rho\right) + S_{\rho}\right] \\
&\Leftrightarrow \rho\frac{\partial T}{\partial t} = -\rho\left(\vec{v}\cdot\vec{\nabla}\right)T - (\gamma-1)T\rho\vec{\nabla}\cdot\vec{v} + (\gamma-1)T\vec{\nabla}\cdot\left(D\vec{\nabla}\rho\right) + (\gamma-1)TS_{\rho}\,,
\end{aligned} \tag{2.50}$$

where the continuity equation (2.46) has been used. The last two terms on the right hand side will again be neglected in the following. Adding heat diffusion and heat source terms yields

$$\rho\frac{\partial T}{\partial t} = -\rho\left(\vec{v}\cdot\vec{\nabla}\right)T - (\gamma-1)\rho T\vec{\nabla}\cdot\vec{v} + \vec{\nabla}\cdot\left(\overleftrightarrow{\kappa}\vec{\nabla}T\right) + S_T\,, \tag{2.51}$$

where $\overleftrightarrow{\kappa}$ and S_T are the thermal conductivity tensor[2] and the heat source respectively. A discussion of the diffusion and source terms in the MHD equations can for example be found in [Goedbloed2004] and [Pamela2010].

2.5. Reduced MHD

The MHD model the present work is based on is called *reduced MHD*. It is based on the diffusive MHD equations presented in the previous sections. The model is useful to describe strongly magnetized plasmas like the tokamak plasma considered in the work at hand, where thermal and kinetic plasma energies are much smaller than the magnetic field energy.
The reduced MHD model has first been introduced by Kadomtsev and Pogutse [Kadomtsev1974] and Strauss [Strauss1976]. The outline of the derivation of the particular formulation of reduced MHD presented in this section is based on Reference [Pamela2010].
As this thesis considers plasmas which are magnetically confined in nuclear fusion devices with toroidal geometry, cylindrical coordinates R, Z, ϕ as shown in Figure 2.1 are used in the following. Here, ϕ denotes the toroidal angle and the $R-Z$ plane is called the poloidal plane.

The reduced MHD equations are obtained by applying the following two approximations:

1. It is assumed that the toroidal component of the magnetic field is much stronger than the poloidal one: $\left|\vec{B_{\phi}}\right| \gg \left|\vec{B_{\mathrm{pol}}}\right|$

[2] Note, that heat diffusion is strongly anisotropic in magnetized plasmas.

2. The toroidal magnetic field strength is assumed to be constant in time: $\frac{\partial}{\partial t}\left|\vec{B}_\phi\right| = 0$

A consequence of the first assumption is, that spatial gradients in the toroidal direction become very small compared to gradients in the poloidal direction, because strong spatial variations along the magnetic field are restrained as they imply a bending of the magnetic field lines, and the magnetic field points mainly in toroidal direction.
Using the second assumption, the magnetic field $\vec{B}$ can be written as

$$\vec{B} = \vec{B_\phi} + \vec{B_{\text{pol}}} = F_0 \vec{\nabla}\phi + \vec{\nabla}\Psi \times \vec{\nabla}\phi\,, \tag{2.52}$$

where F_0 is a constant[3], $\vec{\nabla}\phi \equiv \vec{e_\phi}/R$, where $\vec{e_\phi}$ is the unit vector in toroidal direction and Ψ is the poloidal magnetic flux defined as

$$\Psi = \frac{1}{2\pi}\int \vec{B}_{\text{pol}}\,\mathrm{d}\vec{A}\,. \tag{2.53}$$

As the toroidal component of the magnetic field is independent of ϕ and the poloidal component is expressed by means of a stream function, definition (2.52) already implies $\vec{\nabla}\cdot\vec{B} = 0$.
With this definition of $\vec{B}$, it is now possible to obtain a new expression for the current density by using Ampère's law (2.38)

$$\begin{aligned}\vec{j} &= \frac{1}{\mu_0}\vec{\nabla}\times\left(F_0\vec{\nabla}\phi + \vec{\nabla}\Psi\times\vec{\nabla}\phi\right)\\ &= \frac{1}{\mu_0}\left[\left(\vec{\nabla}\phi\cdot\vec{\nabla}\right)\vec{\nabla}\Psi - \vec{\nabla}\phi\left(\vec{\nabla}\cdot\vec{\nabla}\Psi\right)\right]\\ &= \frac{1}{\mu_0}\left[\frac{1}{R^2}\vec{\nabla}_\perp\left(\frac{\partial\Psi}{\partial\phi}\right) - \vec{\nabla}\phi\left(\Delta^*\Psi\right)\right],\end{aligned} \tag{2.54}$$

where $\vec{\nabla}_\perp = \vec{\nabla} - \vec{B}\left(\vec{B}\cdot\vec{\nabla}\right)/\left|\vec{B}\right|^2$ is the gradient perpendicular to the magnetic field, which is

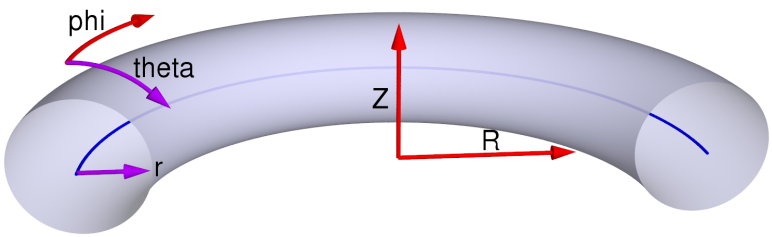

Figure 2.1.: Cylindrical coordinates R, ϕ and Z (red) and additional poloidal coordinates r and θ (violet).

[3]Note, that F_0 is also constant in space, which means, that the toroidal component of the magnetic field is described as a vacuum field, implying the neglect of poloidal currents.

approximately the poloidal direction and Δ^* denotes the *Grad-Shafranov operator* defined by

$$\Delta^* = R\frac{\partial}{\partial R}\left(\frac{1}{R}\frac{\partial}{\partial R}\right) + \frac{\partial^2}{\partial Z^2}\,. \tag{2.55}$$

From assumption 1, it follows, that gradients in toroidal direction are very small. Hence, the first term on the right hand side of equation (2.54) can be neglected. This leads to the expression

$$\vec{j} = j\vec{\nabla}\phi\,, \tag{2.56}$$

where j is defined as

$$j = -\frac{1}{\mu_0}\Delta^*\Psi\,. \tag{2.57}$$

Note, that according to this definition, j does not have the dimensions of a current density. The physical toroidal current density is given by j/R. Using Faraday's law (2.36), $\vec{\nabla}\times\vec{B} = \vec{\nabla}\times\vec{B}_{\mathrm{pol}}$ and $\vec{B}_{\mathrm{pol}} = \vec{\nabla}\times\left(\Psi\vec{\nabla}\phi\right)$ one obtains

$$\vec{\nabla}\times\left[\frac{\partial}{\partial t}\left(\Psi\vec{\nabla}\phi\right) + \vec{E}\right] = 0\,. \tag{2.58}$$

According to this equation, it is possible to define a scalar potential u such that

$$-F_0\vec{\nabla}u = \frac{\partial}{\partial t}\left(\Psi\vec{\nabla}\phi\right) + \vec{E}\,. \tag{2.59}$$

It is now sensible to split the velocity into its components parallel and perpendicular to the magnetic field

$$\vec{v} = \vec{v}_{\parallel} + \vec{v}_{\perp}\,, \tag{2.60}$$

where the parallel component is expressed by $\vec{v}_{\parallel} = v_{\parallel}\vec{B}$. To obtain an expression for the perpendicular component, the curl of the generalized Ohm's law (2.44) with $\vec{\nabla}\phi$ is taken and $\vec{E}$ and $\vec{j}$ are replaced using Equations (2.59) and (2.56). This yields

$$\begin{aligned}\vec{\nabla}\phi\times\left[-\frac{\partial}{\partial t}\left(\Psi\vec{\nabla}\phi\right) - F_0\vec{\nabla}u + \vec{v}\times\vec{B} = \eta\, j\vec{\nabla}\phi\right]\\ \Leftrightarrow \vec{v}_{\perp} - \frac{R^2}{F_0}\left(\vec{\nabla}\phi\cdot\vec{v}_{\perp}\right)\vec{B} = R^2\vec{\nabla}\phi\times\vec{\nabla}u\,.\end{aligned} \tag{2.61}$$

According to assumption 1, the projection of $\vec{v}_{\perp}$ onto the toroidal direction can be neglected. Thus, $\vec{v}_{\perp}$ can be expressed by

$$\vec{v}_{\perp} = R^2\vec{\nabla}\phi\times\vec{\nabla}u\,. \tag{2.62}$$

Now, the dot product of the generalized Ohm's law with $\vec{\nabla}\phi$ is taken to recover the information contained in the toroidal part of this equation

$$\vec{\nabla}\phi\cdot\left[-\frac{\partial}{\partial t}\left(\Psi\vec{\nabla}\phi\right)-F_0\vec{\nabla}u+\vec{v}\times\vec{B}=\eta j\vec{\nabla}\phi\right]$$
$$\Leftrightarrow\frac{\partial\Psi}{\partial t}=R\left[\Psi,u\right]+\eta j-F_0\frac{\partial u}{\partial\phi}\,, \tag{2.63}$$

where again the toroidal component of $\vec{v}_\perp$ has been neglected. The Poisson brackets are defined as $[A,B]\equiv\vec{e_\phi}\cdot\left(\vec{\nabla}A\times\vec{\nabla}B\right)$.

The next step is to reduce the force balance equation. This is done by applying $\vec{\nabla}\phi\cdot\vec{\nabla}\times\left(R^2...\right)$ to equation (2.34) yielding

$$\vec{\nabla}\phi\cdot\vec{\nabla}\times\left(R^2\left[\rho\frac{\partial\vec{v}}{\partial t}+\rho\left(\vec{v}\cdot\vec{\nabla}\right)\vec{v}=-\vec{\nabla}p+\vec{j}\times\vec{B}\right]\right)$$
$$\Leftrightarrow R\vec{\nabla}\cdot\left(R^2\rho\vec{\nabla}_\perp\left(\frac{\partial u}{\partial t}\right)\right)=\left[R^4\rho W,u\right]-\frac{1}{2}\left[R^2\rho,R^4\left|\vec{\nabla}_\perp u\right|^2\right]-\left[R^2,p\right]$$
$$+\left[\Psi,j\right]-\frac{F_0}{R}\frac{\partial j}{\partial\phi}\,, \tag{2.64}$$

where the *toroidal vorticity* W is defined by

$$\vec{w}=\vec{\nabla}\times\vec{v}_\perp\,, \tag{2.65}$$
$$W=\vec{\nabla}\phi\cdot\vec{w}=\vec{\nabla}_\perp^2 u\,. \tag{2.66}$$

Extending the equation by a momentum diffusion term yields the *vorticity equation*

$$R\vec{\nabla}\cdot\left(R^2\rho\vec{\nabla}_\perp\left(\frac{\partial u}{\partial t}\right)\right)=\left[R^4\rho W,u\right]-\frac{1}{2}\left[R^2\rho,R^4\left|\vec{\nabla}_\perp u\right|^2\right]-\left[R^2,p\right]+\left[\Psi,j\right]-\frac{F_0}{R}\frac{\partial j}{\partial\phi}+\mu_\perp R\vec{\nabla}^2W\,. \tag{2.67}$$

To obtain the *parallel velocity equation*, the dot product of equation (2.34) with $\vec{B}$ is taken which gives

$$\vec{B}\cdot\left[\rho\frac{\partial\vec{v}}{\partial t}+\rho\left(\vec{v}\cdot\vec{\nabla}\right)\vec{v}=-\vec{\nabla}p+\vec{j}\times\vec{B}\right]$$
$$\Leftrightarrow\rho F_0^2\frac{dv_\parallel}{dt}=F_0\frac{\partial p}{\partial\phi}-R\left[\Psi,p\right]\,, \tag{2.68}$$

and a momentum diffusion term is added yielding

$$\rho F_0^2\frac{dv_\parallel}{dt}=F_0\frac{\partial p}{\partial\phi}-R\left[\Psi,p\right]+\mu_\parallel\vec{\nabla}^2v_\parallel\,. \tag{2.69}$$

Also for this derivation it is important to keep in mind that vector quantities parallel to the magnetic field are assumed to have a toroidal component only, whereas perpendicular vector quantities are assumed to be purely poloidal.
Including the continuity equation (2.45) and the energy equation (2.51), the full set of reduced MHD equations reads

$$\frac{\partial \rho}{\partial t} + \vec{\nabla}(\rho \vec{v}) = \vec{\nabla} \cdot \left(D \vec{\nabla} \rho \right) + S_\rho \tag{2.70}$$

$$\begin{aligned} R \vec{\nabla} \cdot \left(R^2 \rho \vec{\nabla}_\perp \left(\frac{\partial u}{\partial t} \right) \right) = & \left[R^4 \rho W, u \right] - \frac{1}{2} \left[R^2 \rho, R^4 \left| \vec{\nabla}_\perp u \right|^2 \right] - \left[R^2, p \right] + \left[\Psi, j \right] \\ & - \frac{F_0}{R} \frac{\partial j}{\partial \phi} + \mu_\perp R \vec{\nabla}^2 W \end{aligned} \tag{2.71}$$

$$\rho F_0^2 \frac{dv_\parallel}{dt} = F_0 \frac{\partial p}{\partial \phi} - R \left[\Psi, p \right] + \mu_\parallel \vec{\nabla}^2 v_\parallel \tag{2.72}$$

$$\frac{\partial \Psi}{\partial t} = R \left[\Psi, u \right] + \eta j - F_0 \frac{\partial u}{\partial \phi} \tag{2.73}$$

$$\begin{aligned} \rho \frac{\partial T}{\partial t} = & -\rho \left(\vec{v} \cdot \vec{\nabla} \right) T - (\gamma - 1) \rho T \vec{\nabla} \cdot \vec{v} \\ & + \vec{\nabla} \cdot \left(\kappa_\perp \vec{\nabla}_\perp T + \kappa_\parallel \vec{\nabla}_\parallel T \right) + S_T \end{aligned} \tag{2.74}$$

with the definitions

$$\vec{B} = F_0 \vec{\nabla} \phi + \vec{\nabla} \Psi \times \vec{\nabla} \phi \,, \tag{2.75}$$

$$j = -R^2 \vec{\nabla} \phi \cdot \vec{j} = \frac{1}{\mu_0} \Delta^* \Psi \,, \tag{2.76}$$

$$\vec{\nabla} u = -\frac{1}{F_0} \left(\frac{\partial}{\partial t} \left(\Psi \vec{\nabla} \phi \right) + \vec{E} \right) , \tag{2.77}$$

$$\vec{v} = v_\parallel \vec{B} + R^2 \vec{\nabla} \phi \times \vec{\nabla} u \,, \tag{2.78}$$

$$W = \vec{\nabla} \phi \cdot \left(\vec{\nabla} \times \vec{v}_\perp \right) = \vec{\nabla}_\perp^2 u \,. \tag{2.79}$$

The heat diffusion term has been split into parts parallel and perpendicular to the magnetic field. Equations (2.70 – 2.76) are solved simultaneously as one large implicit system of equations in the finite-element code *JOREK*. For details, refer to Chapter 6.
The approximations of the reduced MHD model are, for instance, discussed in more detail in [Biskamp1993].

Chapter 3.

MHD equilibrium

3.1. Ideal MHD equilibrium

To design a nuclear fusion device based on a magnetically confined plasma it is crucial to find an equilibrium configuration which fulfills the following two conditions:

1. It should have good particle and energy confinement properties.
2. It must provide macroscopic stability.

Starting from the ideal MHD equations (Eqs. (2.33 – 2.39)), a static ($\vec{v} \equiv 0$) equilibrium can be determined by assuming $\partial_t \equiv 0$. This leads to the set of equilibrium equations

$$\vec{j} \times \vec{B} = \vec{\nabla} p\,, \tag{3.1}$$

$$\vec{\nabla} \times \vec{B} = \mu_0 \vec{j}, \tag{3.2}$$

$$\vec{\nabla} \cdot \vec{B} = 0\,. \tag{3.3}$$

Thus, in states of equilibrium, the magnetic force $\vec{j} \times \vec{B}$ balances the pressure gradient force $\vec{\nabla} p$. As the movement of plasma particles perpendicular to a magnetic field is restricted by the Lorentz force to a gyration, but the particles can move freely along the field lines, particle transport as well as energy transport by heat conduction are much stronger parallel to the magnetic field than perpendicular to it. Hence, to meet condition 1, the equilibrium configuration should ensure that magnetic field lines do not leave the plasma. That is why toroidal geometries are favorable.
One toroidal configuration, the so-called *tokamak*, which is the currently best understood device for magnetic fusion, is presented in the following section. A detailed discussion of MHD equilibrium theory can be found in Reference [Freidberg1987].

3.2. Tokamaks

A tokamak is an axisymmetric toroidal plasma confinement configuration. The principal magnetic field in a tokamak is a toroidal field produced by poloidal magnetic coils. But as a purely toroidal field is not sufficient to provide a plasma equilibrium, a weaker poloidal magnetic field component needs to be added in order to confine the plasma. The poloidal magnetic field is mainly produced by a toroidal plasma current induced by a transformer. A smaller contribution

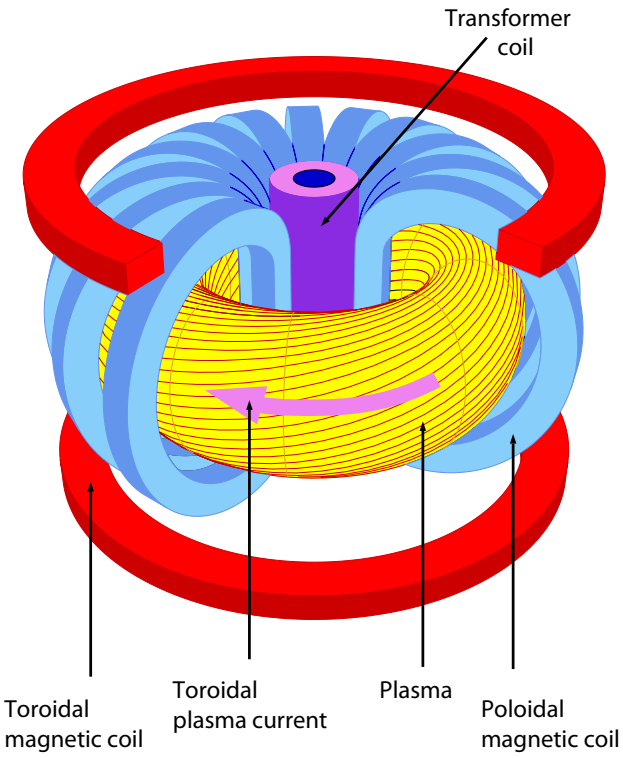

Figure 3.1.: Principal features of a tokamak.

also comes from extra toroidal magnetic coils which are required to control plasma shape and position, and to balance the hoop-force which tends to expand the plasma ring. The principal features of a tokamak are shown in Figure 3.1.

The resulting magnetic field lines wind helically around the torus as shown in Figure 3.2.To describe the geometry of these helical field lines, the *safety factor q* is introduced. It is locally defined as the ratio between the change of the toroidal angle $\Delta\phi$ and the change of the poloidal angle $\Delta\theta$ along a field line, thus

$$q = \frac{\Delta\phi}{\Delta\theta}\,. \tag{3.4}$$

For $\Delta\theta = 2\pi$ this yields a global definition of the safety factor as the number of toroidal rotations a magnetic field line completes during one poloidal rotation. If the safety factor has a rational value, the field line follows a closed path.

From axisymmetry, it follows that the magnetic field lines wind around the torus on nested toroidal surfaces as shown in Figure 3.3. These surfaces are called *magnetic flux surfaces*. As

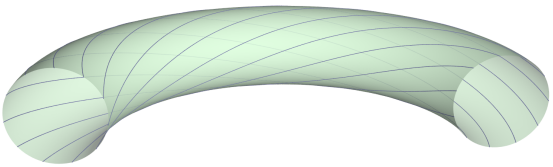

Figure 3.2.: Magnetic field lines, resulting from the superposition of a toroidal and a poloidal magnetic field, winding helically around the plasma torus.

equation (3.1) yields

$$\vec{B}\cdot\vec{\nabla}p = 0 \qquad \textit{and} \tag{3.5}$$

$$\vec{j}\cdot\vec{\nabla}p = 0\,, \tag{3.6}$$

magnetic flux surfaces are surfaces of constant pressure and $\vec{j}$ also lies in these surfaces. Note, that also the globally defined q is the same for all field lines located in a common flux surface.

In so-called *limiter configurations*, the last closed magnetic flux surface is defined by a solid surface touching the plasma at some point. It can also be defined by the magnetic field structure itself, in this case the magnetic field has an *X-point* where the poloidal magnetic field vanishes. The last closed magnetic flux surface is then called *separatrix*. Devices built for plasma configurations with X-point often contain *divertor plates* which are stroke by open field lines close to the plasma. The material, form, position and cooling of these plates are optimized to withstand the large heat flux coming from the plasma and to minimize the influx of impurities into the plasma. A divertor configuration is shown in Figure 3.4.

One of the largest tokamaks currently in operation is the German ASDEX Upgrade[1]. It is designed for D-shaped X-point plasmas and contains divertor plates. It has a major radius of 1.65 m and a minor radius of 0.5 m. Other important tokamak experiments are, for instance, DIII-D in San Diego, USA, and JET in Abingdon, UK. The next step towards a nuclear fusion

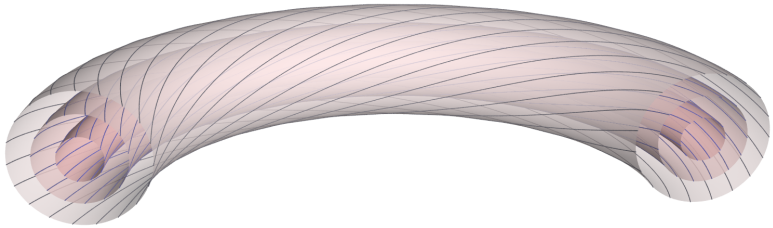

Figure 3.3.: Magnetic flux surfaces in a plasma with circular cross section.

[1] Its design is based on the Axial Symmetric Divertor EXperiment (ASDEX).

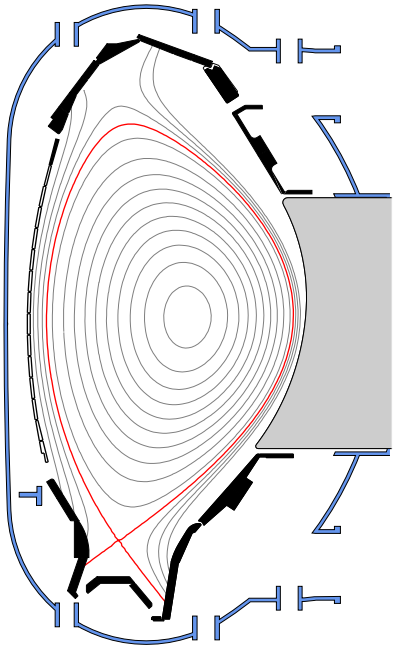

Figure 3.4.: Poloidal plane of an X-point plasma in a divertor configuration (ASDEX Upgrade). The grey lines illustrate magnetic flux surfaces and the red line represents the separatrix.

reactor is the ITER tokamak which is currently being built by an international cooperation in France.
An axisymmetric tokamak equilibrium can be described by a single scalar nonlinear partial differential equation, called *Grad-Shafranov equation* discussed in the following section. Very broad as well as detailed information about tokamaks can be found in Reference [Wesson2004].

3.3. Grad-Shafranov equation

The Grad-Shafranov equation describes the ideal MHD equilibrium of axisymmetric toroidal systems in terms of the poloidal magnetic flux and two free functions. It is expressed in cylindrical coordinates which are defined in Figure 2.1.
To obtain the Grad-Shafranov equation from the general ideal MHD equilibrium equations (3.1 – 3.3), the first step is to express $\vec{B}$ and $\vec{j}$ in terms of the poloidal magnetic flux Ψ. From equation (3.3) and axisymmetry it follows that $\vec{B}$ can be written as

$$\vec{B} = B_\phi \vec{e}_\phi + \frac{1}{R}\vec{\nabla}\Psi \times \vec{e}_\phi \,. \tag{3.7}$$

Inserting this expression into Ampère's law (3.2) yields

$$\mu_0 \vec{j} = -\mu_0 \frac{1}{R} \Delta^* \Psi \vec{e}_\phi + \frac{1}{R} \vec{\nabla} \left(R B_\phi \right) \times \vec{e}_\phi \,, \tag{3.8}$$

where Δ^* denotes the Grad-Shafranov operator introduced in Section 2.5. Note that Equations (3.7) and (3.8) correspond to Equations (2.75) and (2.76) for the more general case that B_ϕ cannot necessarily be written as $B_\phi = F_0/R$.
As the poloidal magnetic flux Ψ is constant on magnetic flux surfaces, it can be used to label these. Thus, quantities which are constant on magnetic flux surfaces can be written as a function of Ψ. Hence, from Equation (3.5) it follows that

$$p = p(\Psi) \,. \tag{3.9}$$

Combining (3.6) and (3.8) yields

$$\vec{e}_\phi \cdot \left(\vec{\nabla} p \times \vec{\nabla} \left(R B_\phi \right) \right) = 0 \,, \tag{3.10}$$

which implies that RB_ϕ is also constant on magnetic surfaces and thus allows to define a function $F(\Psi)$[2] as

$$F(\Psi) = R B_\phi \,. \tag{3.11}$$

Note, that the information contained in the components of the ideal equilibrium force balance equation (3.1) along $\vec{B}$ and $\vec{j}$ has been used to define $p(\Psi)$ and $F(\Psi)$. Now, the third component which is normal to the magnetic flux surface is used to finally obtain the Grad-Shafranov equation. Therefore, Equations (3.7), (3.8), (3.9) and (3.11) are inserted into $\vec{\nabla}\Psi \cdot \left[\vec{j} \times \vec{B} = \vec{\nabla} p \right]$ which yields

$$\Delta^* \Psi = -\mu_0 R^2 \frac{dp}{d\Psi} - F \frac{dF}{d\Psi} \,. \tag{3.12}$$

where

$$\vec{\nabla} p(\Psi) = \frac{dp}{d\Psi} \vec{\nabla} \Psi \qquad \text{and} \tag{3.13}$$

$$\vec{\nabla} F(\Psi) = \frac{dF}{d\Psi} \vec{\nabla} \Psi \tag{3.14}$$

have been used. With the appropriate choice for the free functions $p(\Psi)$ and $F(\Psi)$ and the boundary conditions, a particular equilibrium configuration can be described. More details about the Grad-Shafranov equation can for instance be found in References [Freidberg1987] or [Wesson2004].

[2] Note, that $F(\Psi)$ is proportional to the poloidal plasma current $I_{pol} = 2\pi R B_\phi / \mu_0$.

Chapter 4.

MHD stability

4.1. Linear ideal MHD stability analysis

As already stressed in Section 3.1, a nuclear fusion device needs to be based on an equilibrium configuration which does not only ensure good confinement, but also provides macroscopic stability. A system in equilibrium is stable, if the forces resulting from a perturbation drive the system back towards the equilibrium state. If these forces amplify the initial perturbation, the system is unstable.
In the following, a linear stability analysis is presented. The linear approach is sufficient to predict if an instability will occur or not, but it does not describe properly its further evolution or saturation level. In most cases, MHD instabilities are so disastrous for tokamak plasmas, that the primary goal of stability analysis is to learn how to avoid them, rather than to examine their nonlinear behavior, which justifies the important role of linear stability analysis. Nevertheless, there are instabilities, for example *edge-localized modes* which are discussed in Chapter 5, whose nonlinear evolution is crucial for the confinement properties of the plasma.
Now, the stability of the general ideal MHD equilibrium is analyzed starting from the linearized ideal MHD equations. Given a static ($\vec{v}_0 = 0$) ideal MHD equilibrium described by

$$\vec{j}_0 \times \vec{B}_0 = \vec{\nabla} p_0 \,, \tag{4.1}$$

$$\vec{\nabla} \times \vec{B}_0 = \mu_0 \vec{j}_0 \,, \tag{4.2}$$

$$\vec{\nabla} \cdot \vec{B}_0 = 0 \,, \tag{4.3}$$

all quantities $Q(\vec{x},t)$ are linearized around this state of equilibrium, i.e., expressed as the sum of their equilibrium value $Q_0(\vec{x})$ and a small perturbation $\tilde{Q}_1(\vec{x},t)$, thus

$$Q\left(\vec{x},t\right) = Q_0\left(\vec{x}\right) + \tilde{Q}_1\left(\vec{x},t\right) \,, \tag{4.4}$$

where $\tilde{Q}_1/Q_0 \ll 1$. Now a vector $\tilde{\vec{\xi}}$, describing the perturbation of the plasma position, is defined by

$$\tilde{\vec{v}}_1 = \frac{\partial \tilde{\vec{\xi}}}{\partial t} \,. \tag{4.5}$$

Inserting the linearized quantities into the continuity equation (2.33), the adiabatic equation (2.39) and Faraday's law (2.36) combined with the generalized Ohm's law (2.35), omitting all

terms beyond first order in perturbed quantities, and integrating the obtained equations with respect to time, yields

$$\tilde{\rho}_1 = -\vec{\nabla}\left(\rho_0 \tilde{\vec{\xi}}\right), \tag{4.6}$$

$$\tilde{p}_1 = -\tilde{\vec{\xi}} \cdot \vec{\nabla} p_0 - \gamma p_0 \vec{\nabla} \cdot \tilde{\vec{\xi}}, \tag{4.7}$$

$$\tilde{\vec{B}}_1 = \vec{\nabla} \times \left(\tilde{\vec{\xi}} \times \vec{B}_0\right), \tag{4.8}$$

where the initial conditions have been chosen as

$$\tilde{\vec{\xi}}\left(\vec{x},0\right) = \tilde{\vec{B}}_1\left(\vec{x},0\right) = \tilde{\rho}_1\left(\vec{x},0\right) = \tilde{p}_1\left(\vec{x},0\right) = 0, \tag{4.9}$$

$$\tilde{\vec{v}}_1\left(\vec{x},0\right) \neq 0. \tag{4.10}$$

Now, Equations (4.6 – 4.8) are substituted into the linearized force balance equation, and the linearized Ampère's law is used to eliminate $\tilde{\vec{j}}_1$, to obtain

$$\rho_0 \frac{\partial^2 \tilde{\vec{\xi}}}{\partial t^2} = \vec{F}\left(\tilde{\vec{\xi}}\right), \tag{4.11}$$

where the *force operator* $\vec{F}(\tilde{\vec{\xi}})$ is defined by

$$\begin{aligned}\vec{F}\left(\tilde{\vec{\xi}}\right) = {} & \frac{1}{\mu_0}\left(\vec{\nabla} \times \vec{B}_0\right) \times \left[\vec{\nabla} \times \left(\tilde{\vec{\xi}} \times \vec{B}_0\right)\right] + \frac{1}{\mu_0}\left(\vec{\nabla} \times \left[\vec{\nabla} \times \left(\tilde{\vec{\xi}} \times \vec{B}_0\right)\right]\right) \times \vec{B}_0 \\ & + \vec{\nabla}\left(\tilde{\vec{\xi}} \cdot \vec{\nabla} p_0 + \gamma p_0 \vec{\nabla} \cdot \tilde{\vec{\xi}}\right),\end{aligned} \tag{4.12}$$

and thus only depends on equilibrium quantities and $\tilde{\vec{\xi}}$. It is possible to separate the time-dependency by the ansatz

$$\tilde{\vec{\xi}}\left(\vec{x},t\right) = \vec{\xi}\left(\vec{x}\right) \exp\left(-\mathrm{i}\omega t\right). \tag{4.13}$$

Now, Equation (4.11) becomes

$$-\omega^2 \rho_0 \vec{\xi} = \vec{F}\left(\vec{\xi}\right). \tag{4.14}$$

This approach is called the *normal-mode formulation*.
Equation (4.14) represents an eigenvalue equation with eigenvalues ω^2. As it can be proven that the force operator is self-adjoint, the eigenvalues are real. Thus, ω is imaginary if $\omega^2 < 0$ which corresponds to an exponentially growing perturbation. This is the unstable case, where $\gamma \equiv \mathrm{i}\omega$ defines the *growth rate* of the mode. If ω is real instead, the system oscillates around its equilibrium position with frequency ω and thus is stable.
As it is in general a complex numerical problem to determine the eigenfunctions of $\vec{F}(\vec{\xi})$, a *variational formulation* of the problem is often used to analyze stability. It is obtained by multiplying

Equation (4.14) with $\vec{\xi}$ and integrating over the plasma volume which yields

$$\frac{\omega^2}{2}\int \rho_0 \vec{\xi}^2 \,\mathrm{d}V = -\frac{1}{2}\int \vec{\xi}\cdot\vec{F}\left(\vec{\xi}\right)\mathrm{d}V\,. \tag{4.15}$$

The left hand side of Equation (4.15) can be identified as the kinetic energy of the system, while the right hand side describes the potential energy δW. Now, stability depends on δW, as $\int \rho_0 \vec{\xi}^2 \,\mathrm{d}V$ is always positive. The system is stable if no test function $\vec{\xi}$ exists for which $\delta W < 0$. Otherwise, the potential energy can be reduced by an instability. Note, that in case of an instability, ω represents only a lower limit for the growth rate as the test function $\vec{\xi}$ is in general not an eigenfunction of $\vec{F}(\vec{\xi})$.
Further examination of δW shows that it can be expressed as the sum of a term describing magnetic field energy in the vacuum region which is always positive, a term describing the contribution of the plasma surface which can be neglected in cases without surface currents and a contribution from the plasma volume. This last part δW_V consists of three positive, thus stabilizing terms describing wave energies, and two terms which can have a destabilizing effect. These two terms are

$$\delta W_{V,p} = -\int \left(\vec{\xi}_\perp\cdot\vec{\nabla}p_0\right)\left(\vec{\kappa}\cdot\vec{\xi}_\perp\right)\mathrm{d}V\,, \tag{4.16}$$

$$\delta W_{V,j} = -\frac{1}{2}\int \frac{j_{0,\parallel}}{\left|\vec{B}_0\right|}\left(\vec{\xi}_\perp\times\vec{B}_0\right)\cdot\vec{B}_1\,\mathrm{d}V\,, \tag{4.17}$$

where the indices $\perp$ and $\parallel$ label vectors perpendicular and parallel to the equilibrium magnetic field, respectively, and $\vec{\kappa}$ denotes the curvature of $\vec{B}_0$ given by

$$\vec{\kappa} = \frac{\left(\vec{B}_0\cdot\vec{\nabla}\right)\vec{B}_0}{\left|\vec{B}_0\right|}\,. \tag{4.18}$$

If $\delta W_{V,p}$ is the dominant destabilizing term, the resulting instabilities are called *pressure-driven modes* as $\delta W_{V,p}$ depends on the pressure gradient. As $\delta W_{V,j}$ depends on the parallel component of the current density, instabilities due to this contribution are called *current-driven modes*. In many cases, instabilities are both pressure- and current-driven.
To analyze the stability of a tokamak configuration, an expansion in the inverse aspect ratio

$$\varepsilon = \frac{a}{R_0}\,, \tag{4.19}$$

where a denotes the minor radius of the plasma torus and R_0 denotes its major radius, is carried out. Thus, the zero-order approximation would be to describe the torus as a cylinder which is periodic in z with period $2\pi R_0$. To characterize instabilities in tokamaks, it is useful to express

$\vec{\xi}(\vec{x})$ as a Fourier series

$$\vec{\xi}(\vec{x}) = \sum_{m,n=-\infty}^{\infty} \vec{\xi}_{mn}(r) \exp\left[-\mathrm{i}\left(m\theta + n\phi\right)\right], \tag{4.20}$$

where m and n are called poloidal and toroidal mode numbers, respectively, and r denotes the local minor radius (see Figure 2.1). The mode numbers allow to describe the mode structure of a perturbation by characterizing its periodicity in poloidal and toroidal direction. Magnetic flux surfaces where the perturbation has the same structure as the magnetic field lines, i.e.,

$$q = \frac{m}{n}, \tag{4.21}$$

are called *resonant surfaces*. Resonant surfaces are particularly susceptible to instabilities, because the perturbation is parallel to the equilibrium magnetic field such that the stabilizing effect of field line bending vanishes. Ideal MHD stability analysis and MHD instabilities are for instance discussed in detail in References [Freidberg1987], [Wesson2004] and [Zohm2004].

4.2. MHD instabilities in tokamaks

As discussed in Chapter 4, ideal MHD instabilities can be driven by pressure gradient and parallel current density. In the vincinity of the resonant surface, stabilizing terms reflecting the stabilizing effect of field line bending are diminished, such that the destabilizing terms become important. Pressure-driven instabilities are strongly localized in the region of the resonant surface and constant along a magnetic field line. As can be seen from (4.16) the pressure term is destabilizing if the curvature $\vec{\kappa}$ of the equilibrium magnetic field is parallel to the pressure gradient and stabilizing in the antiparallel case. If the field curvature is parallel to the pressure gradient, flux tubes from the region of lower pressure are moved towards the region of higher pressure, as this shortens the field lines and thus reduces the magnetic field energy. Flux tubes from the region of high pressure are moved in the opposite direction, which reduces the internal energy of the plasma. This instability is called *interchange instability*.
As the interchange of flux tubes is hindered if neighboring flux tubes have a different pitch angle, i.e., a different q, the magnetic shear, defined by $s = dq/dr$, has a stabilizing effect on interchange instabilities. In tokamaks, the curvature of the equilibrium magnetic field is destabilizing in the outer half of the torus and stabilizing in the inner half. Hence, the average curvature along a field line determines the stability. The condition for stability against interchange instabilities in tokamaks as a function of the magnetic shear is given by the *Mercier criterion*. It predicts stability for $q > 1$.
A second kind of pressure-driven instability can occur if the pressure is very high and the perturbation is not constant along the equilibrium magnetic field lines on the resonant surface. The latter corresponds to a superposition of the mode which satisfies $q = m/n$ with other modes which do not exactly satisfy this condition, yielding an asymmetry in the resulting amplitude of the perturbation. This asymmetry can have a destabilizing effect if the amplitude of the perturbation is higher in the region of destabilizing curvature than in the region of stabilizing curvature.

The resulting instability is called *ballooning instability*. Stabilizing effects are an increased magnetic shear and a non-circular plasma shape which ensures that the magnetic field lines stay longer in regions of stabilizing curvature.
The second driving source for instabilities is the current term (4.17). Current-driven instabilities are also called *kink modes*. There are two different types of kink modes, namely the *internal kink* and the *external kink*. Whereas the former does not perturb the plasma-vacuum interface, the latter causes a motion of the plasma surface away from its equilibrium position.
Internal kinks can occur if $m = 1$ and $q(r = 0) \leq 1$. Then, the $(m,n) = (1,1)$ internal kink is the most unstable. The stability criterion limits the current density on the axis $j(0)$.
The stability against external kink modes depends on the position of the resonant surface. If it is located outside the plasma, the system can become unstable, especially if the resonant surface is close to the plasma surface. For large poloidal mode numbers, the stability depends on the current density profile. A high current density near the plasma surface destabilizes the external kink mode. For $m = 1$, the stability criterion is given by the *Kruskal-Shafranov limit*, which predicts instability if $q(r = a) < 1$. This represents a limit to the total plasma current.
Low-m external kinks can be stabilized by an ideally conducting wall surrounding the plasma close to its surface. The perturbation of the magnetic field induces mirror currents in the ideal wall which annihilate the magnetic field perturbation in the wall and attenuate it at the resonant surface. This stabilizing effect is stronger for modes with low poloidal mode numbers, as their radial extension into the vacuum field decays less strongly.
So far, only ideal MHD stability theory has been discussed and non-ideal effects as for example non-vanishing resistivity have been neglected. Taking resistivity into account, magnetic flux conservation is no longer valid, hence the structure of the magnetic field can be changed by instabilities. This allows additional instabilities to occur where ideal MHD theory predicts stability. A common resistive MHD instability in tokamaks is the *tearing mode*, a resistive current-driven instability during which magnetic field lines tear and reconnect. All instabilities predicted by linear ideal MHD theory will also occur in the resistive case, but their further non-linear development can be strongly affected by resistivity.

Chapter 5.

Edge-localized modes

5.1. H-regime

The *H-regime*, also called *H-mode*, is an operational regime for tokamak plasmas where the energy and particle confinement is significantly increased compared to the standard regime, also called *L-regime* or *L-mode*. The transition from L-regime to H-regime takes place at a certain input power threshold. It is observed that above this threshold, the transport in a narrow zone at the plasma edge called pedestal is suddenly reduced, such that particles and energy, which diffuse from the plasma center to the edge, accumulate in front of this transport barrier and steep density and temperature gradients build up at the edge as shown in Figure 5.1. Even if various aspects of the phenomenon have been explained, up to now, a self-consistent model explaining the L-H transition has not been found.
Although the enhanced energy and particle confinement is of course desirable, it also causes some problems. Firstly, an uncontrolled increase in density can cause the plasma to fall back to the L-mode. Secondly, also the confinement of impurities, such as heavy ionized atoms from the walls, is improved, which leads to a larger loss of energy by radiation. The steep density and temperature gradients at the edge of an H-mode plasma can cause an additional kind of instability as discussed in the following section.

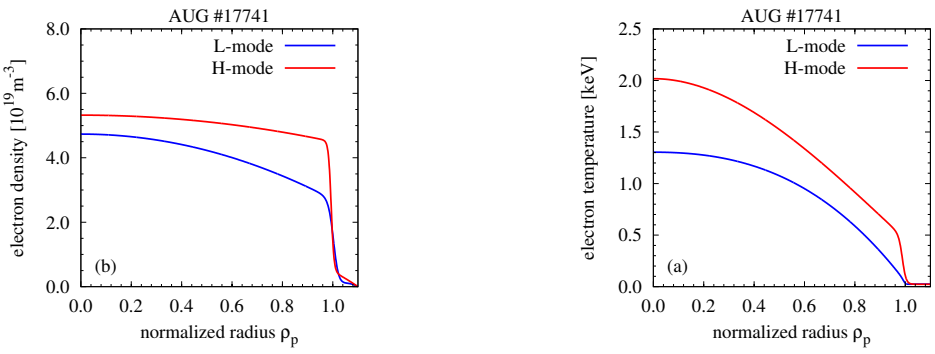

Figure 5.1.: Comparison of typical L- and H-mode electron density and temperature profiles in ASDEX Upgrade. The figures are taken from Reference [Schneider2012], by courtesy of Philip A. Schneider.

5.2. Edge-localized modes

An edge-localized mode (ELM) is a special kind of instability localized at the plasma edge which is only observed in H-mode plasmas. It is caused by the steep temperature and density edge gradients characterizing the H-regime. ELMs are relaxation-oscillations, each event ejects particles and energy, which have been accumulated in front of the H-mode transport barrier. This reduces the steep gradients to some degree. The system thus becomes stable and edge gradients can build up again until the next ELM event is triggered. One ELM event takes about 0.3-1 ms and can reduce the particle and energy content of the plasma by 5-10 % [Zohm1996]. During the ELM, a high level of magnetic fluctuations is measured. The ejected plasma filaments formed by an ELM are shown in Figure 5.2.
ELMs have first been observed in the ASDEX tokamak [Keilhacker1984]. As for the H-regime, there is no comprehensive theoretical understanding of this instability up to now. MHD modes which often are observed before ELMs, suggest an MHD instability as underlying mechanism. A simplified picture of the underlying MHD instability, the peeling-ballooning model, is sketched below.

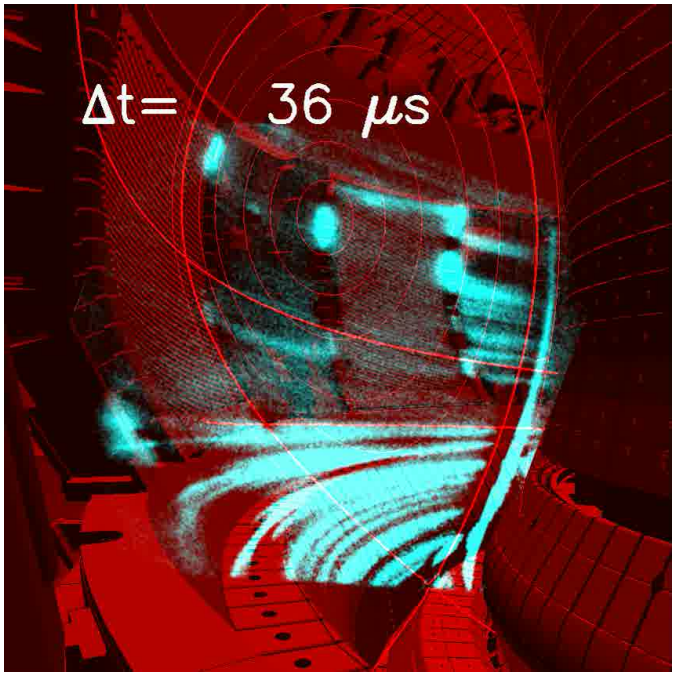

Figure 5.2.: Fast camera picture of ELM filaments in ASDEX Upgrade (blue). To render the filaments visible, the time averaged signal over about half a millisecond has been substracted from the data. A CAD picture of the wall structure and a poloidal cut of the equilibrium flux surfaces are plottet in red. Courtesy of Tilmann Lunt.

ELMs can have both favorable and negative effects on the performance of a nuclear fusion

device which is operating in H-mode. On one hand, the performance is limited because ELMs deteriorate the particle and energy confinement. Additionally, ELMs may cause very high heat fluxes which can damage the plasma facing components of the device, especially the divertor plates. Extrapolations predict that in ITER, energies released per ELM event could reach up to approximately 20 MJ [Loarte2003], which is not acceptable for the plasma facing components. On the other hand, ELMs have two advantages that can be crucial for stationary H-mode operation. Firstly, the ejection of particles allows to control the density which is necessary to avoid a throwback to the L-regime. Secondly, ELMs remove impurities from the plasma.
Hence, whether the H-mode is a stable operational regime suitable for future nuclear fusion devices strongly depends on the occurrence of ELMs, their exact properties and if these can be controlled.
According to the properties observed in experiments, ELMs are often classified into three different types. *Type-I ELMs* cause the largest energy and particle losses and thus the highest heat flux densities at the divertor. They have the lowest repetition rate (about 10-200 Hz depending on the size of the device), which increases if the energy flux through the separatrix is increased. The energy flux is given by the heating power subtracting volumetric power losses, for instance by radiation.
Whereas type-I ELMs are dominant for high input power levels, *type-III ELMs* already appear little above the L→H transition threshold. Type-III ELMs occur with a higher frequency (about 200-2000 Hz) which, in contrast to the type-I ELM frequency, decreases with increasing energy flux through the separatrix. The energy and particle losses and the divertor heat load during a type-III ELM are much smaller than during a type-I ELM. Type-III ELMs are preceded by a coherently oscillating magnetic perturbation characterized by medium poloidal and toroidal mode numbers $m \approx 10-15$ and $n \approx 5-10$. Similar precursor modes have also been found at type-I ELMs [Kass1998].
Type-II ELMs are small, high frequency events like type-III ELMs, but they are observed at high pressure gradients similar to type-I ELMs. For the occurrence of type-II ELMs the plasma shape plays a major role.
There are different concepts to actively control the ELM size. One possibility is ELM pacing by *pellet injection* where cryogenic hydrogen pellets are injected into the plasma to trigger ELMs at a higher frequency and decrease the energy loss per ELM. Another method are *resonant magnetic field perturbations* generated by non-axisymmetric coils which mitigate or suppress ELMs by ergodizing the magnetic field near the separatrix.
Even though a lot of progress has been made in controlling ELMs in existing tokamak experiments, a comprehension of the theoretical background of ELMs is crucial to predict the stability behavior of the H-regime and ELM sizes for future devices like ITER.
One approach to explain the most dangerous type-I ELM cycle qualitatively is the *peeling-ballooning model* illustrated in Figure 5.3. The figure describes the linear stability diagram of a plasma in the space given by edge current density and edge pressure gradient. According to the model, ELMs arise as an MHD instability from the coupling of a pressure driven ballooning mode with a current driven[1] external kink, or *peeling mode*. The cycle starts with a rise of

[1]The toroidal edge current density is also enhanced in the H-regime, because, as follows from neoclassical transport theory, a large pressure gradient in a toroidal plasma generates a toroidal current, called *bootstrap current*.

the pressure gradient (1) until it reaches a ballooning threshold (2). The pressure gradient increases faster than the current density, because the transport timescale is faster than the resistive timescale. Then, the current density increases (3) such that the plasma also becomes unstable with respect to peeling modes (4). This leads to the ELM crash (5) where particles and energy are expelled and edge pressure gradient and current density are reduced.The model cannot predict at which pressure gradient the ELM crash stops, thus it does not provide quantitative information about what happens during the ELM.

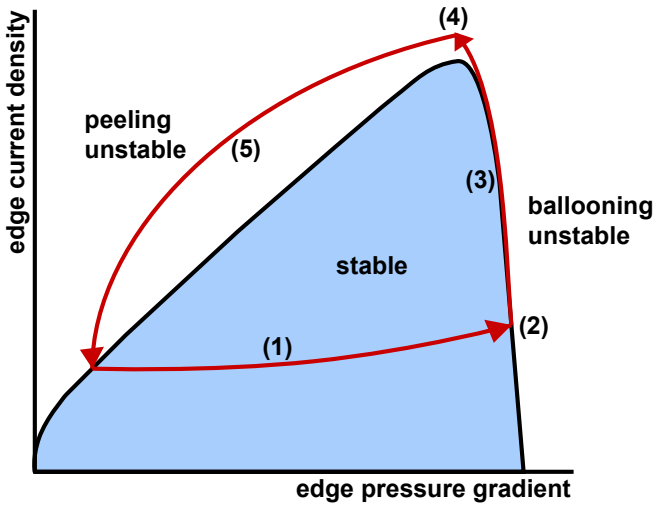

Figure 5.3.: Peeling-ballooning model of an ELM cycle.

As has been stressed, in the case of edge-localized modes, it is essential to be able to predict the non-linear evolution of the instability to obtain information about the duration of an ELM, energy and particle losses and the heat flux onto the plasma facing components. Thus, the use of numerical tools to study ELMs is indispensable. The reduced MHD code JOREK, which can be used to simulate ELMs non-linearly in realistic X-point geometry, is used for the simulations in the work at hand. The most important properties of the code are presented in the following chapter. An introduction into the physics of edge-localized modes can be found in References [Biskamp1993] and [Wesson2004] and an overview about the topic is given in References [Zohm1996], [Suttrop2000] and [Pamela2010].

Chapter 6.

The JOREK code

6.1. Numerical features of JOREK

The JOREK code solves the non-linear reduced MHD equations in full toroidal X-point geometry, including the separatrix and open field lines outside the separatrix. It has initially been developed especially for simulations of edge-localized modes by Huysmans [Huysmans2007]. More information about JOREK can be found in [Huysmans2008], [Czarny2008] and [Pamela2010]. For the spatial discretization, poloidal plane and toroidal direction are treated separately. In toroidal direction, the variables are discretized using Fourier harmonics. Besides from facilitating the numerics, the Fourier representation has the advantage, that the toroidal modes included in the simulation can be explicitely chosen[1]. This is particularly useful for ELMs where only a few intermediate mode numbers are the most unstable ones, such that it is not necessary to include arbitrarily high mode numbers to capture the dominant physics.
In the poloidal plane, *bi-cubic Bézier finite elements* are used for the discretization. A 2D Bézier element, also called *Bézier patch*, is parametrized by

$$\vec{P}(s,t) = \sum_{i=0}^{3}\sum_{j=0}^{3} \vec{P}_{ij}\tilde{B}_i(s)\tilde{B}_j(t)\,, \tag{6.1}$$

where s and t are local coordinates along the edges of the element, $(0 \leq s,t \leq 1)$, and the basis $\tilde{B}$ are the *Bernstein cubic polynomials*, defined by

$$\tilde{B}_0(x) = (1-x)^3\,, \tag{6.2}$$
$$\tilde{B}_1(x) = 3\,(1-x)^2\,x\,, \tag{6.3}$$
$$\tilde{B}_2(x) = 3\,(1-x)\,x^2\,, \tag{6.4}$$
$$\tilde{B}_3(x) = x^3\,, \tag{6.5}$$
$$0 \leq x \leq 1\,. \tag{6.6}$$

The coefficients $\vec{P}_{ij}$ correspond to 16 control points which determine the form of the Bézier surface (see Figure 6.1). Four of them are *vertices*, they determine the position of the corners of the patch. Two *tangent points* and a *twist point* belong to each vertex. The tangent points are

[1] This is done by specifying the number of included modes and the periodicity, i.e., the difference between successive mode numbers

associated with the tangents to the edges at the corner , $\partial\vec{P}/\partial s$ and $\partial\vec{P}/\partial t$, and the twist point is associated with the cross derivative $\partial^2\vec{P}/\partial s\partial t$ at this point. The requirement of continuity between adjacent Bézier patches leads to conditions on the relations between the control points and a reduction of the number of degrees of freedom.
The Bézier finite element method provides continuity of the variables and their first derivatives. In the *isoparametric* formulation implemented in JOREK, the same basis functions are used to describe the form of the elements (R and Z) and for the physical variables (Ψ, T, ...). This allows to align the finite elements precisely to the equilibrium flux surfaces which has computational advantages due to the different length scales of parallel and perpendicular gradients. A discussion of Bézier finite elements and their application in MHD simulations can be found in Reference [Czarny2008].

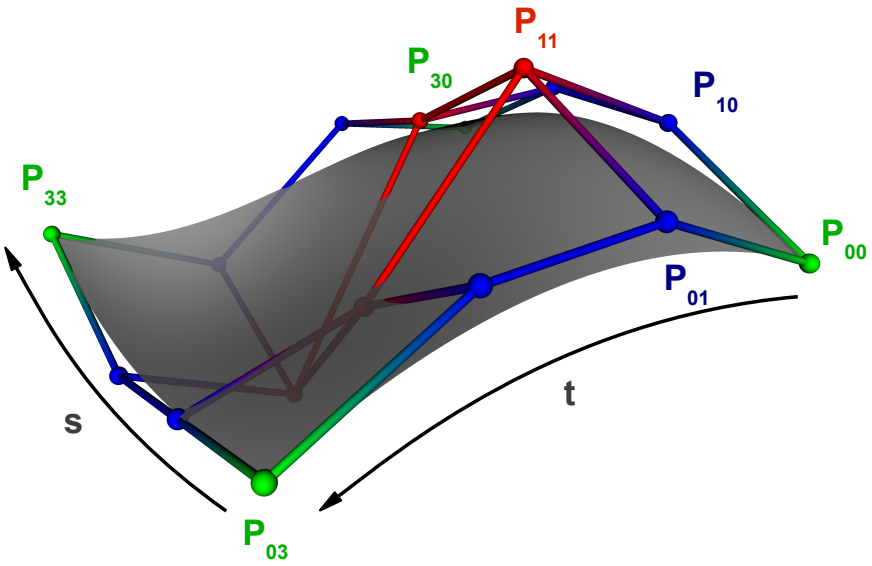

Figure 6.1.: Bézier patch with vertices (green), tangent points (blue) and twist points (red).

To apply the finite element method to the reduced MHD equations (Eqs. (2.70 – 2.74)), the equations are transformed into *weak form*. Therefore, the equations are multiplied by a test-function and integrated over the plasma volume. The test-functions are chosen equivalent to the basis functions of the finite element method, such that the integration can be carried out element-wise (Galerkin method). For integration over s and t, the method of Gauss quadrature is used. The integration over ϕ is carried out using fast Fourier transform.

The time integration in JOREK is performed according to the *Crank-Nicholson scheme*. For a system of ordinary differential equations of the form

$$\frac{d\vec{u}(t)}{dt} = H(\vec{u},t)\,, \tag{6.7}$$

where $\vec{u}$ is a vector of variables and H is a non-linear function or matrix operator, this scheme can be written as

$$\frac{\vec{u}_{n+1}-\vec{u}_n}{\Delta t} = \frac{1}{2}\left(H_{n+1}+H_n\right)\,, \tag{6.8}$$

where $\vec{u}_n = \vec{u}(t_n)$ and $H_n = H(\vec{u}_n,t_n)$ and t_n denotes the time after time-step n. The Crank-Nicholson scheme is, for instance, presented in Reference [Hirsch1988]. As the scheme is fully implicit, the time step can be chosen independently of the grid size and is only limited by numerical instabilities resulting from the non-linearity of the system. The disadvantage of an implicit scheme is, that in each time step, a huge system of equations has to be solved.
Linearization of this system of equations yields a matrix equation of the form $A\vec{x} = \vec{b}$, where $\vec{x}$ is the unknown vector and A is a sparse matrix. To solve this linear system of equations, JOREK uses the iterative GMRES method and the direct parallel sparse matrix solver *PastiX* ([Henon2002]) for the physics-based preconditioning needed by GMRES.
In JOREK, some physical quantities are normalized. The density and the current density are normalized by the density in the plasma center ρ_0 and the magnetic permeability μ_0, respectively. The other variables have to be normalized accordingly to preserve the consistency of the equations. This normalization leads to time scales near the Alfvén time typical for MHD. The normalization of all important quantities in JOREK is listed in Reference [Hoelzl2012]. Note, that the reduced MHD equations (Eqs. (2.70 – 2.74)) do not change due to the normalization, but the definition of j is changed to $j = \Delta^*\Psi$.
The boundary conditions implemented in JOREK are different for the different parts of the boundary. A typical flux surface aligned grid is shown in Figure 6.3. The main part of its boundary is located along the outermost open flux surface contained in the computational domain. This part of the boundary is treated as an ideally conducting wall, thus all perturbations vanish on the boundary. The part of the boundary which is crossed by magnetic field lines corresponds to the divertor target plates. There, the parallel velocity is forced to sound speed (Bohm condition, [Stangeby1995] and [Huysmans2008]) and density and temperature are allowed to outflow freely.

6.2. ELM simulations with JOREK

In the following, the main steps in the course of an ELM simulation with JOREK are presented[2]. At first, a grid which is aligned to the equilibrium flux surfaces has to be determined. For this

[2]The simulations presented in the work at hand have been made with JOREK code revisions #538 and #643. The physics model described above is called "model302" in JOREK.

purpose, the Grad-Shafranov equation (3.12) is solved on a polar grid of the desired form to obtain the poloidal magnetic flux on this domain. The free functions $p(\Psi)$ and $F(\Psi)$ as well as the boundary condition (given by the values of Ψ at the boundary of the domain) are taken, for instance, from the CLISTE equilibrium reconstruction code ([McCarthy1999]) which takes various measurements from a chosen discharge into account.
On the flux surface aligned grid, the Grad-Shafranov equation is solved again, using the equilibrium profiles from the reconstruction. The simulation is then run including only the $n = 0$ Fourier harmonic to achieve a quasi-steady state where the velocity has become steady. Having achieved such a quasi-steady state, higher Fourier harmonics can be included in the simulation. In case of instability, the unstable mode emerges from the initially small numerical noise.
The equilibrium reconstruction used for the simulations presented in this thesis is based roughly on the type-I ELMy H-mode discharge #23221 of the ASDEX Upgrade tokamak. The corresponding equilibrium profiles are plotted in Figure 6.2. This particular discharge has been chosen, because it is a typical example for this kind of discharge providing good diagnostic results for electron density and temperature. Note, that it has been taken as an approximate basis, but the simulations do not represent a reproduction of the discharge.

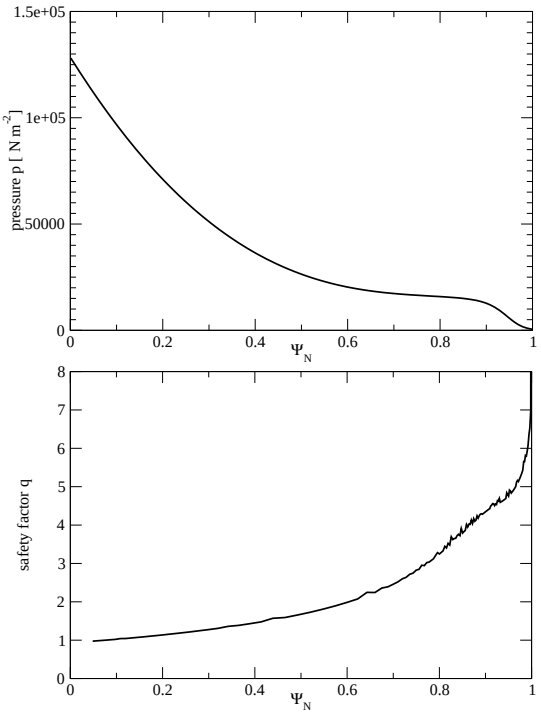

Figure 6.2.: Equilibrium pressure profile and q-profile, obtained from an equilibrium reconstruction of ASDEX Upgrade discharge #23221.

The most important physical parameters in JOREK are heat and particle diffusion coefficients, resistivity and perpendicular viscosity. In the simulations presented in this work, the perpendicular heat and particle diffusivities are constant throughout the plasma, except for the edge, where they decrease by about one order of magnitude to take account of the H-mode transport barrier. The heat diffusion anisotropy is $\kappa_\parallel / \kappa_\perp \approx 3.6 \cdot 10^7$ in the plasma core. The Spitzer-Härm prediction ([Spitzer1953]) for the heat diffusion anisotropy would be typically of the order 10^9–10^{10}, but there is theoretical as well as experimental evidence, that smaller values in the order of 10^8 are more realistic ([Hoelzl2009]).
The parallel particle diffusivity is set to zero, such that particle transport along the field lines is provided by convection only. The particle and heat sources and perpendicular diffusivities are chosen such that the background ρ- and T-profiles do not change significantly during the simulation.
Resistivity and viscosity are modeled with a $T_N^{-1.5}$ temperature dependency, where T_N is the temperature normalized to its value in the plasma core. The value of the resistivity in the plasma core is[3] $\eta_{\mathrm{SI}} \approx 2.5 \cdot 10^{-7}\,\Omega\mathrm{m}$. The perpendicular viscosity has been additionally enhanced in the plasma center to suppress undesired core instabilities, its value at the plasma center is $\mu_{\perp,\mathrm{SI}} \approx 6 \cdot 10^{-7}\,\mathrm{kgm^{-1}s^{-1}}$, which corresponds to a kinematic viscosity of about $\nu_{\mathrm{SI}} \approx 3\,\mathrm{m^2 s^{-1}}$. Whereas the viscosity is of the same order as realistic values, the resistivity is about one order of magnitude larger[4]. The consequence of a larger resistivity is a suppression of small scale structures that could not be resolved at the given grid resolutions. For simulations including many toroidal modes, this is the closest one can get towards realistic simulation parameters with current high performance computing resources and the current numerical implementation in JOREK.

[3] To convert normalized quantities into quantities in SI units, $\rho_0 = 2 \cdot 10^{-7}\,\mathrm{kg\,m^{-3}}$ has been used.

[4] A realistic value for η would be of the order of $10^{-8}\,\Omega\mathrm{m}$ at the parameters of the considered discharge ([Wesson2004]).

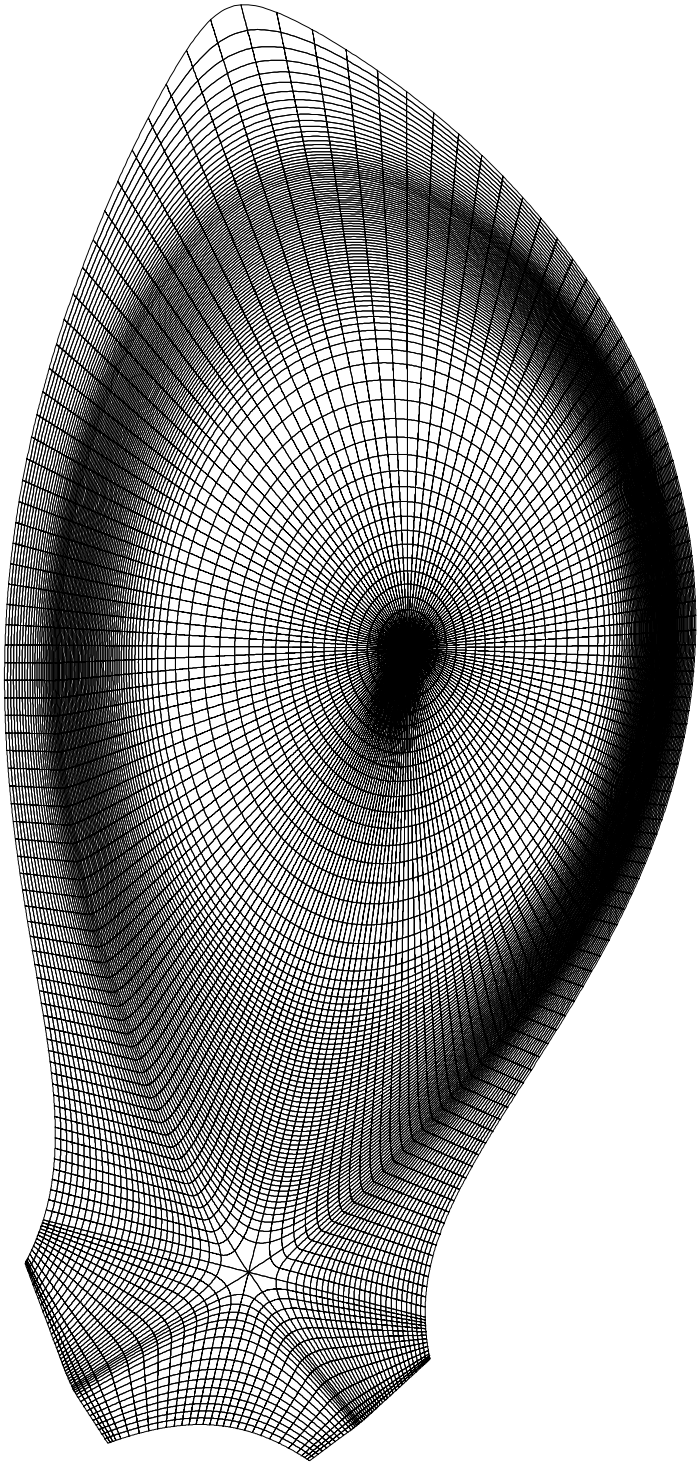

Figure 6.3.: Flux surface aligned grid resolving the plasma core and the region between separatrix and wall (scrape-off layer). The radial grid resolution is increased around the separatrix and the poloidal grid resolution around the X-point.

Part II.

Analysis of the mode structure and evolution in simulations of edge-localized modes

Chapter 7.

Introduction

In Part I of the thesis, the framework of magnetohydrodynamics has been introduced and the reduced MHD model has been presented. In the course of the discussion of MHD equilibrium and stability, the tokamak configuration for magnetic plasma confinement has been introduced and MHD instabilities in tokamaks have been adressed. One particular instability arising in tokamaks, namely edge-localized modes, have been discussed in more detail, underlining the importance of non-linear numerical simulations of ELMs for the successful operation of future tokamaks. The non-linear reduced MHD code JOREK, which has been developed for this purpose has been presented.
In Part II, the results of such simulations of edge-localized modes in ASDEX Upgrade geometry with JOREK are presented and analyzed. The discussion focuses on the evolution of the poloidal and toroidal Fourier harmonics of the perturbation. As an example, Figure 7 shows time traces of energy and growth rate of the different Fourier modes at the onset of an ELM in a simulation with JOREK including four toroidal modes ($n = 4, 8, 12, 16$). A general definition of the growth rate γ of a mode, introduced in Section 4.1, is given by

$$\gamma = \frac{1}{2}\frac{d\log E}{dt}, \tag{7.1}$$

where E is the energy contained in the mode. The energies of all modes in the simulation grow exponentially with a constant growth rate at the beginning. Subsequently, the growth rates of the subdominant modes rise due to nonlinear interaction with other modes. In the end, a saturation is observed.
The first phase, where nonlinear effects can be neglected, is called the *linear phase*, the constant growth rates in this phase are called *linear growth rates*. As can be seen, the linear growth rates differ for the various mode numbers. They can be analyzed by carrying out simulations where only one non-zero toroidal mode is included. The time evolution of the growth rate of the $n = 4$ mode in such a simulation is represented in Figure 7.2.

The discussion is divided into three parts, focusing on the linear mode growth, the non-linear evolution and the saturation. Chapter 8 treats the linear phase. The questions are addressed, how the linear growth rate depends on the toroidal mode number, how it is influenced by the distance between the plasma and an ideally conducting wall and if a critical wall distance beyond which its influence is negligible, can be found.
In Chapter 9, the nonlinear development of the mode structure is analyzed. It is shown, how the main characteristics of the evolution of the mode structure can be explained by the mode interaction between the toroidal modes. Furthermore, effects determining the mode saturation

are studied in Chapter 10.

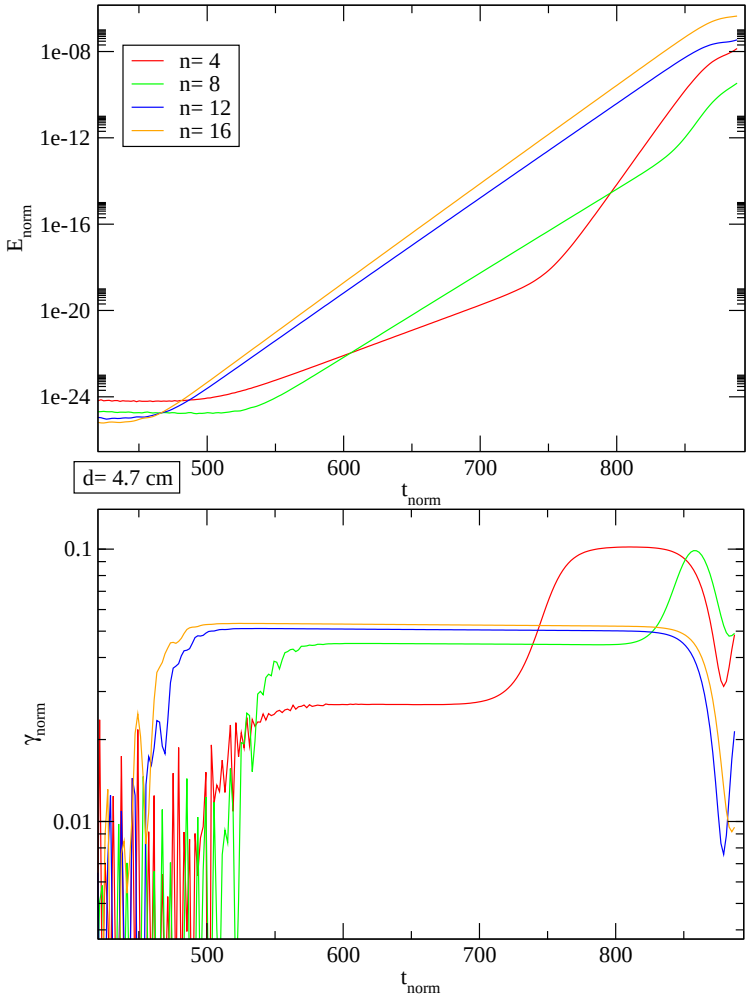

Figure 7.1.: Time evolution of the sum of magnetic and kinetic energies and the growth rate of the toroidal modes $n = 4, 8, 12, 16$. The fluctuations at the beginning, before the linear growth sets in, are due to numerical noise at very low energy levels. Quantities indexed with "norm" are normalized according to the normalization scheme used in JOREK (see Section 6.1).

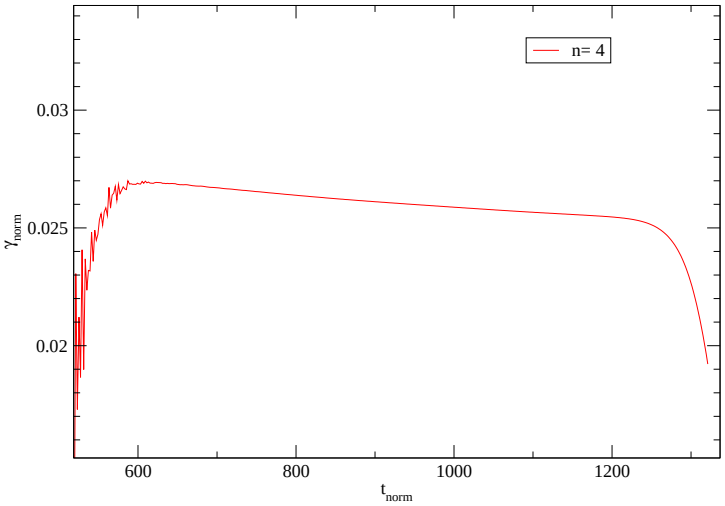

Figure 7.2.: Growth rate of the $n = 4$ mode in a simulation including only this toroidal harmonic. In contrast to Figure 7, where the growth rate of the $n = 4$ mode is increased by nonlinear interactions with the other modes, the growth rate in this simulations stays approximately constant until the saturation. The slight decrease of the linear growth rate is due to little changes in the background profiles, because the state of equilibrium is not perfectly steady.

The simulations

The ELM-simulations analyzed in Chapter 8 have been carried out with one single non-zero toroidal harmonic only. In order to compare growth rates of different toroidal modes and analyze the influence of the wall distance onto the growth rates, the toroidal mode numbers n have been varied between 2 and 20 and the distances between the separatrix and the ideally conducting wall d have been varied between 0.6 cm and 4.7 cm. The linear growth rates and the poloidal mode widths b at the midplane (see Figure 7.3) in these simulations have been determined. Higher toroidal mode numbers could not be considered due to computational limitations. To further increase the wall distances, the second inactive X-point would have to be taken into account in this discharge, making the flux surface aligned grid more complicated. A typical simulation needs at least 8 compute nodes (24 GB and 8 cores each) to meet the memory requirements of the solver and about 800 core hours. The simulations have been carried out on the HPC-FF computing cluster in Jülich, Germany.

To analyze how nonlinear mode coupling determines the mode structure in ELM simulations, the simulations discussed in Chapter 9 include several toroidal modes. The simulations have been carried out including the sets of toroidal modes $n = 4, 8, 12, 16$ and $n = 2, 4, 6, 8, 10, 12, 14, 16,$

with wall distances $d = 0.6\,\text{cm}$ and $d = 4.7\,\text{cm}$. A typical simulation with eight included toroidal harmonics needs at least 36 compute nodes (50 GB and 16 cores each) to meet the memory requirements of the solver and about 7000 core hours. These simulations have been run on the IFERC-CSC Helios computing cluster in Rokkasho, Japan.
In Chapter 10, the phase of saturation of the mode growth in simulations with one and with several included toroidal harmonics and varying wall distances is analyzed. For the analysis presented in this Chapter, the displacement of the density in radial direction ξ_ρ has been determined as shown in Figure 7.4. The mode structure of perturbations of the poloidal magnetic flux Ψ, the density ρ and the temperature T have been examined by Fourier analysis. The $(m,n) = (0,0)$ profiles of the current density and the temperature, density and pressure gradient have been determined by averaging the corresponding quantities over a set of flux surfaces.

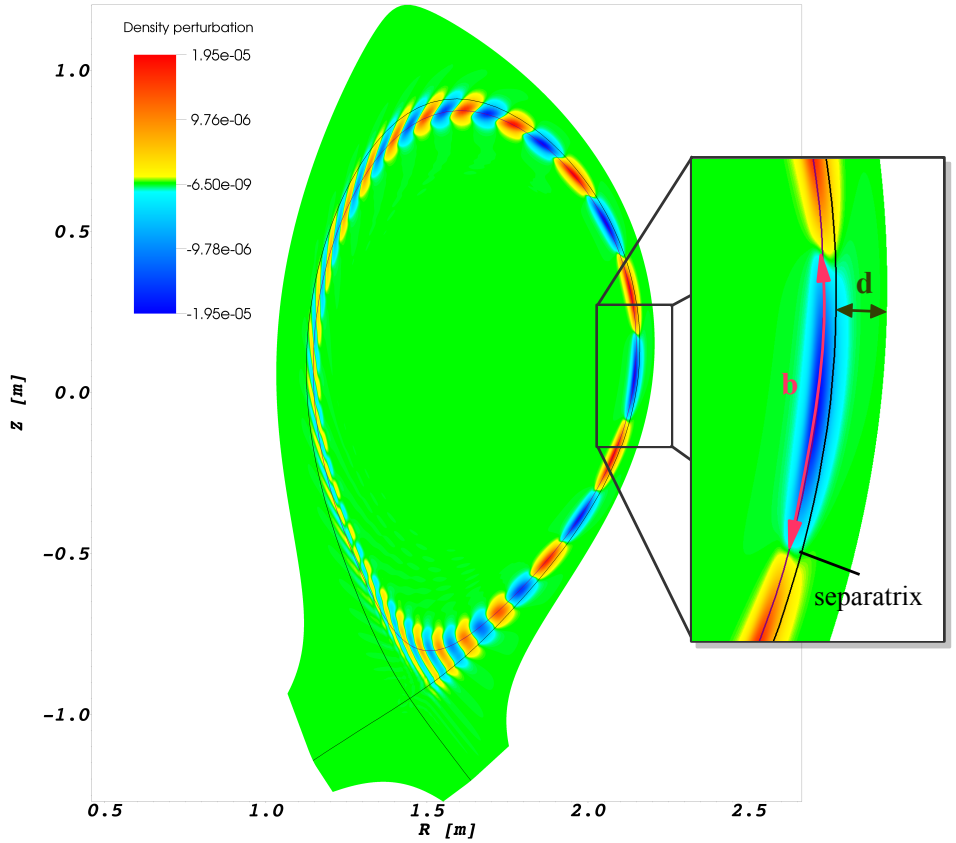

Figure 7.3.: Definition of the poloidal mode width b. The figure shows a poloidal cross section of the density perturbation with separatrix (black line) and the flux surface, where the density perturbation is maximal (dark red). Poloidal mode width b and wall distance d are determined at the outboard midplane. Note, that b denotes half the wavelength of the perturbation in poloidal direction.

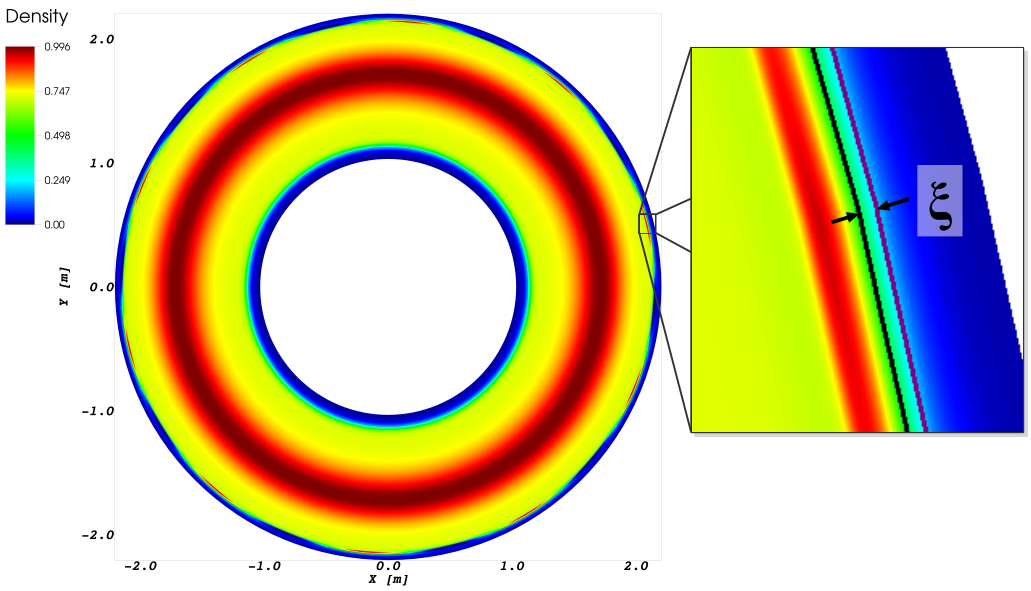

Figure 7.4.: Definition of the displacement of the density contours in radial direction ξ_ρ. The figure shows a toroidal cross section of the density at the midplane. The density perturbation is visible as red and dark blue spots at the outboard edge. The black line is a line of constant density at the separatrix in the unperturbed density profile. The violet line is a line of the same value of constant density in the perturbed plasma. Compared to the former, the latter is displaced inwards where the perturbation lowers the density and outwards where the perturbation enhances the density. The displacement ξ_ρ has been defined as the distance between these two lines at the toroidal angle of maximum perturbation amplitude.

Chapter 8.

Linear growth

As mentioned in Section 5.2, ELMs are typically characterized by intermediate toroidal mode numbers ($n \approx 5-10$) [Zohm1996]. Figure 8.1 shows the dependence of the growth rate on the toroidal mode number for different wall distances d in the simulations. As can be seen, also in the simulations the growth rates increase when the toroidal mode numbers increase from small to intermediate, but instead of decreasing for higher mode numbers they further increase. This is caused by the neglect of diamagnetic stabilization[1] in the code used for the simulations. This additional term would stabilize high mode numbers [Huysmans2001].
Note, that the n-dependence of the growth rate for the three highest mode numbers $n = 13, 16, 20$ has to be interpreted with care. In these simulations, the resolution might have been critical to resolve the small-scale structures of the modes, which might influence the growth rate. As resolution requirements only depend on the mode number, the dependence of the growth rate on the wall distance for fixed mode number should not be significantly affected.

In Figure 8.2 the growth rate is shown in terms of the wall distance for different toroidal mode numbers. The growth rates increase with increasing wall distance for given toroidal mode numbers, which shows clearly the stabilizing effect of an ideal wall close to the plasma discussed in Section 4.2. This stabilizing effect can be understood considering a simple model based on the energy balance

$$\delta W_p = \delta W_{kin} + \delta W_{vac}\,, \tag{8.1}$$

where δW_p is the magnetic energy released by the instability which is available as kinetic energy δW_{kin} deforming the plasma and as energy of the magnetic field in the vacuum region between the plasma and the wall δW_{vac}. Note, that these are the time-independent parts of the energies, where the time-dependency has been separated by the ansatz (4.13). The kinetic energy δW_{kin} can be expressed by

$$\delta W_{kin} = \gamma^2 \delta K\,, \tag{8.2}$$

where γ denotes the growth rate and $\delta K = \frac{1}{2}\int \rho_0 \vec{\xi}^2(\vec{x})\,dV$ [Freidberg1987]. Here ρ_0 is the equilibrium density and $\vec{\xi}(\vec{x})$ is the displacement of the plasma due to the perturbation defined

[1] The diamagnetic drift of the ions, caused by the pressure gradient and pointing in poloidal direction, has a stabilizing effect on ballooning modes, as it induces a shear and additionally carries the mode from the low- to the high-field side of the torus, where the magnetic field curvature is stabilizing. This effect can be important if the growth rate of the mode is lower than or comparable to the ion diamagnetic drift frequency ([Huysmans2001]).

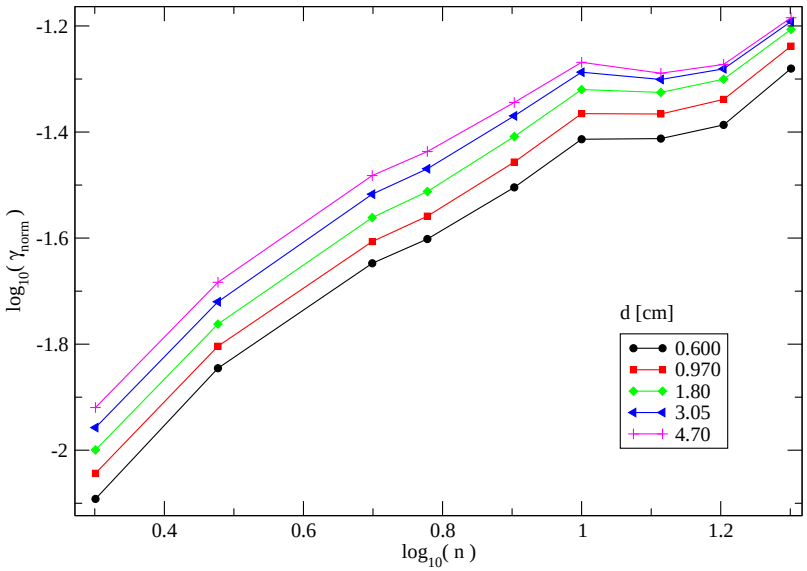

Figure 8.1.: Linear growth rate γ obtained in the simulations in terms of the toroidal mode number n for different wall distances d. For large mode numbers and large wall distances the curves approach each other. This indicates that the growth rate is less influenced by the wall distance if mode number and wall distance get larger.

in Section 4.1 by Equations (4.5) and (4.13).
According to Reference [Fitzpatrick1996], the vacuum field energy, in the case of a tokamak plasma surrounded by an ideally conducting wall, can be described by

$$\delta W_{vac} = \left[r \frac{\partial \Psi}{\partial r} \Psi \right]_{r=a} = m \Psi^2_{r=a} \frac{1 + \left(\frac{a}{r_w}\right)^{2m}}{1 - \left(\frac{a}{r_w}\right)^{2m}}, \tag{8.3}$$

where m denotes the poloidal mode number as defined in Equation (4.20), a the minor plasma radius, r_w the distance between the magnetic axis and the ideally conducting wall and $\Psi_{r=a}$ the poloidal magnetic flux at the plasma boundary. Note, that this expression applies to large aspect ratio tokamaks with circular flux surfaces and is taken as an approximation.
Now, *mode rigidity*, in the sense that the structure of the modes is not influenced by the wall distance, is assumed. From this assumption it follows, that δW_p and δK do not depend on the

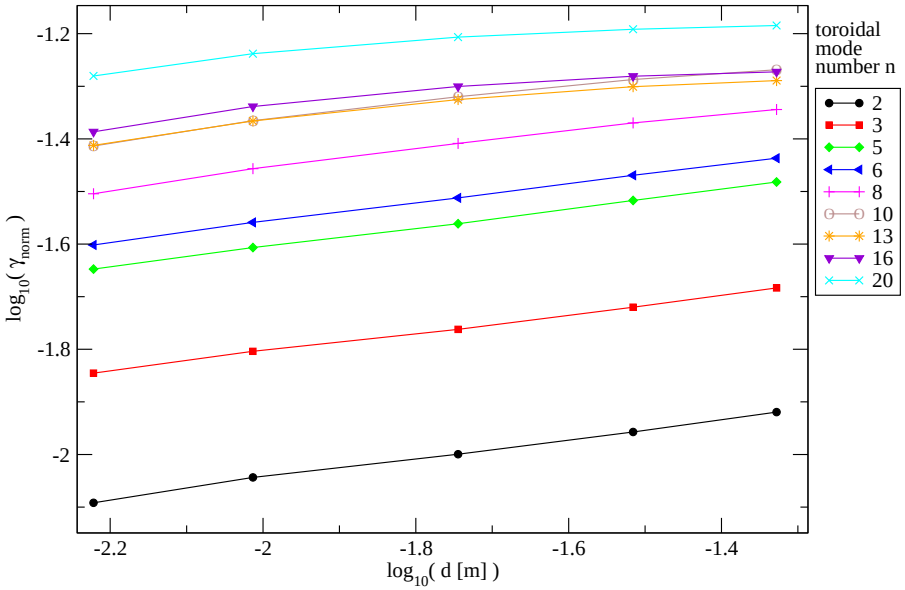

Figure 8.2.: Dependence of the growth rate γ on the wall distance d for different toroidal mode numbers n. The growth rate diminishes with decreasing wall distance, this reflects that an ideal wall which is close to the plasma has a stabilizing effect onto the mode.

wall distance, hence,

$$\frac{\partial \delta W}{\partial r_w} = 0\,, \tag{8.4}$$

$$\frac{\partial \delta K}{\partial r_w} = 0\,, \tag{8.5}$$

at constant Ψ_a. By means of the energy balance

$$\delta W_p = \gamma^2 \delta K + m\Psi_a^2 \frac{1+\left(\frac{a}{r_w}\right)^{2m}}{1-\left(\frac{a}{r_w}\right)^{2m}}\,, \tag{8.6}$$

together with the assumption of mode rigidity, it is possible to explain how the distance between the plasma and the ideally conducting wall influences the linear growth rates. Decreasing the wall distance compresses the vacuum field such that the vacuum field energy increases. As δW_p is assumed to be independent of the wall distance, this increase of the vacuum field energy yields a decrease of the kinetic energy. This leads to a reduction of the growth rate, as also δK is r_w-independent.

To obtain an expression for the linear growth rate in terms of the wall distance, first δW_p is rewritten by taking the limit $r_w \to \infty$ of Equation (8.6) which yields

$$\delta W_p \left(r_w \to \infty\right) = \gamma_\infty^2 \delta K + m\Psi_a^2, \tag{8.7}$$

where $\gamma_\infty \equiv \gamma(r_w \to \infty)$. Inserting this expression for δW_p into Equation (8.6) yields

$$\gamma^2 = \gamma_\infty^2 + \frac{m\Psi_a^2}{\delta K}\left(1 - \frac{1+\left(\frac{a}{r_w}\right)^{2m}}{1-\left(\frac{a}{r_w}\right)^{2m}}\right). \tag{8.8}$$

Now, it is useful to express Equation (8.8) in terms of a new parameter Δ, which is defined as the ratio between the wall distance d and the poloidal mode width b,

$$\Delta \equiv \frac{d}{b} = \frac{md}{\pi a}, \tag{8.9}$$

where

$$d = r_w - a. \tag{8.10}$$

The introduction of this parameter is motivated by the observation that not only with increasing wall distance, but also with increasing mode number[2], the influence of the wall distance onto the linear growth rate diminishes (see Fig. 8.1). This agrees with the expectations, as instabilities with low mode numbers are easier to stabilize by mirror currents in the ideal wall because of their larger radial extent, as mentioned in Section 4.2.
Expression (8.8) in terms of Δ yields

$$\gamma^2(\Delta) = \gamma_\infty^2 - \frac{2m\Psi_a^2}{\delta K}\left(\frac{1}{\left(1+\frac{\pi\Delta}{m}\right)^{2m}-1}\right). \tag{8.11}$$

Figures 8.3 and 8.4 show the behavior of the growth rate in the simulations as a function of Δ. It can be seen, that the influence of the wall onto the growth rate has the expected Δ-dependency. Figure 8.5 further illustrates this effect, showing that the logarithmic derivative of the growth rate with respect to Δ decreases when Δ increases.

For large mode numbers this behavior can be reproduced by a model based on the energy balance (8.1) and the assumption of mode rigidity. Taking the logarithmic derivative of Equation (8.11) with respect to Δ yields

$$\frac{d\log\gamma}{d\log\Delta} = \frac{1}{2}\frac{\Delta}{\gamma^2}\frac{d\gamma^2}{d\Delta} = \frac{\pi\Delta\left(1+\frac{\pi\Delta}{m}\right)^{2m-1}}{\frac{\gamma_\infty^2\delta K}{\Psi_a^2}\frac{1}{2m}\left[\left(1+\frac{\pi\Delta}{m}\right)^{2m}-1\right]^2 - \left[\left(1+\frac{\pi\Delta}{m}\right)^{2m}-1\right]}. \tag{8.12}$$

[2]Note, that the numerical results depend on the toroidal mode number n, whereas the theoretical model is expressed in terms of the poloidal mode number m, but as $n = qm$, where q is the safety factor introduced in Section 3.2, they are proportional to each other at each given plasma location (constant q).

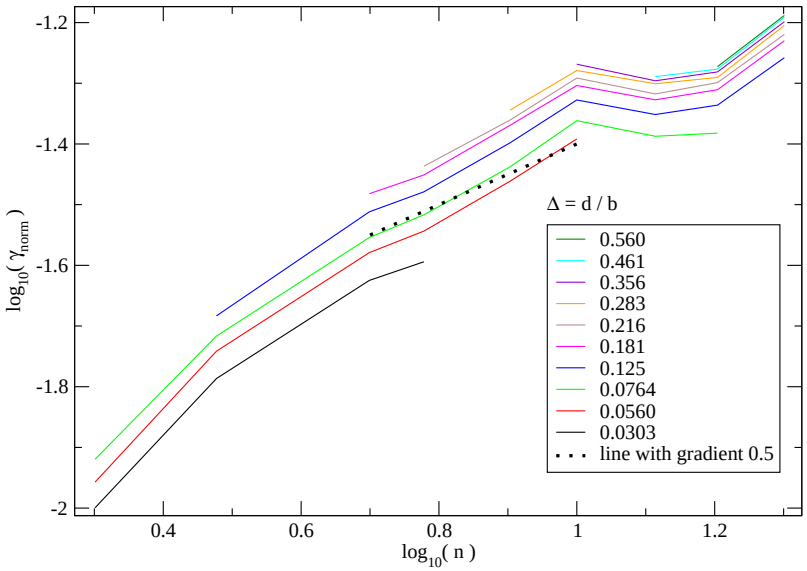

Figure 8.3.: The dependence of the growth rate γ on the toroidal mode number n is shown for different Δ, where Δ is the ratio of the wall distance d and the poloidal mode width b. The growth rate is less influenced by the wall distance for increasing Δ. The comparison of the curves with the dotted line shows that in a certain range of n the curves have a gradient of about 0.5, which means that in this range $\gamma \propto \sqrt{n}$.

This expression can now be fit to the numerical results shown in Figure 8.5, using

$$\frac{\gamma_\infty^2 \delta K}{\Psi_a^2} \tag{8.13}$$

as free parameter. Note, that it is exactly the r_w-independence of this parameter which reflects the assumption of mode rigidity. As Ψ_a^2 acts as a normalization, it corresponds to the normalized kinetic energy at infinite wall distance.
To fit Equation 8.12 to the curves in Figure 8.5, it would be favorable to use a fit parameter which is independent of m. Therefore, the numerical results are used to obtain information about how $\gamma_\infty^2 \delta K / \Psi_a^2$ depends on m. Figure 8.6 shows the logarithmic derivative of the growth rate with respect to the mode number in the simulations. It can be seen, that for large enough mode numbers, this derivative is approximately 0.5. (The deviation of the values in the simulations with the three highest mode numbers is probably due to resolution limitations.) This yields

$$\frac{d\log\gamma}{d\log n} \approx \frac{1}{2} \Rightarrow \gamma \propto \sqrt{n} \propto \sqrt{m} \qquad \text{(for large } m \text{ and fixed } q\text{)}. \tag{8.14}$$

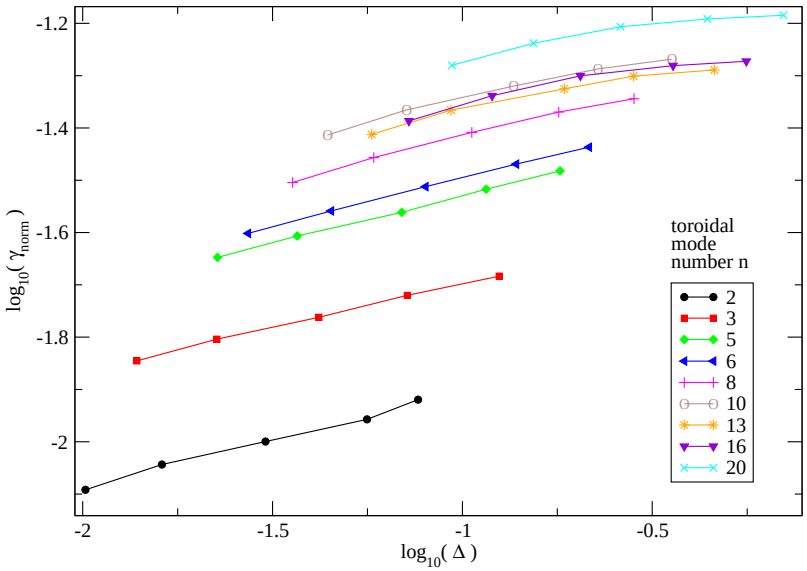

Figure 8.4.: The growth rate γ in terms of Δ is shown for different toroidal mode numbers n. Δ is defined as the ratio between the wall distance d and the mode width b. Especially for high Δ the curves have very similar gradients.

Using this result, it follows from Equation 8.11, that

$$\gamma_\infty^2 \propto m \qquad \text{(for large m)}\,, \tag{8.15}$$

and

$$\frac{\partial}{\partial m}\left(\frac{\Psi_a^2}{\delta K}\left[\frac{-2}{\left(\frac{\pi\Delta}{m}+1\right)^{2m}-1}\right]\right)=0 \qquad \text{(for large } m)\,. \tag{8.16}$$

In the limit $m \to \infty$ the term in squared brackets becomes

$$\lim_{m\to\infty}\frac{-2}{\left(\frac{\pi\Delta}{m}+1\right)^{2m}-1}=\frac{-2}{\exp\left(2\pi\Delta\right)-1}\,, \tag{8.17}$$

which is independent of m for fixed values of Δ, which means at a fixed ratio between wall distance and mode width. Equations (8.16) and (8.17) imply that

$$\frac{\partial}{\partial m}\left(\frac{\Psi_a^2}{\delta K}\right)=0 \qquad \text{(for large } m \text{ and fixed } \Delta)\,. \tag{8.18}$$

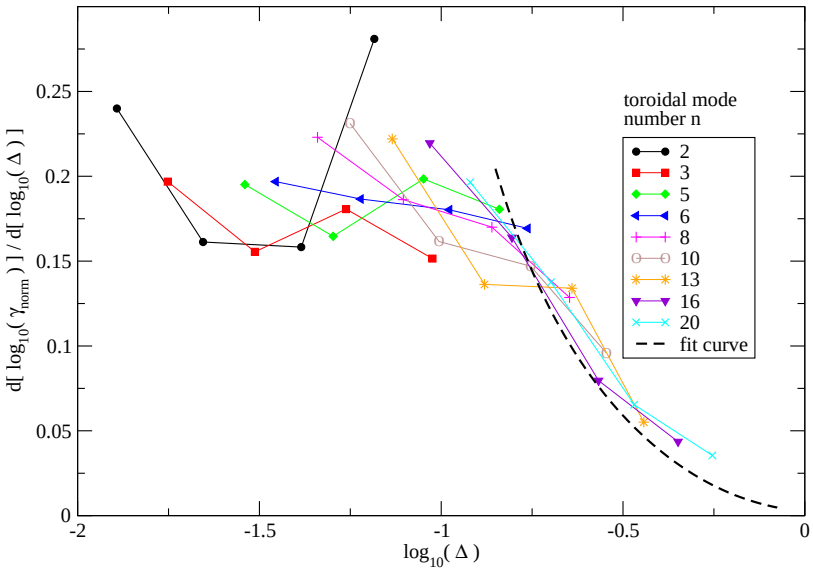

Figure 8.5.: The logarithmic derivative of the growth rate γ with respect to Δ is shown for different toroidal mode numbers n.The dependence of the growth rate on Δ diminishes with increasing Δ. This reflects the decreasing influence of the wall onto the growth rate for large wall distances. Furthermore it can be observed that the curves for different n approach each other for increasing Δ. The dashed line shows a fit to the results of the simulation which is based on a simple theoretical model with only one free parameter (Eq.(8.12)).

Finally, it is obtained that

$$\frac{\gamma_\infty^2 \delta K}{\Psi_a^2} \propto m \qquad \text{(for large } m\text{)}\,, \tag{8.19}$$

such that it is possible to define an m-independent fit parameter as

$$\frac{\hat{\gamma}_\infty^2 \delta K}{\Psi_a^2} \equiv \frac{\frac{\gamma_\infty^2}{m} \delta K}{\Psi_a^2}\,. \tag{8.20}$$

The resulting fit is shown in Figure 8.5. It can be seen, that the dependence of the linear growth rate on the distance between plasma and ideal wall observed in the simulations with JOREK, can be reproduced well for large mode numbers by the simple model based on the energy balance (8.1) and the assumption of mode rigidity. Note, that to obtain the fit shown in Figure (8.5), Equation 8.12 for $m = 100$ has been fit to all data points in the region where the fit is drawn,

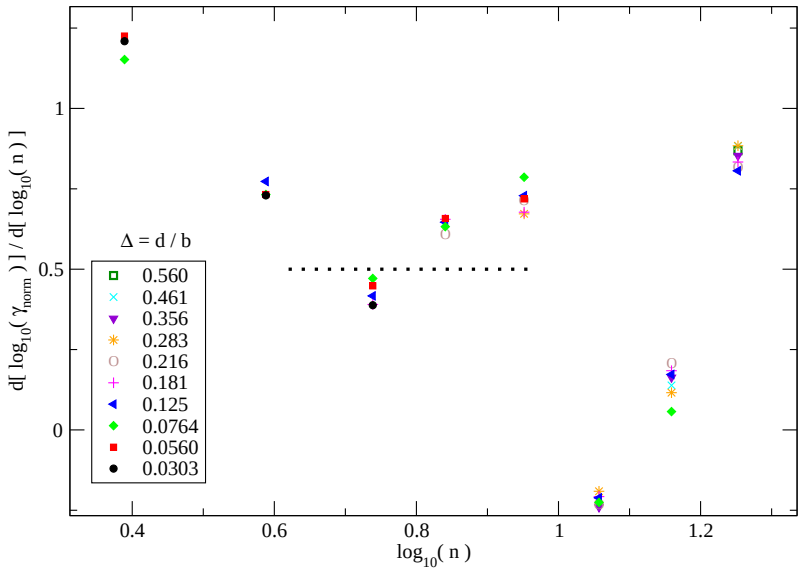

Figure 8.6.: The logarithmic derivative of the growth rate γ with respect to the toroidal mode number n is shown for different values of Δ. For large toroidal mode numbers the values of the derivatives are approximately 0.5 (compare to dotted line), which means that $\gamma \propto \sqrt{n}$. The deviation from this value for the three largest mode numbers is probably due to an insufficient resolution.

independent of the corresponding mode number. This is justified by the observation, that the values of the logarithmic derivative of the growth rate with respect to Δ in the simulations seem to be independent of the mode number in this region.
Figure 8.7 shows the fit curves using the same value for the fit parameter as in Figure 8.5, but different values of m. As expected, because the fit parameter is only m-independent for large m, the curves for small mode numbers show a larger deviation from the numerical results and the fit curves for large mode numbers approach each other.

One may ask why d has been defined as the distance between the wall and the separatrix instead of the distance between the wall and the maximum of the mode. This definition has been chosen, because, as can be seen in Figure 8.8, the perturbed flux Ψ_1 (the plot shows its $n = 13$ component) is not symmetric in reference to the its maximum ($\Psi_N = 0.988$), but it decreases much slower towards the separatrix ($\Psi_N = 1$) than towards the center of the plasma.
The assumption that the distance between the wall and the separatrix determines the physics rather than the distance between the wall and the maximum of the perturbation is supported by the fact that if d is replaced by the distance between the wall and the mode maximum, the curves

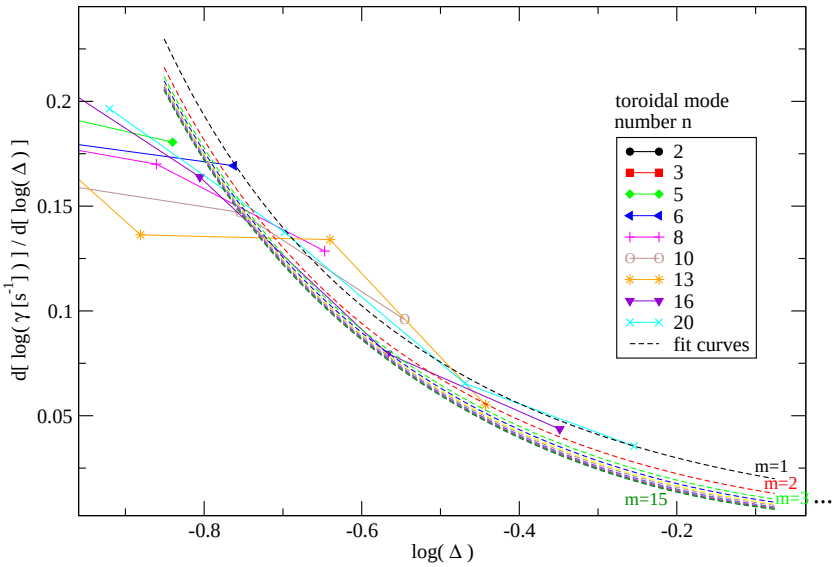

Figure 8.7.: Fit curves (dashed lines) with the same value for the fit parameter, but varying values of m. As the fit parameter is independent of the mode number for large mode numbers, the curves approach each other for increasing m.

in Figure 8.5 do not show a behavior which is as universal as the one shown choosing the initial definition.

Summary

The dependence of the linear growth rate on the mode number and on the distance between plasma and ideally conducting wall has been analyzed in simulations of edge-localized modes in ASDEX Upgrade geometry including one non-zero toroidal mode only. It has been found that the behavior of the linear growth rate corresponds to the expectations from experimental findings and compared to a simple theoretical model. The growth rate in general increases with increasing mode number, which is expected taking into account the neglect of diamagnetic stabilization in the simulations. For large mode numbers, the numerical results suggest that γ^2 is proportional to the mode number.
Furthermore, it can be observed that the larger the wall distance, the higher is the growth rate, which reflects the stabilizing effect of an ideal wall close to the plasma. This influence of the wall onto the mode growth decreases with increasing values of Δ, which is defined as the ratio

between wall distance and poloidal mode width[3]. This decrease becomes significant at $\Delta \gtrapprox 1/6$ (see Figure 8.5). At $\Delta \approx 2/5$, the logarithmic derivative of the linear growth rate with respect to Δ has dropped by about 75 %. This means, that in the presented simulations with the largest possible wall distance, the influence of the ideal wall onto the growth rates for high mode numbers can be neglected. This is particularly important, as high mode numbers are most unstable and present the dominant participants in the non-linear evolution.
The dependence of the linear growth rate on the wall distance, observed in the simulations, can be reproduced by means of a simple theoretical model. The model is based on the idea, that assuming mode rigidity, a decrease of the wall distance leading to an increase of vacuum magnetic field energy in the region between plasma and wall causes that a smaller part of the energy released by the instability is transformed into kinetic energy deforming the plasma, such that the growth rate diminishes.

[3]Note, that the mode width has been defined as half the wavelength of the perturbation in poloidal direction (see Figure 7.3).

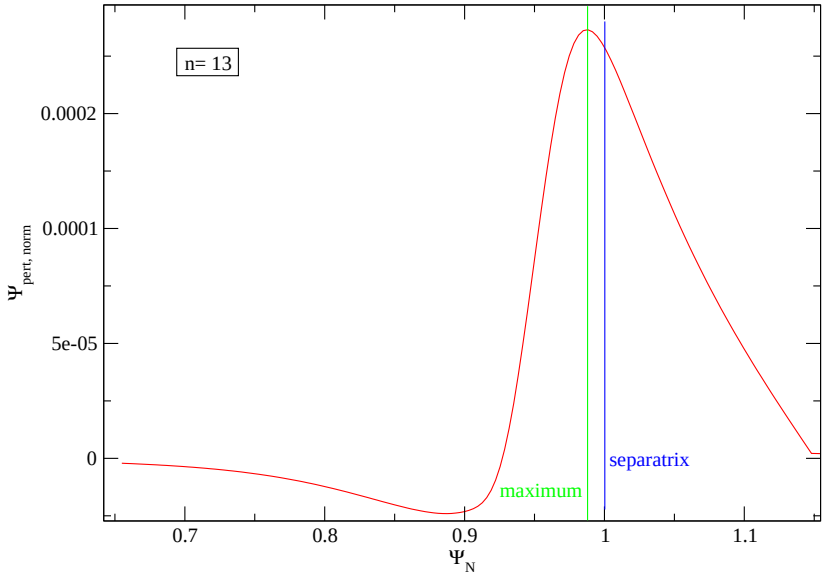

Figure 8.8.: The figure shows the $n = 13$ component of the poloidal flux perturbation Ψ_{pert} at the edge of the plasma in terms of the normalized poloidal flux Ψ_N. The mode expands more towards the separatrix than towards the inside of the plasma.

Chapter 9.

Mode interaction

Figures 7 and 9.1 show the time evolution of the mode structure in ELM simulations where four and eight different toroidal modes have been included, respectively. In Figures 9.2 and 9.3, the mode structure is shown for simulations with the same number of included modes, but a smaller distance between separatrix and ideally conducting wall. It can be seen, that the main characteristics of the nonlinear evolution of the modes are similar in simulations with the same number of included toroidal modes and different wall distances. Comparing the results of these simulations, it has to be taken into account, that the linear growth rates are influenced (differently, depending on the mode number) by the wall distance as discussed in Chapter 8. This has an impact on the nonlinear evolution and is a probable explanation for the residual small differences between the results.

The main characteristics of the evolution of the mode structure can be explained by means of a simple mode interaction picture. In this model, nonlinear mode coupling allows the transfer of energy between different modes. Consider a wave consisting of two contributions with different mode numbers n_1 and n_2 and amplitudes A_1 and A_2, respectively,

$$A(\phi) = A_1 \cos(n_1\phi) + A_2 \cos(n_2\phi), \tag{9.1}$$

where $A(\phi)$ is defined in terms of the energy density $e(\phi)$ by

$$A(\phi) \equiv \sqrt{e(\phi)}. \tag{9.2}$$

Terms which are nonlinear in $A(\phi)$ lead to a mixture of the two modes. For example, a quadratic term yields

$$\begin{aligned} A^2(\phi) &= [A_1 \cos(n_1\phi) + A_2 \cos(n_2\phi)]^2 \\ &= A_1^2 \cos^2(n_1\phi) + A_2^2 \cos^2(n_2\phi) + A_1 A_2 \left(\cos([n_1 - n_2]\phi) + \cos([n_1 + n_2]\phi)\right). \end{aligned} \tag{9.3}$$

Hence, two modes with mode numbers $(n_1 - n_2)$ and $(n_1 + n_2)$ are generated. According to this, energy transfer can take place between three modes, if one of the mode numbers can be expressed as the sum or the difference of the two others.

Considering four modes $n = 4, 8, 12, 16$ and neglecting higher than second order terms, this yields the following system of coupled differential equations describing the time evolution of

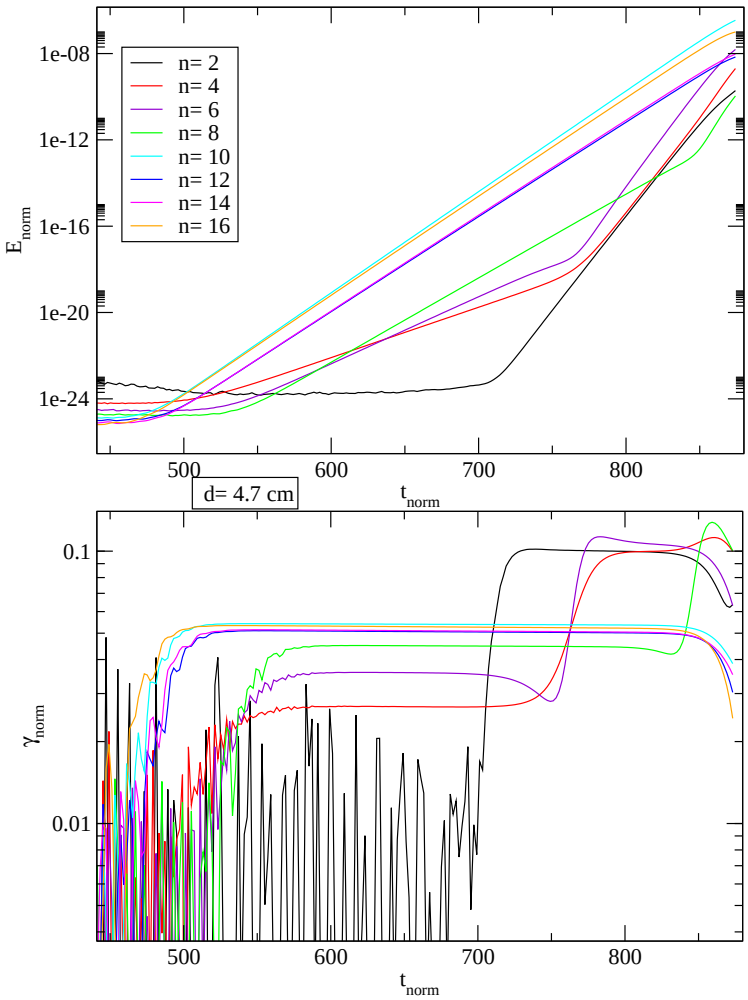

Figure 9.1.: Time trace of energy and growth rate of the toroidal modes $n = 2,4,6,8,10,12,14,16$ in a simulation with wall distance $d = 4.7\,\mathrm{cm}$.

their amplitudes

$$\begin{aligned}
\frac{\partial A_4}{\partial t} &= \gamma_4 A_4 + \gamma_{(8,-4)} A_4 A_8 + \gamma_{(12,-8)} A_8 A_{12} + \gamma_{(16,-12)} A_{12} A_{16} \\
\frac{\partial A_8}{\partial t} &= \gamma_8 A_8 + \gamma_{(4,4)} A_4 A_4 + \gamma_{(12,-4)} A_4 A_{12} + \gamma_{(16,-8)} A_8 A_{16} \\
\frac{\partial A_{12}}{\partial t} &= \gamma_{12} A_{12} + \gamma_{(4,8)} A_4 A_8 + \gamma_{(16,-4)} A_4 A_{16} \\
\frac{\partial A_{16}}{\partial t} &= \gamma_{16} A_{16} + \gamma_{(8,8)} A_8 A_8 + \gamma_{(4,12)} A_4 A_{12}\,,
\end{aligned} \tag{9.4}$$

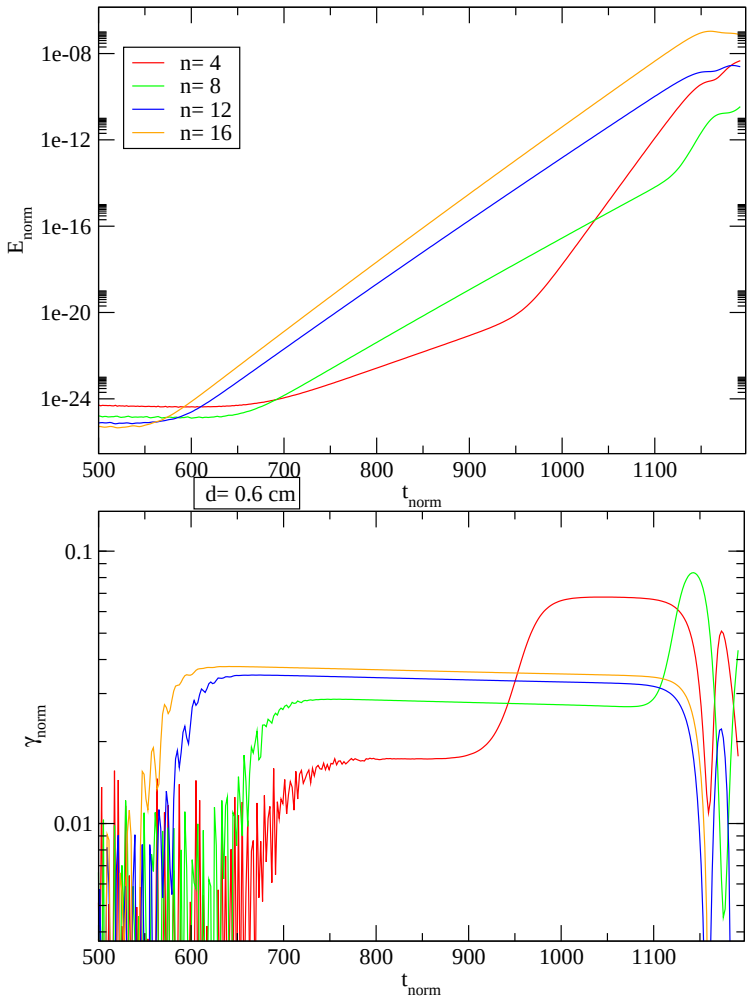

Figure 9.2.: Time trace of energy and growth rate of the different toroidal modes. The distance between separatrix and ideally conducting wall in this simulation is 0.6 cm.

where A_i denotes the amplitude of the i^{th} mode, γ_i denotes its linear growth rate and $\gamma_{(j,k)}$ the coupling constant to the j^{th} and the k^{th} mode. In this model, the coupling constants are not time-dependent. This simplification means that mode coupling cannot be influenced by temporal changes of the mode structure. This is justified if mode rigidity, in the sense that the structure of the modes do not change significantly in time, is assumed.
The linear terms in (9.4) describe the energy transfer from the $n = 0$ mode to the $n \neq 0$ compo-

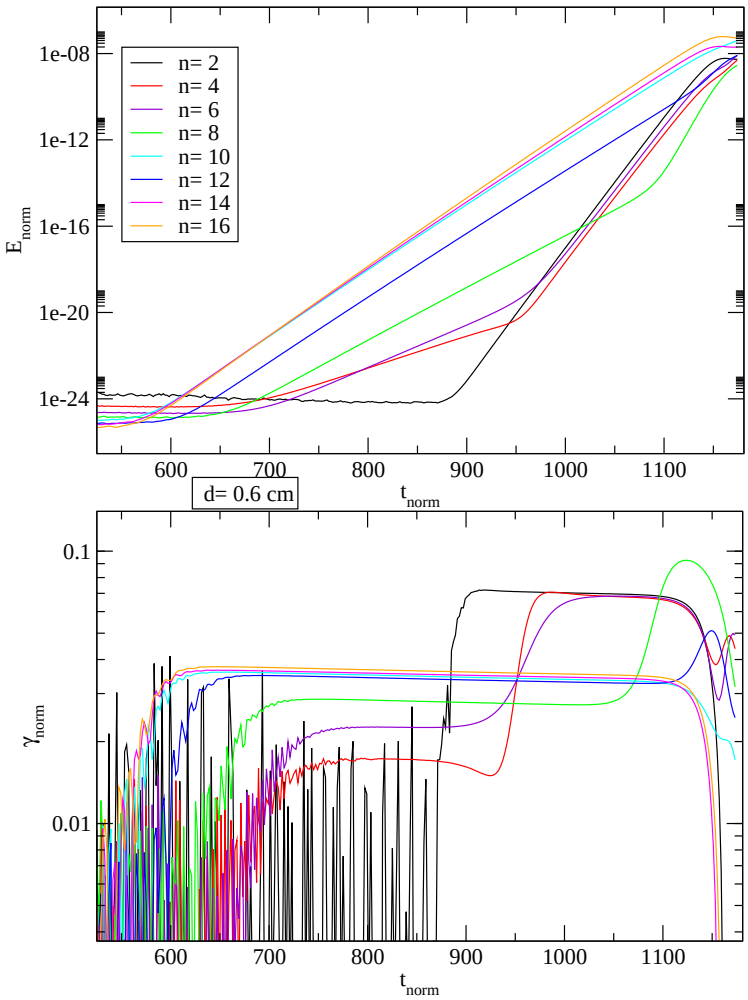

Figure 9.3.: Time trace of energy and growth rate of the different toroidal modes. The wall distance in this simulation is 0.6 cm.

nents. The growth rate γ_n could also be expressed in terms of coupling constants as

$$\gamma_n \equiv \gamma_{(n,0)} A_0 + \gamma_{(n,-0)} A_0 \,, \tag{9.5}$$

but as the energy of the $n = 0$ component is typically several orders of magnitude higher than the other components, changes in its energy due to coupling to other modes are negligible, such that A_0 can be assumed constant. Thus, the linear terms result in an influx of energy into the system, whereas the nonlinear terms only yield an exchange of energy between the different $n \neq 0$ modes, but leave the total energy of the system invariant. This energy conservation of the

nonlinear terms leads to constraints for the coupling constants. The energy of the n^{th} mode is given by

$$E_n = \int_V e_n(\phi)\,\mathrm{d}V = \int_V (A_n \cos(n\phi))^2\,\mathrm{d}V \propto A_n^2, \tag{9.6}$$

and the total energy of the modes $n = 4, 8, 12, 16$ is given by

$$\begin{aligned} E_{\text{tot}} &= \int_V \left(\sum_n A_n \cos(n\phi)\right)^2 \mathrm{d}V \\ &\propto \int_0^{2\pi} \left(\sum_n A_n \cos(n\phi)\right)^2 \mathrm{d}\phi \\ &= \int_0^{2\pi} \sum_n A_n^2 \cos^2(n\phi)\,\mathrm{d}\phi + \underbrace{\int_0^{2\pi} 2 \sum_{l\neq k} A_l \cos(l\phi) A_k \cos(k\phi)\,\mathrm{d}\phi}_{\equiv 0} \\ &\propto \sum_n A_n^2. \end{aligned} \tag{9.7}$$

Thus, to conserve energy, the time evolution (9.4) has to satisfy

$$\frac{\partial E_{\text{tot}}}{\partial t} \propto \sum_n A_n \frac{\partial A_n}{\partial t} \stackrel{!}{=} 0. \tag{9.8}$$

Note, that considering energy conservation, the linear terms have to be omitted, as the $n = 0$ mode acts as an energy reservoir. This leads to the following relations between the coupling constants as energy conservation needs to hold independently of the mode amplitudes A_i:

$$\begin{aligned} \gamma_{(4,8)} + \gamma_{(12,-4)} + \gamma_{(12,-8)} &= 0 \\ \gamma_{(4,12)} + \gamma_{(16,-4)} + \gamma_{(16,-12)} &= 0 \\ \gamma_{(4,4)} + \gamma_{(8,-4)} &= 0 \\ \gamma_{(8,8)} + \gamma_{(16,-8)} &= 0. \end{aligned} \tag{9.9}$$

The time evolution of the mode structure determined by this model, which is given by the system of coupled differential equations (9.4) and the constraints for the coupling constants (9.9), can now be used to reproduce, to a certain extent, the results of the JOREK simulations shown for example in Figure 7. Figure 9.4 compares the results of the model to the results of a JOREK simulation with $n = 4, 8, 12, 16$ and $d = 4.7\,\text{cm}$, showing the time evolution of energies and growth rates. As can be seen in Figure 9.5, it is also possible to reproduce the results of a JOREK simulation with the same included toroidal modes, but a different wall distance $d = 0.6\,\text{cm}$ with this model by adjusting the linear growth rates, but using the same coupling constants as in the case with the larger wall distance. This independence of the coupling constants from the wall distance may be understood as an indication of mode rigidity, in the sense that the structure of the modes is independent of the wall distance.

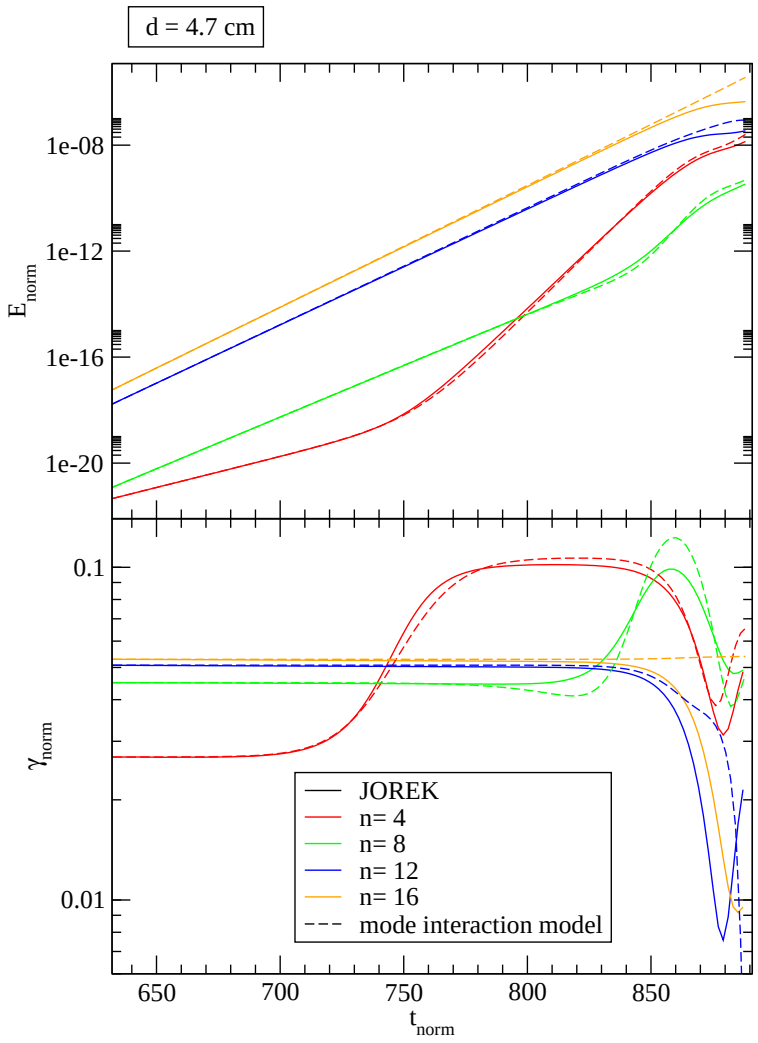

Figure 9.4.: Time traces of the energies and growth rates of the toroidal modes resulting from a JOREK simulation with $n = 4, 8, 12, 16$ and $d = 4.7\,\mathrm{cm}$ (continuous lines), compared to the results of a fit based on the simple mode interaction model (dashed lines). Whereas the early nonlinear phase can be reproduced very well by the model, other effects not included in the model seem to become important in the phase of saturation.

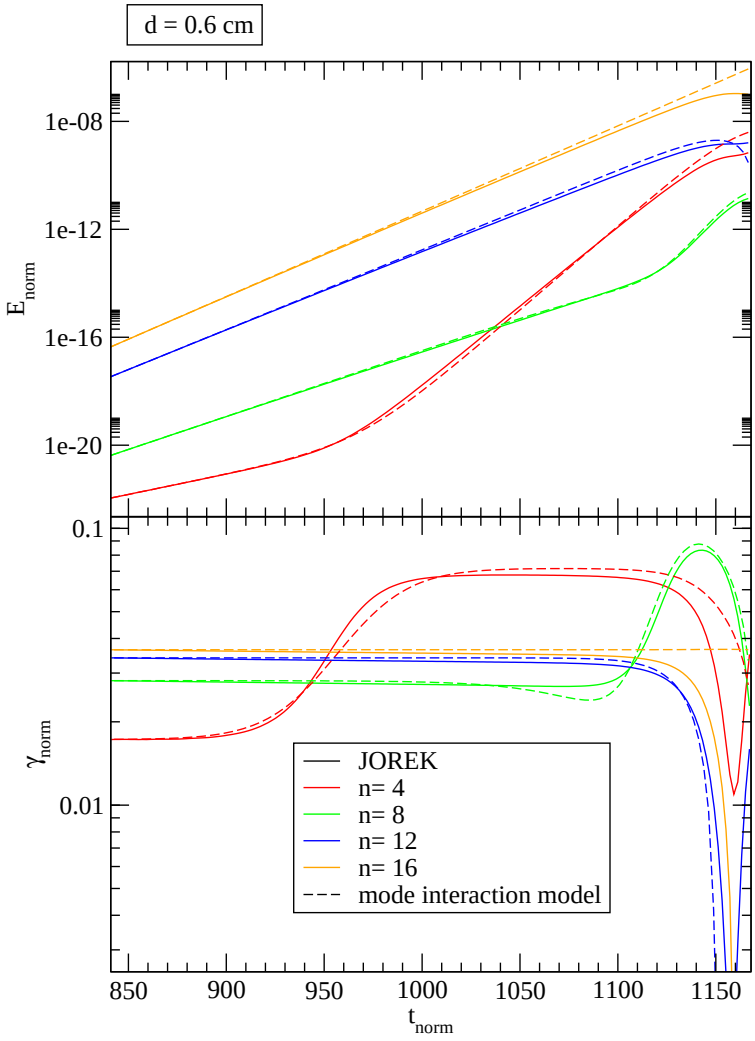

Figure 9.5.: Time traces of the energies and growth rates of the toroidal modes resulting from a JOREK simulation with $n = 4, 8, 12, 16$ and $d = 0.6\,\mathrm{cm}$ (continuous lines), compared to the results of a fit based on the simple mode interaction model (dashed lines). For the fit, the same coupling constants have been used as in the case with $d = 4.7\,\mathrm{cm}$ (Figure 9.4).

The results shown in Figures 9.4 and 9.5 have been obtained by fitting the time evolution of the energies contained in the different modes of the model system to the corresponding time evolution in the JOREK simulation. Afetr using the constraints of energy conservation, the model has ten independent parameters, thereof six coupling constants and four linear growth rates. The latter are directly taken from the linear phase of the JOREK simulations such that six free parameters remain.
The fit procedure has been carried out for the simulations with $d = 4.7\,\mathrm{cm}$ and $d = 0.6\,\mathrm{cm}$ simultaneously to show that it is possible to find a set of coupling constants which can reproduce both simulations well. To obtain the fit, the squared differences between the time traces of the logarithmic energy obtained from the mode interaction model and from the JOREK simulations at discrete points in time are calculated. The sum of these values over all modes $n = 4, 8, 12, 16$ and both simulations is minimized by adjusting the six free coupling constants. Note, that in each step of this minimization process, the system of coupled differential equations (9.4) has to be solved for both cases using the current set of coupling constants. The coupling constants, used to obtain the results shown in Figures 9.4 and 9.5, are $\gamma_{(12,-4)} = 44.24$, $\gamma_{(12,-8)} = -4516$, $\gamma_{(4,12)} = 41.84$, $\gamma_{(16,-4)} = -106.3$, $\gamma_{(4,4)} = 165.4$ and $\gamma_{(8,8)} = 149.6$, whereof $\gamma_{(12,-4)}$, $\gamma_{(4,4)}$ and $\gamma_{(16,-12)} = -\gamma_{(4,12)} - \gamma_{(16,-4)}$ play the major role in determining the characteristic rise of the subdominant modes.
The obtained coupling constants can be used to gain information about the relative importance of the coupling terms. Comparing the time evolution of the different nonlinear terms in (9.4) yields that, for example, the rise of the growth rate of the $n = 8$ component is in both simulations mainly due to the coupling to the $n = 4$, as the $(\gamma_{(4,4)} A_4 A_4)$ term is dominant one at the moment of the rise.
Taking a detailed look at the time traces of energies and growth rates of the JOREK simulations and the corresponding fit, it can be observed that especially in the early nonlinear phase the results of the mode interaction model are in very good agreement with the JOREK results in both simulations. In the phase of saturation, the simple model starts to deviate from the time traces in the JOREK simulations. Especially the saturation of the most dominant mode ($n = 16$) is not described at all by the mode interaction model.
These deviations correspond to the expectations, as the physical mechanisms responsible for the saturation are not described by the simple mode interaction picture. The decline of the growth rates calculated by the simple model for some modes is caused by energy transfer to other nonzero modes and not by a mode saturation effect. Real saturation is caused, for example, by the reduction of the drive of the instability due to a change in the background edge profiles and an additional stabilizing effect of the ideally conducting wall if the displacement ξ becomes significant compared to the wall distance. In addition, both mechanisms can influence the spatial structure of the different toroidal modes, such that mode rigidity cannot be assumed anymore. These effects, which influence the evolution of the mode structure in the phase of saturation, are discussed in more detail in the following Chapter.

Summary

It has been shown, that the main characteristics of the evolution of the toroidal mode structure before the phase of saturation of the mode growth in ELM simulations can be reproduced by a simple mode interaction model. This model describes the time evolution of the amplitudes of a set of toroidal modes by a system of coupled differential equations including linear terms proportional to the linear growth rates, describing the energy transfer from the $n = 0$ mode to the non-zero modes and nonlinear terms of second order, describing the energy transfer between the non-zero modes via mode coupling. The coupling constants are time-independent, assuming mode rigidity, in the sense that the shape of the toroidal modes does not change significantly in time. Specific relations between the coupling constants ensure that the nonlinear terms conserve energy.

The evolution of the mode structure in two simulations with different distances between plasma and ideal wall have been reproduced adjusting the linear growth rates, but using the same set of coupling constants. This universality of the coupling constants confirms, that mode rigidity, in the sense that the structure of the mode is independent of the wall distance, can be assumed. Moreover, the fact, that the results of two simulations with different wall distances can be reproduced to a large extent by the same model only by changing the linear growth rates, supports the idea, that the wall distance mainly influences the non-linear mode evolution by affecting the linear growth rates.

In the phase of saturation, mode rigidity is not valid anymore and additional saturation effects not included in the presented model become important for the mode structure. As expected, the results of the model deviate from the results of the JOREK simulations in this phase.

Chapter 10.

Saturation

As discussed in Chapter 9, the main characteristics of the early nonlinear evolution of the mode structure in ELM simulations with several included toroidal modes are determined by mode interaction effects. In the subsequent phase, where the mode growth starts to saturate, additional effects have to be taken into account to explain the development of the mode structure. In this Chapter, two saturation mechanisms are discussed. To be able to separate mode interaction effects from saturation effects, also simulations with only one included non-zero toroidal mode are analyzed.

One reason for the saturation of the mode growth is the reduction of the $(m,n) = (0,0)$ current density and the $(m,n) = (0,0)$ pressure gradient, which diminishes the drive of the instability and thus yields a reduction of the growth rate. A second effect is related to the stabilizing effect of the ideally conducting wall. If the displacement ξ in radial direction becomes significant compared to the distance between plasma and ideal wall, the ideal wall can additionally stabilize the mode.

Figure 10.1 shows how the growth rates of different toroidal modes in the phase of saturation decrease in terms of the energy of the corresponding mode. The growth rates have been obtained from simulations with only one included toroidal mode and two different wall distances. It can be observed, that for all mode numbers, a smaller wall distance results in a shift of the saturation to lower energy values.

This is consistent with the idea that the effect of the ideal wall becomes important with increasing significance of the displacement compared to the wall distance, which is further illustrated in Figure 10.2. It shows the growth rate of the $n = 5$ mode, normalized by the corresponding linear growth rate, in terms of the displacement of the density ξ_ρ, for two simulations with one included toroidal mode and two different wall distances. In the simulation with the smaller wall distance, the saturation takes place already at smaller displacement values, which means that the displacement does not have to be as large as in the case with a larger wall distance for the stabilizing effect of the ideal wall to play a significant role in the saturation.

Coming back to Figure 10.1, it further shows that modes with higher toroidal mode numbers saturate at smaller energies than modes with small mode numbers. The question, if this n-dependence is related to the reduction of the drive due to a change in the $(m,n) = (0,0)$ edge profiles, is addressed in the following. If the background edge profiles were changed more by modes with large mode numbers than by modes with small mode numbers, the n-dependence of the saturation could be explained by this effect.

The change of edge pressure gradient and edge current density profiles between linear and saturation phase for different mode numbers is shown in Figure 10.3. It can be seen that, indeed, at

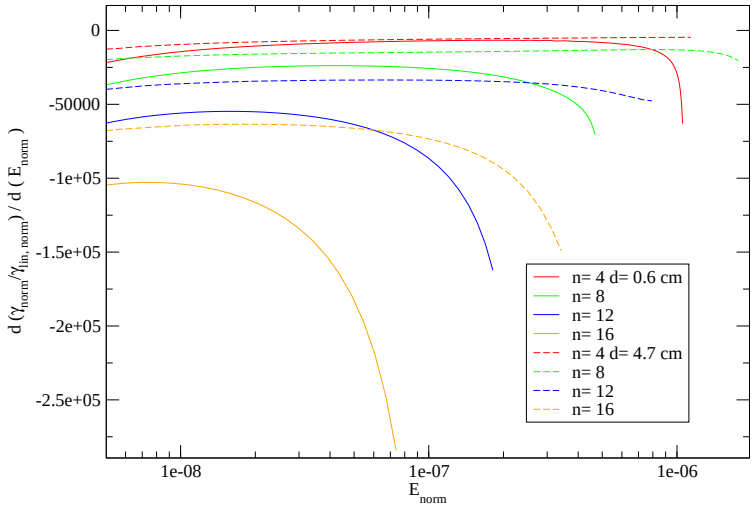

Figure 10.1.: Derivative of the growth rate γ of various toroidal modes with respect to the energy contained in these modes in the phase of saturation. Growth rates are normalized by the corresponding growth rates in the linear phase. The curves show the results of simulations with one included toroidal mode and at two different distances between plasma and wall. The energy is the sum of magnetic and kinetic energies of the modes. It can be seen, that saturation sets in at lower energies if the wall distance is small compared to simulations with larger wall distances. The same effect is observed for simulations with larger mode numbers compared to simulations with smaller mode numbers.

the same energy of the mode, the modification of the profiles is stronger for larger mode numbers. Both pressure gradient and current density are reduced at the radial position of maximum perturbation amplitude, which diminishes the drive of the instability. Figure 10.4 further illustrates the time evolution of the poloidal flux perturbation of the $n = 16$ component, compared to the evolution of the background pressure gradient profile. It can be seen, that while the amplitude of the perturbation grows, the background profile is more and more modified at the edge.
The question arises, why the background profiles are modified more by perturbations with large mode numbers than by perturbations with small mode numbers, although the energy of the mode is the same. This can be understood, comparing the radial structures of the perturbations. Figure 10.5 shows the Fourier spectrum of the poloidal flux perturbation in the simulations with $n = 4$ and $n = 16$ at times, where the same energy is contained in these modes. The $n = 16$ perturbation is significantly more localized than the $n = 4$ perturbation and thus able to perturb the $(m,n) = (0,0)$ edge profiles more efficiently.

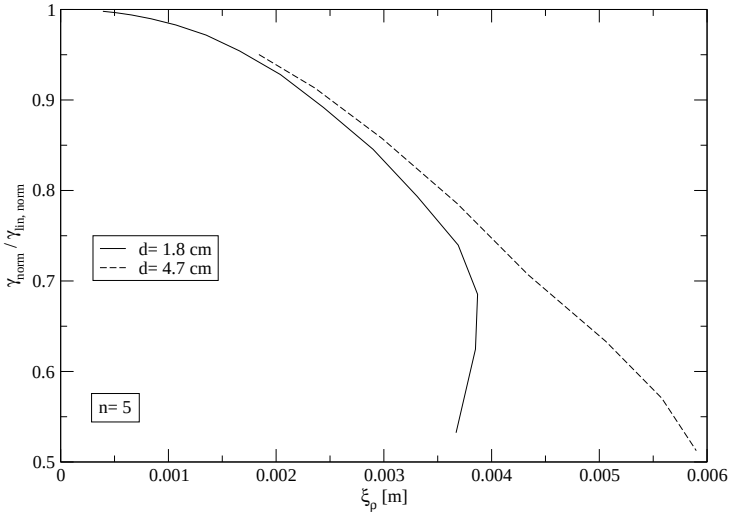

Figure 10.2.: Growth rate of the $n = 5$ mode in terms of the displacement of the density in radial direction ξ_ρ, normalized by their value in the linear phase. The growth rates are obtained from simulations with one included toroidal mode at two different wall distances. At a smaller wall distance, the saturation of the mode growth is shifted towards smaller values of ξ_ρ.

Comparing the time evolution of the perturbation structure to the evolution of the $(m,n) = (0,0)$ profiles, it is also interesting to examine how, on the other hand, the changes in the background profiles influence the structure of the perturbation.This can be seen in Figure 10.6 where the temperature perturbation in a simulation including only the toroidal mode $n = 16$ is shown at two different points in time and compared to the background pressure gradient, current density and temperature gradient profiles at these moments. In the region, where the current density is reduced and the pressure gradient is flattened, the temperature perturbation grows slower while the perturbation grows faster in the region where the background profiles are enhanced. Hence, the maximal amplitude of the perturbation is shifted inwards.
The same effect is observed for the density perturbation shown in Figure 10.7. In this case, the perturbation has developed a pronounced minimum in the center of the structure. This difference between the evolution of temperature and density perturbations can be understood considering the background temperature and density gradient profiles. As the perturbations T_{pert} and ρ_{pert} are given by

$$T_{\text{pert}} \propto \vec{\xi} \cdot \vec{\nabla} T_{(m,n)=(0,0)} \,, \tag{10.1}$$

$$\rho_{\text{pert}} \propto \vec{\xi} \cdot \vec{\nabla} \rho_{(m,n)=(0,0)} \,, \tag{10.2}$$

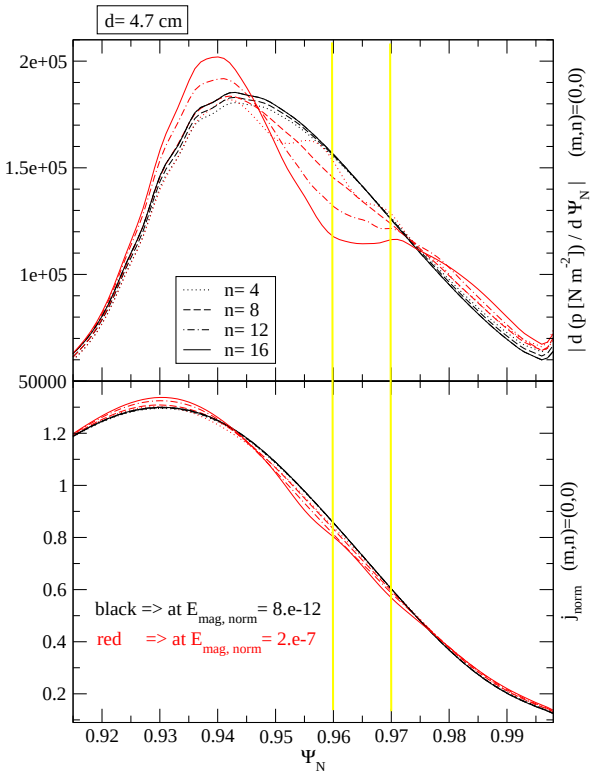

Figure 10.3.: Background pressure gradient and current density at the edge in simulations with different single toroidal modes. Curves of the same color show the profiles at a moment, where the magnetic energies of the modes have the same value. The black profiles correspond to a moment in the linear phase, the red profiles to a moment in the phase of saturation. In the region between the yellow lines, the corresponding poloidal magnetic flux perturbations are maximal. In this region, the $(m,n) = (0,0)$ pressure gradient and current density are reduced, which yields a reduction of the mode drive.

the structure of the perturbed quantities depends also on the corresponding background profile. As can be seen in Figures 10.6 and 10.7, the flattened region in the $(m,n) = (0,0)$ density gradient profile is more localized than the one in the temperature gradient profile, which explains the different evolution of the structures of the perturbations.

Having analyzed the saturation of the mode growth in simulations with only one included toroidal mode, it is now possible to compare the results to the saturation phase in simulations

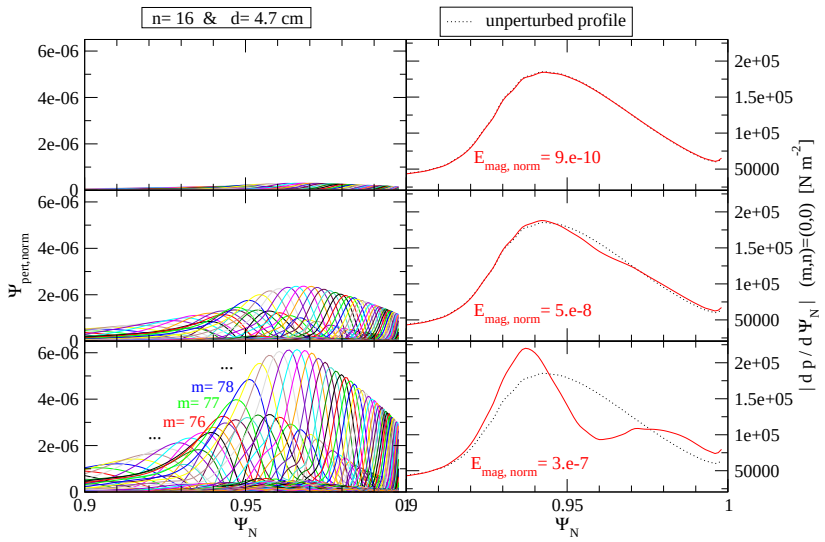

Figure 10.4.: Poloidal magnetic flux perturbation compared to the $(m,n) = (0,0)$ pressure gradient profile at the edge. The various poloidal Fourier harmonics belonging to the toroidal $n = 16$ mode are plotted. The results have been obtained in a simulation, where the only included toroidal mode is $n = 16$. The three plots show different points in time, the first in the linear phase, the second in the early phase of saturation and the third at a later moment in the phase of saturation. It can be seen, that while the amplitude of the perturbation is growing, the background pressure gradient at the edge deviates more and more from its unperturbed profile.

with several included modes. Figure 10.8 shows the growth rate of the $n = 16$ mode in the phase of saturation in simulations with different numbers of included toroidal modes and varying wall distances. It can be seen, that also in the case of several included modes, a smaller wall distance yields a saturation at smaller energies. Furthermore, it is observed, that with more toroidal modes included, saturation sets in earlier (in terms of the energy).
One possible reason for this behavior is, that the growth rate of the $n = 16$ mode in simulations with several included toroidal modes is additionally decreased due to energy transfer from the $n = 16$ to other non-zero toroidal modes. Another possible mechanism is, that in simulations with more toroidal modes, the $(m,n) = (0,0)$ current density and pressure gradient edge profiles are perturbed by all included modes leading to a stronger modification. Figure 10.9 confirms this idea. It compares the background current density and pressure gradient profiles in a simulation where the $n = 16$ is the only included toroidal mode to a simulation with eight included toroidal modes, where the $n = 16$ is the most dominant mode. It is observed, that at a moment in the phase of saturation, where the same energy is contained in the $n = 16$ mode in both simulations,

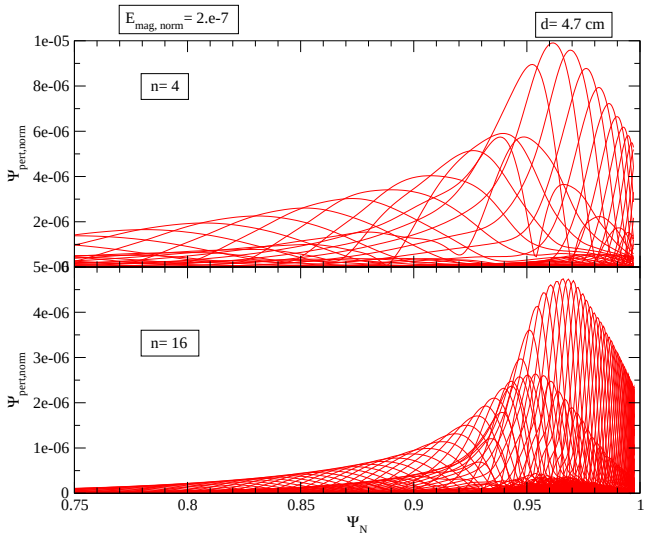

Figure 10.5.: Poloidal magnetic flux perturbation at the edge in simulations with the single toroidal mode $n = 4$ and $n = 16$, respectively. The plots show points in time, where the modes have the same magnetic energies. The $n = 16$ perturbation is significantly more localized than the $n = 4$ perturbation. This explains why the former is able to change the $(m,n) = (0,0)$ current density and pressure gradient profiles more than the latter, although the modes have the same energy.

the background profiles are significantly more modified in the case of several included toroidal modes.

Summary

Two possible mechanisms responsible for the saturation of the mode growth in ELM simulations have been analyzed. The first one is an additional stabilizing effect of the ideal wall when the displacement due to the instability becomes significant compared to the distance between plasma and wall. The second one is the reduction of background current density and pressure gradient at the edge by the perturbations, attenuating the drive of the instability. Both effects were shown to have an impact on the saturation in the simulations.
The influence of the reduction of the $(m,n) = (0,0)$ current density and pressure gradient at the edge onto the mode growth has been analyzed comparing the saturation of modes with different toroidal mode numbers. For large toroidal mode numbers, the saturation sets in at smaller energies contained in the mode than for small mode numbers. This is, because at the same mode energy, the perturbation is more localized, such that the background profiles are changed more significantly for large than for a small mode numbers.

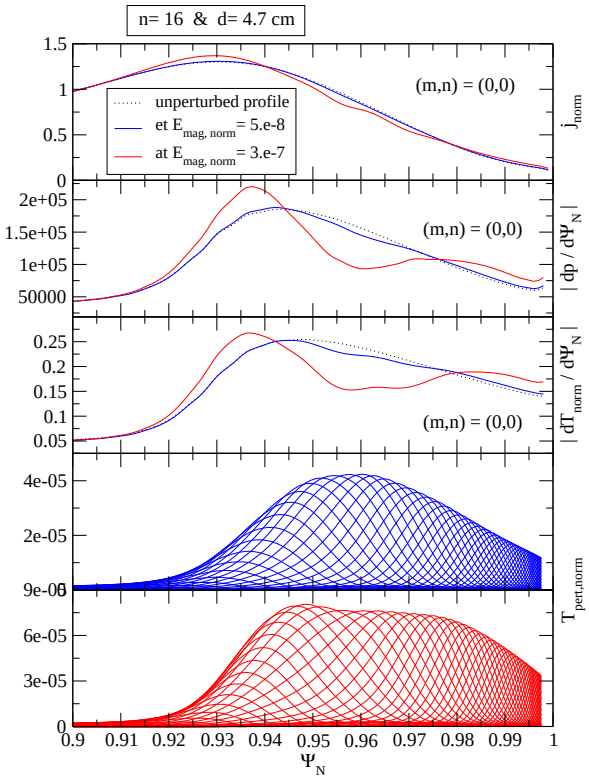

Figure 10.6.: Comparison of temperature perturbation and the $(m,n) = (0,0)$ current density, pressure gradient and temperature gradient edge profiles at two different moments. In this simulation only the $n = 16$ mode is included. The blue curves correspond to a moment at the beginning of the phase of saturation, the red ones to a moment, where the saturation has further progressed. In the region, where the $(m,n) = (0,0)$ current density and pressure gradient are reduced ($\Psi_N \approx 0.95 \ldots 0.97$), the perturbation grows more slowly, whereas it is enhanced in the region, where the background profiles are raised.

Furthermore, it has been discussed how the structure of the perturbations is influenced by changes in the background profiles. A local reduction of the background profiles, that are responsible for the mode drive, locally reduces the mode growth, while a local enhancement of the profiles acts destabilizing in that region.
Considering simulations with several included toroidal harmonics, additional effects let the saturation set in earlier (in terms of the energy of the most dominant mode) than in simulations

with only this toroidal mode. One reason for this is, that all included toroidal modes contribute to the perturbation of the $(m,n) = (0,0)$ current density and pressure gradient edge profiles, thus their influences accumulate.

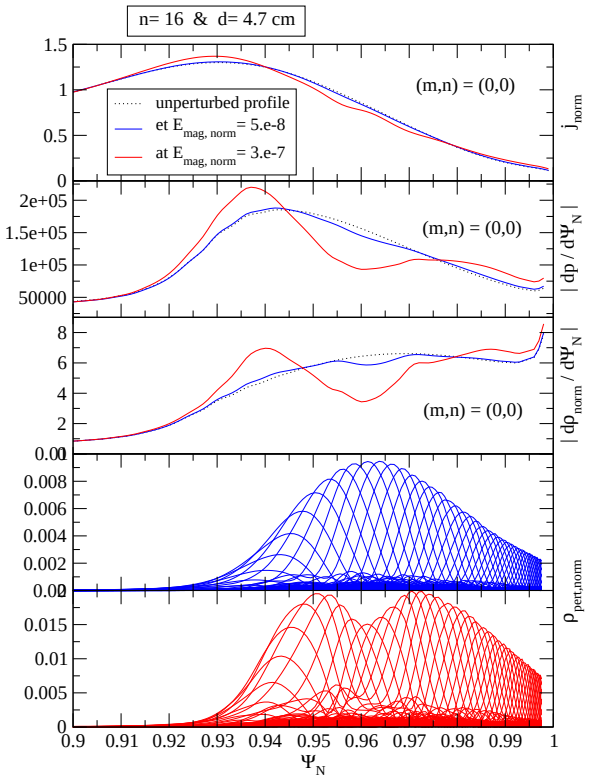

Figure 10.7.: Comparison of density perturbation and the $(m,n) = (0,0)$ current density, pressure gradient and density gradient edge profiles at two different moments. In this simulation only the $n = 16$ mode is included. The blue curves correspond to a moment at the beginning of the phase of saturation, the red ones to a moment, where the saturation has further progressed. As in Figure 10.6, the influence of changes in the background profiles onto the evolution of the mode structure is visible. To explain the differences between the structure of the density perturbation and the structure of the temperature perturbation shown in Figure 10.6 in the late phase of saturation, the background density gradient and temperature gradient profiles have to be considered.

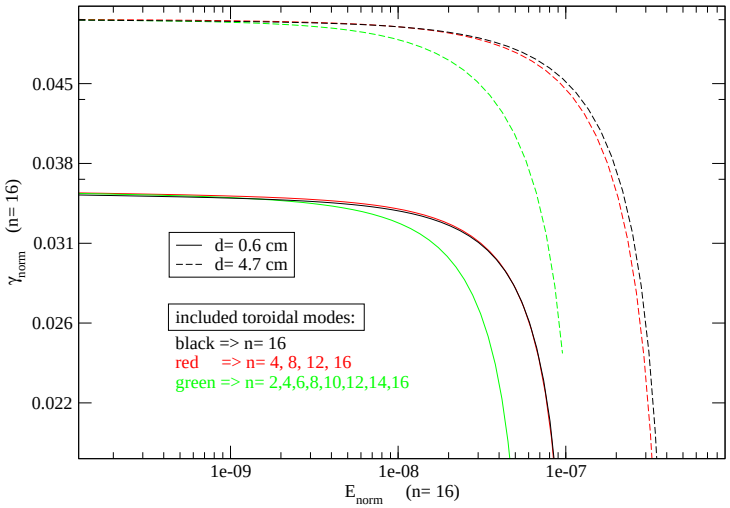

Figure 10.8.: Growth rate of the $n = 16$ mode in terms of its energy in simulations with different wall distances and different numbers of included toroidal modes. The saturation in simulation with small wall distances sets in already at lower energies than in simulations with large wall distances. This illustrates the additional stabilizing effect of the ideal wall in the phase of saturation. Furthermore, it can be seen, that in simulations with a high number of included modes, the saturation also sets in at lower energies.

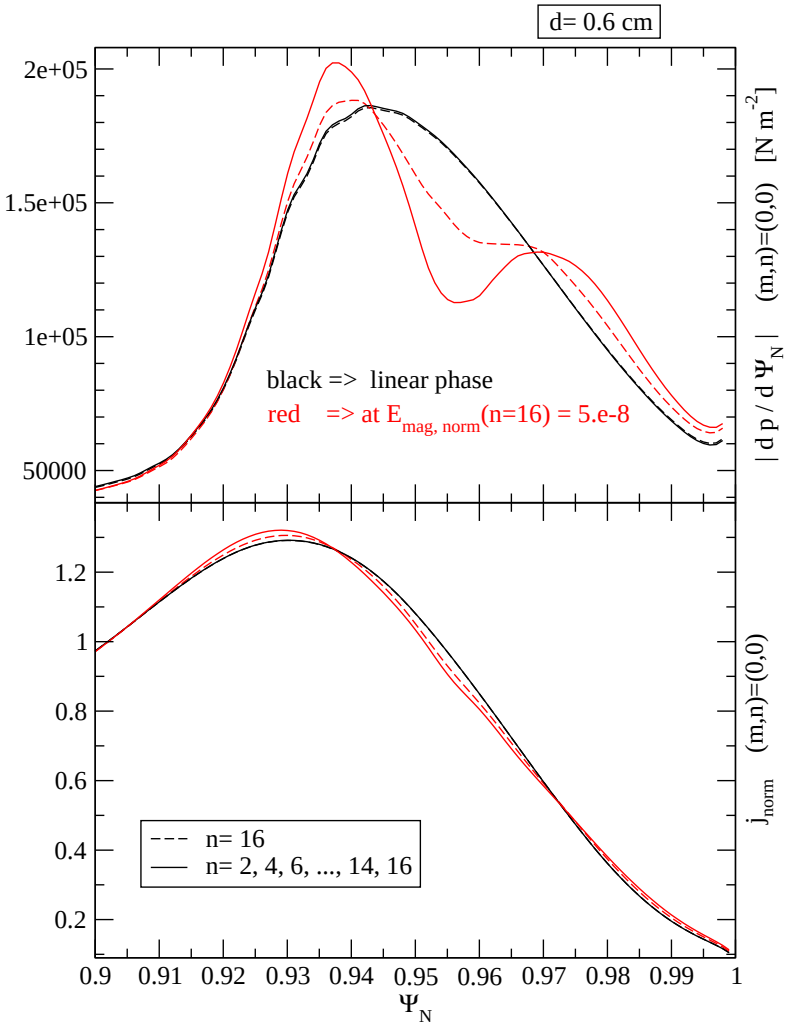

Figure 10.9.: Edge profiles of the $(m,n) = (0,0)$ pressure gradient and $(m,n) = (0,0)$ current density in the linear phase (black) and at a moment in the phase of saturation (red). A simulation with only one included toroidal mode and a simulation with eight included toroidal modes, where the $n = 16$ is the most dominant mode, are compared. The moment in the phase of saturation has been chosen such that the energy contained in the $n = 16$ mode is the same in both simulations. The background profiles are modified more significantly in the case of eight included modes. This corresponds to the expectations, as in this case all included modes contribute to the perturbation of background profiles.

Chapter 11.

Conclusion

In the thesis at hand, non-linear reduced MHD simulations of edge-localized modes in realistic ASDEX Upgrade geometry are presented and analyzed. The simulations have been carried out using the finite-element code JOREK. Analyzing the results of the simulations, emphasis is put onto the evolution of the structure of toroidal and poloidal Fourier modes of the perturbation. The linear mode growth, the non-linear evolution and the saturation of the mode growth have been examined in simulations with different numbers of included toroidal modes.

Chapter 8 treats the linear mode growth. Linear growth rates of different toroidal harmonics are studied in simulations including one single toroidal mode only. It is found that, in general, the modes with the highest toroidal mode numbers are the most unstable. This corresponds to the expectations, taking into account the neglect of diamagnetic stabilization in JOREK, which would act stabilizing for high mode numbers. At high mode numbers, the numerical results suggest, that the linear growth rate is proportional to the square root of the mode number.

Furthermore, the influence of an ideally conducting wall onto the linear mode growth has been analyzed. As expected, an ideal wall acts stabilizing. Growth rates drop with decreasing distance between plasma and wall. This influence of the ideal wall diminishes if the ratio Δ between the wall distance and the poloidal mode width is increased. This diminishment of the influence becomes significant at $\Delta \gtrsim 1/6$. At values of Δ of about 0.4, the logarithmic derivative of the linear growth rate with respect to Δ has dropped by about 75 %.

The dependence of the linear growth rates onto the wall distance can be reproduced for high mode numbers by means of a simple theoretical model, based on the idea, that a decrease of the wall distance yields an increase of vacuum magnetic field energy in the region between plasma and ideal wall. Thus, a smaller part of the energy released by the instability is transformed into kinetic energy deforming the plasma and the growth rate of the instability is reduced. This model assumes mode rigidity, in the sense that the structure of the mode is independent of the wall distance.

In Chapter 9, the non-linear evolution of the mode structure is studied on the basis of simulations with several included toroidal harmonics. A simple model of the non-linear interaction between the different included modes is developed. In this model, the time evolution of the mode amplitudes is determined by the energy transfer from the $n = 0$ mode, i.e., the linear growth, and by the exchange of energy with different non-zero toroidal modes, modeled as second order non-linear terms. The coupling constants, determining the strength of the mode coupling, are kept constant in time, assuming mode rigidity in the sense that the structure of the toroidal modes does not change significantly in time.

It is shown, that the main characteristics of the evolution of the toroidal mode structure in the

simulations can be explained and interpreted by means of this simple model. The time evolution of the energies contained in the toroidal modes and the evolution of their growth rates in two simulations with two different wall distances can be reproduced to a large extent by the mode interaction model, using the same set of coupling constants for both simulations. The universality of the coupling constants supports the assumption, that the shape of the perturbation is largely independent of the wall distance. In the phase of saturation, mode rigidity cannot be assumed anymore and other effects not included in the mode interaction model become important factors determining the evolution of the mode structure. As expected, the results of the simplified model begin to deviate from the results of the JOREK simulations during this phase.
The phase of saturation in the simulations is examined in Chapter 10. Mechanisms responsible for the saturation of the mode growth are studied. One of them is the additional stabilizing effect of the ideally conducting wall if the displacement becomes significant compared to the wall distance. The other one is a reduction of the background current density and pressure gradient in the radial region of the maximal perturbation, reducing the drive of the instability.
The latter effect becomes noticeable comparing the saturation of modes of different toroidal mode numbers. As perturbations of higher mode numbers are more localized, they are able to perturb the background edge profiles more strongly than modes of lower mode numbers when the same amount of energy is contained in the modes. This explains, why modes with high toroidal mode numbers saturate already at lower energies. Furthermore, it has been shown, how on the other hand the spatial structure of the toroidal modes is locally influenced by changes in the background profiles.
In simulations with more than one included toroidal harmonic, it is observed, that the saturation of the most dominant mode takes place at smaller energies contained in this mode than in simulations where only this mode is included. One reason for this is, that all of the included toroidal modes change the background current density and pressure gradient profiles, reducing the drive of the instability more efficiently than a single mode.

The results presented in Chapter 9 can be used to interpret recent experimental findings on type-I ELMs in ASDEX Upgrade. The multi-mode simulations which have been analyzed by means of the mode interaction model in this chapter were restricted to a periodicity 4, and hence did not include modes with toroidal mode numbers $n = 1, 2$. The realistic case with periodicity 1 is, for instance, treated in Reference [Hoelzl2012]. The mode coupling effects leading to the driven growth of the $n = 4$ mode in the simulations discussed in Chapter 9 would result in a growth of the $n = 1$ mode in the case with periodicity 1, particularly because this growth would be driven by the nonlinear interaction of several pairs of modes with mode numbers n and $n+1$ having simultaneously high linear growth rates. In fact, Figure 5 in Reference [Hoelzl2012], describing the energy development of the different toroidal modes shows a very strong analogy to Figure 9.4 in this work, with corresponding roles taken by the $n = 1$ and $n = 4$ modes in the two cases. It has thus been suggested [Hölzl, Krebs, Lackner; private communication], that the mechanism described in Chapter 9 could also be responsible for the pronounced $n = 1$ structure of the observed type-I ELMs in ASDEX Upgrade [Wenninger2012a] and other tokamaks [Wenninger2012].

Bibliography

[Atkinson1929] R. d. E. Atkinson, F. G. Houtermans, *Zur Frage der Aufbaumöglichkeit der Elemente in Sternen*, Zeitschrift für Physik A Hadrons and Nuclei, 54 (1929), 656, doi:10.1007/BF01341595, 10.1007/BF01341595.

[Bernard1981] L. Bernard, F. Helton, R. Moore, *GATO: An MHD stability code for axisymmetric plasmas with internal separatrices*, Computer Physics Communications, 24 (1981), #34, 377 , doi:10.1016/0010-4655(81)90160-0.

[Biskamp1993] D. Biskamp, *Nonlinear Magnetohydrodynamics*, Cambridge University Press (1993).

[Czarny2008] O. Czarny, G. Huysmans, *Bézier surfaces and finite elements for MHD simulations*, Journal of Computational Physics, 227 (2008), #16, 7423 , doi:10.1016/j.jcp.2008.04.001.

[Dudson2011] B. D. Dudson, X. Q. Xu, M. V. Umansky, H. R. Wilson, P. B. Snyder, *Simulation of edge localized modes using BOUT++*, Plasma Physics and Controlled Fusion, 53 (2011), #5, 054005, URL `http://stacks.iop.org/0741-3335/53/i=5/a=054005`.

[Dux2002] R. Dux, H. Zohm, R. Neu, *Plasmaphysik und Fusionsforschung Teil 2* (2002), doi:http://www.physik.uni-muenchen.de/lehre/vorlesungen/sose_12/A_PlasmaphysikII/vorlesung/skript.pdf, script.

[Eddington1920] A. S. Eddington, *The internal constitution of the stars*, The Observatory, 43 (1920), 341, doi:http://adsabs.harvard.edu/full/1920Obs....43..341E.

[Fitzpatrick2011] R. Fitzpatrick, *Plasma physics* (2011), URL `http://farside.ph.utexas.edu/teaching/plasma/380.pdf`, script.

[Fitzpatrick1996] R. Fitzpatrick, A. Y. Aydemir, *Stabilization of the resistive shell mode in tokamaks*, Nuclear Fusion, 36 (1996), #1, 11, URL `http://stacks.iop.org/0029-5515/36/i=1/a=I02`.

[Freidberg1987] J. P. Freidberg, *Ideal Magnetohydrodynamics*, Plenum Press, New York (1987).

[Gamow1928] G. Gamow, *Zur Quantentheorie des Atomkernes*, Zeitschrift für Physik A Hadrons and Nuclei, 51 (1928), 204, URL `http://dx.doi.org/10.1007/BF01343196`, 10.1007/BF01343196.

[Glasser1999] A. H. Glasser, C. R. Sovinec, R. A. Nebel, T. A. Gianakon, S. J. Plimpton, M. S. Chu, D. D. Schnack, the NIMROD Team, *The NIMROD code: a new approach to numerical plasma physics*, Plasma Physics and Controlled Fusion, 41 (1999), #3A, A747, URL `http://stacks.iop.org/0741-3335/41/i=3A/a=067`.

[Goedbloed2004] H. Goedbloed, S. Poedts, *Principles of Magnetohydrodynamics*, Cambridge University Press (2004).

[Henon2002] P. Hénon, P. Ramet, J. Roman, *PaStiX: a high-performance parallel direct solver for sparse symmetric positive definite systems*, Parallel Computing, 28 (2002), #2, 301 , doi:10.1016/S0167-8191(01)00141-7.

[Hirsch1988] C. Hirsch, *Numerical computation of internal and external flows*, volume 1, John Wiley & Sons (1988).

[Hoelzl2009] M. Hölzl, S. Günter, I. Classen, Q. Yu, the TEXTOR Team, E. Delabie, *Determination of the heat diffusion anisotropy by comparing measured and simulated electron temperature profiles across magnetic islands*, Nuclear Fusion, 49 (2009), #11, 115009, URL `http://stacks.iop.org/0029-5515/49/i=11/a=115009`.

[Hoelzl2012] M. Hölzl, S. Günter, R. P. Wenninger, W.-C. Müller, G. T. A. Huysmans, K. Lackner, I. Krebs, the ASDEX Upgrade Team, *Reduced-magnetohydrodynamic simulations of toroidally and poloidally localized edge localized modes*, Physics of Plasmas, 19 (2012), #8, 082505, doi:10.1063/1.4742994.

[Hoelzl2011] M. Hölzl, et al., *Reduced-MHD simulations of edge-localized modes in ASDEX Upgrade*, in *38th EPS Conference on Plasma Phys., Strasbourg* (2011) URL `http://ocs.ciemat.es/EPS2011PAP/pdf/P2.078.pdf`.

[Huysmans2008] G. Huysmans, *Non-linear MHD simulations of ELMs*, in *35th EPS Conference on Plasma Phys., Hersonissos* (2008) URL `http://epsppd.epfl.ch/Hersonissos/pdf/P2_065.pdf`.

[Huysmans2007] G. Huysmans, O. Czarny, *MHD stability in X-point geometry: simulation of ELMs*, Nuclear Fusion, 47 (2007), #7, 659, URL `http://stacks.iop.org/0029-5515/47/i=7/a=016`.

[Huysmans2009] G. T. A. Huysmans, S. Pamela, E. van der Plas, P. Ramet, *Non-linear MHD simulations of edge localized modes (ELMs)*, Plasma Physics and Controlled Fusion, 51 (2009), #12, 124012, URL `http://stacks.iop.org/0741-3335/51/i=12/a=124012`.

[Huysmans2001] G. T. A. Huysmans, S. E. Sharapov, A. B. Mikhailovskii, W. Kerner, *Modeling of diamagnetic stabilization of ideal magnetohydrodynamic instabilities*

associated with the transport barrier, Physics of Plasmas, 8 (2001), #10, 4292, doi:10.1063/1.1398573.

[Kadomtsev1974] B. Kadomtsev, O. Pogutse, *Nonlinear helical perturbations of a plasma in the tokamak*, Sov. Phys.-JETP, 38 (1974), 283.

[Kass1998] T. Kass, S. Günter, M. Maraschek, W. Suttrop, H. Zohm, ASDEX Upgrade Team, *Characteristics of type I and type III ELM precursors in ASDEX upgrade*, Nuclear Fusion, 38 (1998), #1, 111, URL `http://stacks.iop.org/0029-5515/38/i=1/a=310`.

[Keilhacker1984] M. Keilhacker, et al., *Confinement studies in L and H-type Asdex discharges*, Plasma Physics and Controlled Fusion, 26 (1984), #1A, 49, URL `http://stacks.iop.org/0741-3335/26/i=1A/a=305`.

[Klimov2011] N. Klimov, et al., *Experimental study of PFCs erosion and eroded material deposition under ITER-like transient loads at the plasma gun facility QSPA-T*, Journal of Nuclear Materials, 415 (2011), #1, Supplement, 59 , doi:10.1016/j.jnucmat.2011.01.013, proceedings of the 19th International Conference on Plasma-Surface Interactions in Controlled Fusion.

[Konz2007] C. Konz, L. Horton, E. Strumberger, S. Günter, P. M. Carthy, G. Huysmans, P. Snyder, ASDEX Team, *The peeling-ballooning model revisited*, in *34th EPS Conference on Plasma Phys., Warsaw* (2007) .

[Loarte2003] A. Loarte, et al., *Characteristics of type I ELM energy and particle losses in existing devices and their extrapolation to ITER*, Plasma Physics and Controlled Fusion, 45 (2003), #9, 1549, URL `http://stacks.iop.org/0741-3335/45/i=9/a=302`.

[McCarthy1999] P. J. McCarthy, P. Martin, W. Schneider, *The CLISTE interpretive equilibrium code*, Technical Report IPP-Report 5/85, Max-Plack-Institut für Plasmaphysik (1999).

[Osmanlic2012] F. Osmanlic, S. Günter, C. Konz, M. Dunne, *Ideal linear MHD stability analysis of the edge plasma in ASDEX Upgrade*, to be published.

[Pamela2010] S. Pamela, *Simulation Magnéto-Hydro-Dynamiques des Edge-Localised-Modes dans un tokamak*, Ph.D. thesis, Université de Provence (2010).

[Pamela2010a] S. Pamela, G. Huysmans, S. Benkadda, *Influence of poloidal equilibrium rotation in MHD simulations of edge-localized modes*, Plasma Physics and Controlled Fusion, 52 (2010), #7, 075006, URL `http://stacks.iop.org/0741-3335/52/i=7/a=075006`.

[Pamela2011] S. J. P. Pamela, G. T. A. Huysmans, M. N. A. Beurskens, S. Devaux, T. Eich, S. Benkadda, J. E. contributors, *Nonlinear MHD simulations of*

edge-localized-modes in JET, Plasma Physics and Controlled Fusion, 53 (2011), #5, 054014, URL http://stacks.iop.org/0741-3335/53/i=5/a=054014.

[Pankin2007] A. Y. Pankin, G. Bateman, D. P. Brennan, A. H. Kritz, S. Kruger, P. B. Snyder, C. Sovinec, the NIMROD team, *Modelling of ELM dynamics for DIII-D and ITER*, Plasma Physics and Controlled Fusion, 49 (2007), #7, S63, URL http://stacks.iop.org/0741-3335/49/i=7/a=S04.

[Park1999] W. Park, E. V. Belova, G. Y. Fu, X. Z. Tang, H. R. Strauss, L. E. Sugiyama, *Plasma simulation studies using multilevel physics models*, Physics of Plasmas, 6 (1999), #5, 1796, doi:10.1063/1.873437.

[Saarelma2003] S. Saarelma, S. Gnter, L. Horton, A. U. Team, *MHD stability analysis of type II ELMs in ASDEX Upgrade*, Nuclear Fusion, 43 (2003), #4, 262, URL http://stacks.iop.org/0029-5515/43/i=4/a=307.

[Schneider2012] P. A. Schneider, *Characterization and scaling of the tokamak edge transport barrier*, Ph.D. thesis, Ludwig-Maximilians-Universität München (2012), URL http://edoc.ub.uni-muenchen.de/14723/1/Schneider_Philip.pdf.

[Snyder2004] P. Snyder, et al., *ELMs and constraints on the H-mode pedestal: peeling-ballooning stability calculation and comparison with experiment*, Nuclear Fusion, 44 (2004), #2, 320, URL http://stacks.iop.org/0029-5515/44/i=2/a=014.

[Spitzer1953] L. Spitzer, R. Härm, *Transport phenomena in a completely ionized gas*, Phys. Rev., 89 (1953), 977, doi:10.1103/PhysRev.89.977.

[Stangeby1995] P. C. Stangeby, A. V. Chankin, *The ion velocity (Bohm–Chodura) boundary condition at the entrance to the magnetic presheath in the presence of diamagnetic and E x B drifts in the scrape-off layer*, Physics of Plasmas, 2 (1995), #3, 707, doi:10.1063/1.871421.

[Strauss1976] H. R. Strauss, *Nonlinear, three-dimensional magnetohydrodynamics of noncircular tokamaks*, Physics of Fluids, 19 (1976), #1, 134, doi:10.1063/1.861310.

[Sugiyama2010] L. E. Sugiyama, H. R. Strauss, *Magnetic X-points, edge localized modes, and stochasticity*, Physics of Plasmas, 17 (2010), #6, 062505, doi:10.1063/1.3449301.

[Suttrop2000] W. Suttrop, *The physics of large and small edge localized modes*, Plasma Physics and Controlled Fusion, 42 (2000), #5A, A1, URL http://stacks.iop.org/0741-3335/42/i=5A/a=301.

[Teller1981] E. Teller, et al., *Fusion*, volume 1, Academic Press (1981).

[Wagner2012] F. Wagner, *Feature of an electricity supply system based on variable input*, Technical Report IPP 18/1, Max-Planck-Institut für Plasmaphysik (2012), URL http://edoc.mpg.de/display.epl?mode=doc&id=618631&col=33&grp=1311.

[Wenninger2012] R. Wenninger, H. Reimerdes, O. Sauter, H. Zohm, *3D structure of the non-linear ELM phase*, in *39th EPS Conference on Plasma Phys., Stockholm* (2012) .

[Wenninger2012a] R. Wenninger, et al., *Solitary magnetic perturbations at the ELM onset*, accepted for publishing in Nuclear Fusion, preprint at arXiv:1202.3603.

[Wesson2004] J. Wesson, *Tokamaks*, 3 edition, Oxford University Press (2004).

[Wilson2002] H. R. Wilson, P. B. Snyder, G. T. A. Huysmans, R. L. Miller, *Numerical studies of edge localized instabilities in tokamaks*, Physics of Plasmas, 9 (2002), #4, 1277, doi:10.1063/1.1459058.

[Zohm1996] H. Zohm, *Edge localized modes (ELMs)*, Plasma Physics and Controlled Fusion, 38 (1996), #2, 105, URL http://stacks.iop.org/0741-3335/38/i=2/a=001.

[Zohm2004] H. Zohm, *MHD-Gleichgewichte und Stabilität heißer Fusionsplasmen* (2004), URL www.aug.ipp.mpg.de/E2/Mitarbeiter/Zohm/scripts/Zohm/mhd.pdf, script.

[Zohm2010] H. Zohm, *Plasmaphysik Teil 1* (2010), URL www.aug.ipp.mpg.de/E2/Mitarbeiter/Zohm/scripts/Plasmaphysik1.pdf, script.

Acknowledgments

I would like to thank Karl Lackner, Hartmut Zohm and Sibylle Günter for many inspiring ideas and fruitful discussions.

I am also deeply grateful to Matthias Hölzl for the great support, for all the time he spent answering innumerable questions, for help whenever I needed some, for teaching me so much and for his precious motivating positivity.

Finally, I would like to thank Johannes for his steadfast loving support.

Declaration:

I hereby declare that this thesis is my own work, and that I have not used any sources and aids other than those stated in the thesis.

München, September 28, 2012

_____

Isabel Krebs